INAUGURAL-DISSERTATION

zur Erlangung der Doktorwürde der
Naturwissenschaftlich-Mathematischen
Gesamtfakultät der Ruprecht-Karls-Universität
Heidelberg

vorgelegt von

Dipl.-Chem. Eva Bock
aus Edenkoben

Tag der mündlichen Prüfung: 17. Oktober 2008

Deposition and Growth of Various Nanomaterials at Nanostructured Interfaces

Gutachter:

Prof. Dr. Joachim P. Spatz
Biophysikalische Chemie
Universität Heidelberg

PD Dr. Reiner Dahint
Angewandte Physikalische Chemie
Universität Heidelberg

Contents

Summary

The goal of this work is the deposition and growth of various nanoobjects on patterned surfaces. For this purpose, patterned surfaces function as a chemical template to direct the location and shape of the added nanoobjects. In particular, colloidal nanoparticles, viral particles and inorganic salts are used to assemble small structures along large areas of chemical surface patterns.

The substrates for these assays are based on glass or silicon, which have been decorated with gold or platinum nanoparticles. These nanostructured substrates were obtained by block copolymer micelle nanolithography. The technology has been substantially improved for application to large-scale surface areas and optimum pattern quality. Here, the influence of trapped solvent vapor above the dipping solution on the thickness of the adsorbed polymer film was investigated. A higher amount of trapped vapor results in an increase of the lateral distance of the nanoparticles on the surface and a more reproducible pattern formation, which was shown by SEM analysis. Nanopatterned surfaces were then used as a chemical mosaic platform for the deposition and growth of different nanoobjects.

CdSe-Au dumbbells, $CoPt_3$-Au heterodimers and Co-Au matchsticks were attached to gold nanoparticles which were deposited by block copolymer micelle nanolithography via a dithiol linker. The resulting patterns show a random orientation of the nanocrystals. The magnetic Co-Au matchsticks were additionally aligned in a magnetic field, resulting in an ordered surface. Furthermore, CdSe-Au dumbbells were immobilized by DNA assembly. Here, hybridization allowed for a controlled and reversible attachment of the nanocrystals on the surface.

Direct assembly of spherical CdSe nanocrystals on a non-patterned surface was realized by block copolymer micelle nanolithography. Hydrophilic ligands enable the interaction between the nanocrystals as formed in organic solvents and the polar core of block copolymer micelles. Guided by the block copolymer micellar core the CdSe particles were hexagonally arranged on the substrate, with 3 or 4 particles being located in one micelle. The number of CdSe particles per micelle was investigated by electron and fluorescence microscopy and was found to be independent from the size of the polymer. In a solution-liquid-solid approach, CdSe rods and wires as well as Co rods were grown on the nanopatterned substrates. For the growth of the CdSe rods and wires, Au@Bi core shell particles on the surface were used as a catalyst. Interestingly, the Au@Bi core shell particles remained on the substrate while the tips of the wires were covered by the growth of bismuth.

Layers of biotin modified cowpea mosaic viruses are formed on a biotin-doped lipid bilayer on a hydrophilic silicon oxide surface, connected by streptavidin. In quartz crystal microbalance studies, different biotin modifications were compared. The resulting films showed differences in their roughness and density. Thiol-modified streptavidin enabled the attachment of the virus nanoparticles to gold, where the resulting layer has the same density as on the lipid

bilayer.

In summary, nanostructured substrates are a versatile platform for the assembly of organic and inorganic nanoparticles as well as growth seeds for inorganic material. Several different methods to control the assembly of particles on a solid substrate were successfully investigated, demonstrating their potential for further application in nanotechnology.

Zusammenfassung

Ziel dieser Arbeit ist die Anbindung verschiedenster Materialien an chemisch strukturierte Oberflächen gewesen. Dabei wurden kolloidale Nanokristalle und Viren zum Aufbau komplexer Strukturen auf nanostrukturierten Oberflächen genutzt.

Chemisch nanostrukturierte Oberflächen wurden mit Hilfe amphiphiler Blockcopolymere hergestellt. Diese Technologie wurde insbesondere für große Substratflächen und bezüglich der reproduzierbaren Qualität der entstehenden Oberflächenmuster optimiert. Hierbei zeigte sich, dass Lösungsmitteldämpfe, die sich über der Polymerlösung ansammeln, den Abstand zwischen den Nanopartikeln auf der Oberfläche und die Qualität der Oberflächenmuster wesentlich beeinflussen. Je mehr Dampf sich über der Polymerlösung ansammelt, desto weiter sind die Partikel auf der Oberfläche voneinander entfernt. Eine Erklärung hierfür ist eine Änderung der Oberflächenspannung der Polymerlösung durch den Dampf. Eine geringere Oberflächenspannung führt zu einem dünneren Polymerfilm, der sich auf der Oberfläche beim Eintauchen abscheidet. Dies wiederum führt zu größeren Abständen zwischen den Partikeln.

Auf diese chemisch strukturierten Oberflächen wurden in der Folge kolloidale Nanokristalle und virale Partikel angebunden. Nanohanteln aus CdSe mit Goldbereichen an den Enden, Heterodimere aus $CoPt_3$ und Gold sowie Nanostreichhölzer aus Kobalt mit einem Kopf aus Gold wurden mit einem Dithiollinker an die Goldpunkte auf der Oberfläche angebunden. In AFM-Messungen konnte gezeigt werden, dass die Goldbereiche der Nanokristalle auf den Goldpartikeln der Oberfläche liegen. Die magnetischen Kobaltnanopartikel konnten zusätzlich in einem magnetischen Feld auf der Oberfläche ausgerichtet werden. Die CdSe-Goldnanohanteln wurden außerdem über DNA mit der Oberfläche verbunden. Durch die Hybridisierung von DNA-modifizierten Partikeln mit einer DNA-funktionalisierten Oberfläche erhält man eine reguläre Anordnung der Nanokristalle auf der Oberfläche. Um runde CdSe-Nanopartikeln auch ohne ein verknüpfendes Molekül auf einer Oberfläche anzuordnen, wurden die Liganden auf der Oberfläche des Nanopartikels ausgetauscht. Man erhält so hydrophile Partikel, die mit dem polaren Kern einer Mizelle aus Blockcopolymeren reagieren können. Aufgrund der Selbstorganisation der Blockcopolymermizellen organisierten sich die Partikel folglich in einer hexagonalen Anordnung. Im Elektronenmikroskop wurde sichtbar, dass sich jeweils drei oder vier Partikel in einer Mizelle befinden. Diese Zahl zeigte sich unabhängig von der Masse des verwendeten Polymers, was auch in Fluoreszenzmessungen bestätigt werden konnte.

Stäbchen und Drähte aus CdSe und Kobaltstäbchen können auch direkt auf der Oberfläche hergestellt werden. Kern-Schale-Partikel mit einem Kern aus Gold und einer Hülle aus Wismuth können auf der Oberfläche hergestellt werden und dann als Ausgangspunkt für das Wachstum von CdSe-Stäbchen genutzt werden. Interessanterweise bilden die Wismuthhüllen die freien En-

den der Drähte, während die Goldpartikel nach wie vor auf der Oberfläche zu finden sind.

Mehrere Lagen aus viralen Nanopartikeln können kontrolliert auf einer Lipiddoppelschicht aufgebaut werden. Die Viren sind an ihrer Proteinhülle mit Biotin modifiziert und auch die Lipiddoppelschicht enhält Biotinmoleküle, so dass mit Hilfe von Streptavidin eine Anbindung erfolgen kann. In Quartzkristallmessungen kann die Rauigkeit der entstandenen Oberfläche in Zusammenhang gebracht werden mit der Anzahl an Biotinmolekülen auf der Oberfläche der Viren. Thiol-modifiziertes Streptavidin ermöglicht die Anbindung der Viren auch direkt auf einer Goldoberfläche, wobei sich die entstehende Schicht nicht von der auf der Lipiddoppelschicht unterscheidet.

Nanostrukturierte Oberflächen können so auf vielfältige Weise genutzt werden, um Nanopartikel daran anzubinden. Verschiedene Methoden sind möglich, um sowohl organische wie auch anorganische Partikel anzuordnen. Die erhaltenen Strukturen stellen interessante Grundlagen für mögliche Anwendungen in der Nanotechnologie

Part I
Introduction

1 Introduction

Nanotechnology is considered to be a key technology for the upcoming century [1]. Materials at the nanoscale have exceptional physical properties, which make them promising candidates as building blocks for new applications and technologies [2]. Already in 1959, Richard Feynman formulated the vision of performing engineering task at a very low scale in his lecture 'There is plenty of room at the bottom' [3]. Since then the field of nanotechnology has evolved to a nowadays interdisciplinary discipline, where chemistry with its preparational methods, physics with investigation methods, and biology with functional molecules work hand in hand. In the approach towards the nano-regime two major principles can be distinguished, which deal with preparation and manipulation of nano-materials, the so-called 'top-down' and 'bottom-up' approaches [4].

Standard lithographic methods, including photo, focused ion beam (FIB) or electron beam (e-beam) lithography, enable the top-down structuring of surfaces [5–7]. A photosensitive material is exposed to UV-light; an electron or ion beam is used to write nanopatterns in substrates. The limit in resolution of photolithography is the wavelength of the light. Structures below 200 nm are hardly accessible. In FIB and e-beam lithography it is possible to obtain structures in the range of 20 nm, but here sophisticated and expensive equipment is needed.

The concept of bottom-up relies on the self-assembly of small building blocks to larger structures. Block copolymer nanolithography and colloidal lithography are widely spread, as these methods offer a cheap and fast structuring of the surface [8–10]. Extended research on the self-assembly of DNA has been investigated, to form 2D as well as 3D structures [11,12]. For aperiodic structures dip-pen nanolithography (DPN) and microcontact printing (μCP) are widely spread, where the molecules are precisely positioned in the desired pattern on the surface [13, 14]. A combination of bottom-up with top-down lithographic methods might be the key for the development of new materials [15,16].

In the framework of this work two different techniques of nanotechnology were brought into contact for the benefit of the assembly of small structures into larger arrays. Colloidal nanoparticles, as presented in section 1.3 offer an easy access to a wide range of physical properties. These nanoparticles can spontaneously assemble into regular structures, but in most cases these are limited in size and the control of the interparticle spacing. Virus nanoparticles, described in section 1.5.2, present alternatives for building blocks in nanotechnology. Diblock copolymer based nanolithography enables the production of macroscopic surfaces with a nanoscopic structure with controlled interparticle spacing. Only it is limited in the choice of material. This technique will be briefly introduced in section 1.2.

1.1 Assembly of Inorganic Nanocrystals

Metal and semiconductor particles in the nanometer range are of various interests for technical and biological applications due to their unique, size dependent optical, electronical and catalytic characteristics [17–19]. Recent advances led to the development of shape-controlled nanoparticles, including a rod or tetrapod like shape (figure 1) [20–26]. A short introduction on the synthesis techniques and general properties of semiconductor and magnetic nanoparticles will be given in sections 1.3.1, 1.3.2, and 1.4.

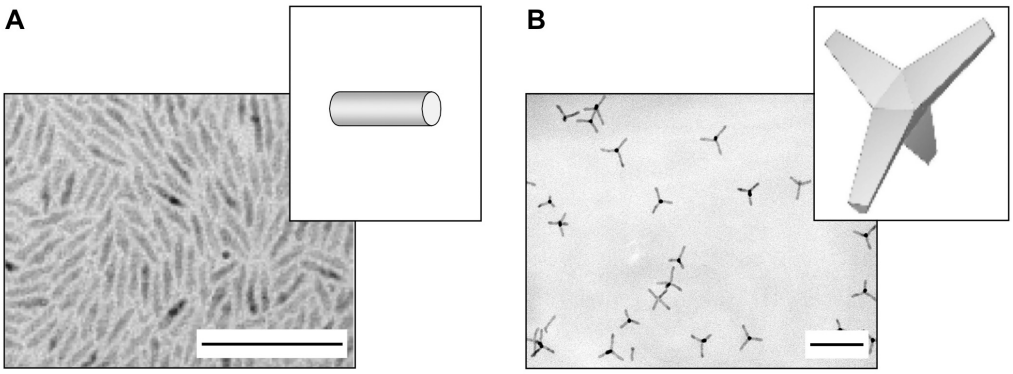

Figure 1: **Shape control of inorganic nanocrystals**. A: TEM image and schematic of CdTe rods. B: TEM image and schematic of CdTe tetrapods. The scale bars correspond to 100 nm (images adapted from [27]).

The assembly of such nanoscale building blocks into complex architectures is a primary challenge in material science [28]. Many applications, including photonic band gap devices, nanostructured solar cells, magnetic data storage media, and biomedical devices require the fabrication of highly ordered structural features [29–32]. Magnetic phenomena of nanoscaled materials and catalytic reactions are just two areas where the desired properties may not only depend on the size of the individual nanostructures but also on their spacing. Dipolar magnetic interactions between neighboring particles or spill-over and transport processes on the surface are dependent on the distance between particles [33, 34].

One can distinguish between different approaches towards the assembly of colloidal particles. First, the particles are assembled through linker molecules. This type of assembly might be done in solution. The growth of a gold domain to semiconducting nanocrystals, as described in section 1.3.4, enables a specific binding site for thiolated molecules. Second, the particles are assembled through particle-particle interactions, mainly van-der-Waals forces. In general this is a phenomenon which occurs when the nanoparticles are spread onto a surface and the solvent is allowed to evaporate.

The assembly of particles in solution has been realized by different approaches. The formation of chains of single nanoparticles has been realized by selective

functionalization at the opposite sides of spherical particles [35]. Gold particles with single stranded DNA strands are organized into larger structures by hybridization with complementary DNA strands. Two gold dots have been connected with each other in such a way over distances up to 12,5 nm [36]. Also larger assemblies have been realized with DNA, but so far only in solution [37]. Incapsulating colloidal nanocrystal in poylmers results in the assembly of the particles inside these polymers [38–40]. Functional polymers have been used to form chains of the coated particles [41]. But still, also under the vision of applications such as data storage, a much more controlled assembly of the particles on a substrate is desired, where certain requirements have to be taken into account.

Improved data storage systems require reduced chipsize. The storage of a large amount of data on such a small surface can only be achieved if each individual particle is addressable without any interaction with neighboring crystals. One possibility would be the use of an AFM cantilever for the write and read process (figure 2).

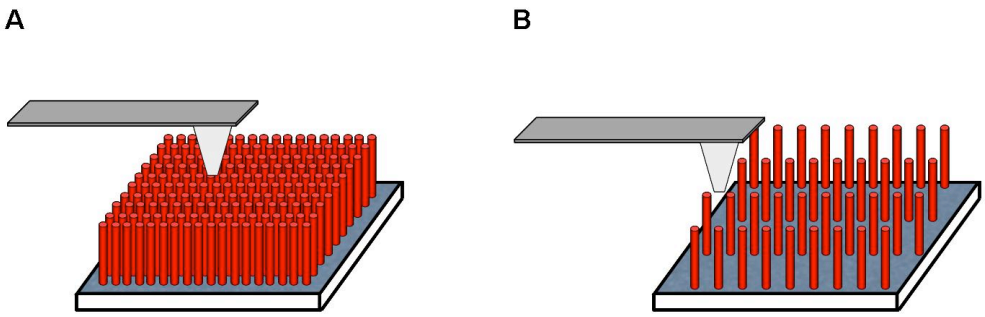

Figure 2: **Schematic of possible data storage via AFM**. A: particles assembled next to each other are not individually addressable. B: An interparticle distance in the range of the diameter of the AFM tip enables to distinguish neighboring particles.

Each nanoparticle acts as a variable magnet that stores data. A current passing from the AFM tip through the anisotropic nanocrystal induces a magnetization of of the particle. Nowadays high precision cantilevers have a tip radius of 15 nm [42]. To distinguish single nanoparticles from each other the nanocrystals have to be positioned precisely, with a distance of about 15 - 20 nm in a highly ordered fashion to enable automatic read out of the stored information.

Films of different inorganic nanocrystals are frequently obtained by evaporating the solvent [43–45]. These superlattices are forming due to interactions of the ligands around the particles with each other [43]. The resulting morphologies can be either colloidal crystals or ordered thin films, which can be controlled by the solvent, reaction temperature and pressure [46]. The nanoparticles arrange in a regular lattice with a typical dimension of several micrometers [43, 46]. The interparticle distance is less than 1 nm, corresponding to the length of the ligands. By adding crosslinkers it is even reduced to 0,8

nm [47].

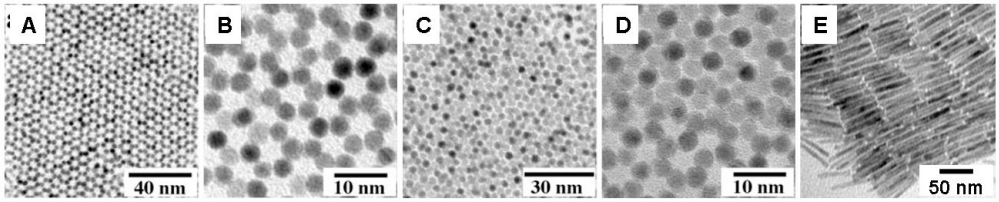

Figure 3: **TEM images of regular arranged nanocrystals.** A-D: Regular arrangements of $CoPt_3$ nanocrystals out of two (A, B) and three (C, D) layers (from [45]). E: Evaporation-mediated self-assembly of CdSe/CdS nanorods prepared by seeded growth (from [44]).

Nanocrystalline particulate films can be grown in-situ under floating monolayers on top of an unpolar solvent. So far films of CdS, ZnS, PbS, CdSe, PbSe, Ag and Au have been grown usig this approach [48, 48–52]. In a first step, a porous film composed of elliptically shaped particles with a thickness of 2 - 4 nm and maximum length of 3 - 8 nm is forming. Diffusion of fresh metal ions to this first layer results in the formation of further layers. In the end, the film can reach a thickness up to 350 nm for CdS particles, above which no further growth is observed [53]. Afterwards they are transferred to solid substrates by standard coating techniques. Crystal structure, morphology, orientation and film thickness can be controlled by the choice of the monolayer and the experimental conditions [54].

A further method to transfer surfactant coated NCs on surfaces uses the Langmuir Blodgett (LB) technique. It is used for the formation of films at the air-water interface [55]. A Langmuir-Blodgett film consists of a monolayer of organic molecules assembled on this interface. It can be transferred from the surface of a liquid onto a solid by immersing a substrate into the liqid. A monolayer is added with each immersion or emersion step, thus films with very accurate thickness can be formed [56]. Surfactant stabilized nanoparticles can be dispersed on an aqueous surface. Spreading the particles in a Langmuir trough facilitates their transfer to a wide range of solid substrates. Moving a clean plate through the monolayer on the solution forms LB films [55].

Even though it is possible to create different kinds of films with these techniques, there are limitations to be considered. The interparticle distance is controlled only by the surfactant's chemistry, mainly the length of the alkyl chain [47]. In the case of TOPO, which is a standard surfactant, it is 1,3 nm, which corresponds to eight CH_2 groups. Elongation of the chain to 18 CH_2 groups leads to an increase of the particles distance of 1,4 nm, considering a stretched form (C-C bond corresponds to 154 pm). The longer the surrounding molecule is, the more complex is the determination of the size of the shell, formed by the layer. Therefore it is hard to specify the effective size of differently coated particles, as different methods result in large derivations [57].

All techniques introduced so far allow access to homogenous films of closed-

packed nanocrystals. For a more flexible and controlled assembly of inorganic nanocrystals, the particles have been modified with functional molecules. A gradient of spherical streptavidin modified CdSe particles have been successfully introduced on a polyethylene (PE) surface [58]. As the avidin-biotin system is a widely exploited tool for biological application, due to its high binding affinity ($K_D > 10^{-15}M$) [59, 60], the PE substrate is functionalized with a gradient of biotin molecules. Incubation of the streptavidin coated CdSe particles results then in a gradient of the particle density on the PE surface [58]. Even though a gradient can be observed in fluorescence intensity, the lateral distance between each CdSe particle cannot precisely be controlled.

So far, assemblies of inorganic nanocrystals have been realized mainly by slow evaporation of the solvent. The distance between the single particles is in the range of few nanometers, as controlled by the length of the surfactant. The assemblies usually cover a surface area in the range of few micrometers. In this work, a new approach was investigated in order to align inorganic nanocrystals on larger areas and with larger distances between the inorganic nanocrystals. To this aim, nanostructured substrates have been employed. Hexagonally arranged gold nanoparticles were obtained by block copolymer nanolithography, where the lateral distance between the gold particles on the surface can be controlled. With this method it is possible to structure substrates with a size of several cm^2. Different linkers were introduced, to immobilize colloidal nanocrystals specifically over their gold domains on the gold particles of the surface. Also approaches without linkers where employed. The controlled assembly allows for a control over the lateral distance of the inorganic nanocrystals. The different methods lead to homogeneously functionalized substrates that extend several cm^2, which is not possible by the methods described so far. In the following section 1.2 the structuring of surfaces with block copolymers is introduced. A short presentation of the properties of the employed colloidal nanocrystals is provided in section 1.3 and 1.4.

1.2 Nanostructured Substrates

Nanopatterned substrates, where the interparticle distance can be adjusted in a wide range, are a versatile platform for the immobilization of nanoparticles [61]. It allows a control of the lateral distance between the attached nanocrystals [34]. Nanopatterned substrates, prepared with block copolymer nanolithography, enable the control in the interparticle distance up to 250 nm, which is a range, not accessible by the above-described methods [62, 63]. Surfaces, decorated with gold nanoparticles with a diameter of 3 to 30 nm and a lateral distance, ranging from 20 to 250 nm have successfully been prepared by block copolymer micellar nanolithograhy [64]. These gold particles can be used as anchoring points for linkers between the surface particles and the ones in solution.

1.2.1 Block Copolymer Micellar Nanolithography

Block copolymer micellar nanolithography is a tool for the fabrication of nanostructured surfaces [65,66]. The accessible length scale is below 100 nm, which is barely achievable by other lithographic methods [4].

A diblock copolymer consists of two chemically different chains, which spontaneously assemble in solution [67]. A system will then self-assemble if its building blocks have appropriate interaction capabilities to form stable, well defined structures that can range from a few nanometers to millimeters in size [9, 68, 69]. Tailoring the properties of the building blocks controls this process. The final structure is reached by equilibrating the lowest free-energy state, in which both attraction and repulsion between the building blocks are well balanced [70].

Diblock copolymers, consisting of at least two chemically distinct, immiscible polymer fragments which are joined by a covalent bond, are well studied systems [68]. They can self-assemble into different structures [9]. The morphology depends on the overall molecular weight $N = N_A + N_B$, the composition $f = V_A/(V_A + V_B)$ and the energy of mixing both segments, the so-called Flory-Huggins parameter χ. It describes the strength of the repulsion forces between the polymer blocks [9,10,71,72]. With rising temperature χ decreases according to

$$\chi_{AB} = \frac{1}{k_B T} \cdot \left[E_{AB} - \frac{1}{2} \cdot (E_{AA} - E_{BB}) \right] \tag{1}$$

with E_{ij} being the interaction energy between the two blocks i and j. A separation into microdomains is favoured by high values of χ_{AB}, but on the other hand restricted by the associated loss in the conformation entropy ($S \propto N^{-1}$). Therefore, the segregation energy is controlled by the product of the segment-segment interaction parameter χ and the overall degree of polymerization. In the weak segregation limit ($\chi \cdot N << 1$), the block copolymer melt is disordered, whereas in the strong segregation limit ($\chi \cdot N >> 10$) a microphase separation into A and B domains is observed [73]. While block copolymers in solution generally tend to form spherical micelles, if one block is preferentially dissolved by the solvent, the bulk structure can vary [69]. The most common features are spherical, cylindrical or lamellar morphologies (figure 4A, B, E), but also gyroid (figure 4C) or double diamond structures (figure 4D) can occur [66,74,75].

The resulting structure is dependent on the volume fraction of the blocks. Spherical structures (figure 4A) usually occur, if the volume fraction of the A block is between 0 and 21 %. With rising percentage (21 - 33 %) the cylinders (figure 4B) become the preferential phase. In the range of 33 - 37 % of the A block, gyroid (figure 4C) and double diamond (figure 4D) are the preferred structure, while with rising fraction of A (37 - 50 %) the lamellar order (figure 4E) becomes dominant [66]. Such microphase textures, based on self-assembly processes, provide a structural template on which inorganic particles can be

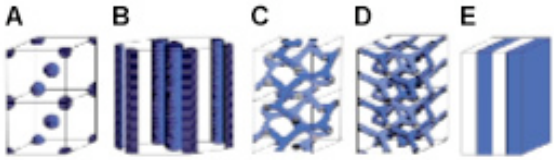

Figure 4: **Schematic phase diagrams of possible morphologies of diblock copolymers.** The resulting morphology depends on the volume fraction of the single blocks. A: spheres; B: cylinders; C: double gyroid; D: double diamond; E: lamellar. The white domains present the block A of the polymer, while the grey ones present the block B (adapted from [66]).

deposited [65, 76]. In this work an amphiphilic diblock copolymer, consisting of a non-polar polystyrene block and a polar poly-2-vinylpyridine block, is used for the fabrication of nanostructured surfaces (figure 5).

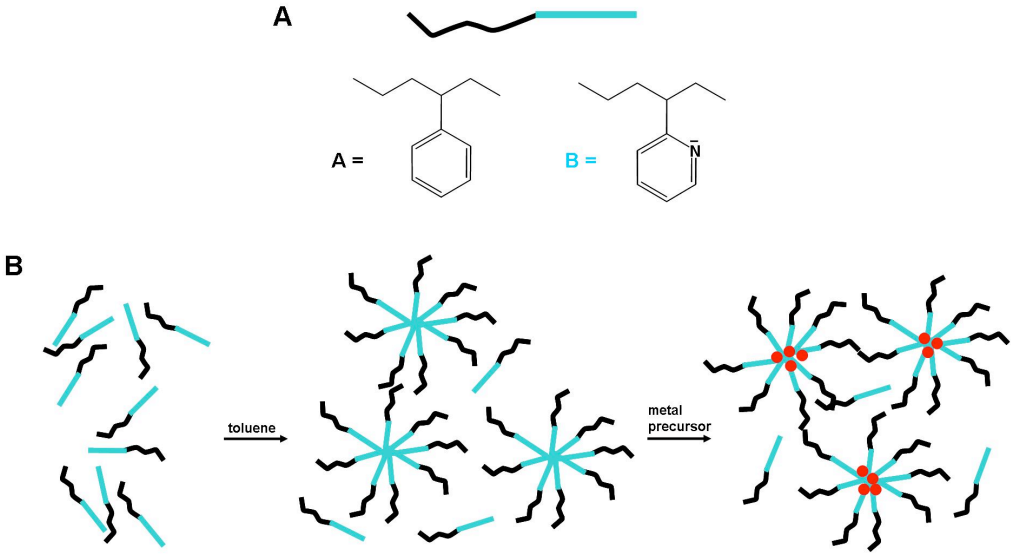

Figure 5: **Formation of micelles of diblock copolymers.** A: Diblock copolymer, consisting of a non polar polystyrene block (A), and a polar polyvinylpyridine block (B). B: Dissolving the polymer in toluene leads to the formation of inverted micelles as the concentration of the polymer is above the CMC. A metal salt is added to the solution, diffusing inside the core of the micelle.

If polystyrene-*block*-poly(2-vinylpyridine) block copolymers are dissolved in toluene they start to form spherical micelles, as toluene is a selective solvent for the styrene [77, 78]. The polar blocks agglomerate and reverse micelles with the non-polar styrene as a corona are formed [8, 9, 79]. Below a certain concentration, the block copolymers are dissolved in their unimeric form. If the concentration rises above a threshold, the critical micellar concentration

(CMC), micelles are formed (figure 6).

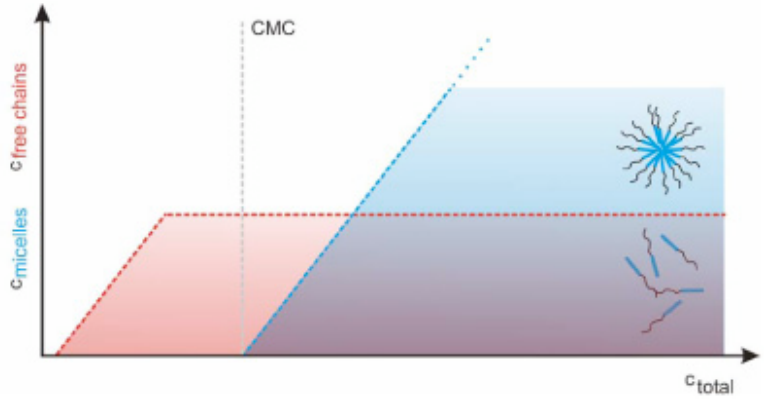

Figure 6: **Critical micellar concentration (CMC).** If the concentration c of a diblock copolymer in a selective solvent for one of the blocks rises over a threshold, micelles are forming.

The core-shell like structure of the micelles enables the incorporation of a metal salt into the polar core [80]. The vinyl pyridine gets ionized through the precursor and this shifts the thermodynamic equilibrium towards the micelle formation. If the vinyl pyridine is loaded by a metal salt, the micelles are stabilized. The CMC is shifted to lower concentration, but the concentration of the free chains remains constant [79, 81, 82].

Most of the experiments in this work are carried out working with tetrachloroaureatic acid ($HAuCl_4$) as a metal precursor to achieve gold nanoparticles on the surface. The gold salt is diffusing inside the core of the micelles [83]. To get a homogeneous distribution of the gold ions inside the micelles, a constant stirring is required. The size of the gold nanoparticles is controlled by the amount of metal precursor added to the micellar solution. The loading L, which defines the size of the obtained particles, gives the number of vinyl pyridine molecules $[VP]$, statistically occupied by one gold ion:

$$L = \frac{metal\,precursor}{[VP]} \tag{2}$$

To get a homogenous coating of solid substrates they can either be spin-coated or casted, by dipping the substrate inside the micellar solution. Dip coating enables a uniform coverage of different kinds of solid substrates over large areas with high accuracy [34]. In a first step, free polymer chains bind to the surface, leading to a formation of a polymer brush [67, 78]. During the retraction of the substrate out of the micellar solution the micelles form a monolayer on the substrate. They assemble into a quasi-hexagonal order. The driving force is the evaporation of the toluene at the immersion edge. Capillary forces, steric interactions, and electrostatic repulsion influence the final formation of the micelles on the surface [84]. During the dipping process the substrate is moved with a constant velocity. It is then treated by hydrogen

or oxygen plasma, which leads to a reduction of the metal precursor to the elementary metal or metal oxide followed by the complete removing of the polymer matrix [62]. The quasi-hexagonal pattern of the micelles is reflected in the pattern of the nano-particle arrays. The resulting particles are of spherical shape, which was shown in a side view transmission electron microscopy (TEM) image [63].

Block Copolymer Micellar Nanolithography has been successfully applied on many different substrates, such as glass, mica etc. [34, 85–87]. The only requirement to the substrate is that the material is stable in the solvent, which is here toluene, and resists the plasma conditions. These nanopatterned substrates are interesting for application as biosensors or rulers, due to the size dependence of the localized plasmon resonance of the gold particles [88–90]. The gold nanoparticles can also be used for the immobilization of different kind of molecules [91]. A biofunctionalization with enzymes, DNA, or peptides serves as platform for bioanalytical devices [92, 93]. Controlling the distance of immobilized nanoparticles enables also the control over the lateral distance between the biomolecules [94]. This allows studies of density or clustering effects in cell-adhesion [95]. The nanoparticles on the surface are also interesting as catalysts or as seeds for the growth of other nanoparticles.

In this work the nanostructured substrates, obtained by Block Copolymer Micellar Nanolithography, are used as platform for the controlled assembly of inorganic nanocrystals and virus nanoparticles. The gold particles on the surface serf as anchoring point. In a further approach, the nanoparticles are used as seeds for the growth of nanoparticles directly on a silicon surface.

1.3 Nanoparticles and Mesoscopic Phenomena

Semiconductor nanocrystals (NC) comprise a few hundreds to several thousands of atoms [96] and display unique properties, which resemble neither the bulk nor the molecular properties [97]. Furthermore, their physical characteristics strongly depend in the size and the shape of the NC [98]. Already during synthesis, the color of the reaction solution changes continuosly and this can be tracked back to the increasing size of the nanoparticles. In the absorption and fluorescence emission spectra of the NCs one can see a red shift in wavelength with smaller diameters (figure 7).

These nanomaterials do not have enough atoms to exhibit fully delocalized electrons and thus, their physical and electronic properties are strongly depended on the size [100, 101]. Especially in the regime below 10 nm the size plays an important role [36]. Studies of NCs of semiconductors or metals provide examples of how particle size can lead to the optimized materials performance. Essentially, two major effects are responsible for the size dependent properties in these NCs [18]. First, the fraction of surface atoms in NCs is very large in respect to the total number of atoms. Second, quantum size effects influence the electronic properties [36]. The high number of surface atoms compared to the overall number of atoms arises from the fact that the surface

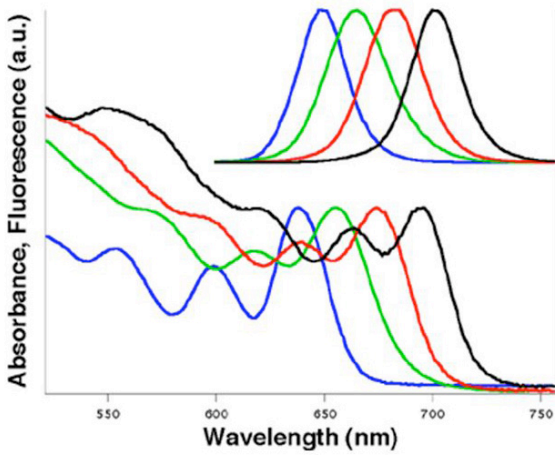

Figure 7: **Absorption and emission spectra of CdTe dots of different sizes.** For clarity the emission spectra are shifted upwards (from [99]).

of a sphere scales with the square of its radius r but its volume scales with r^3. The percentage of atoms, located at the surface, is extremely high for small particles, while this effect becomes less important for larger structures. Slight variations are observed for different shapes and crystalline structures of the materials (figure 8) [102].

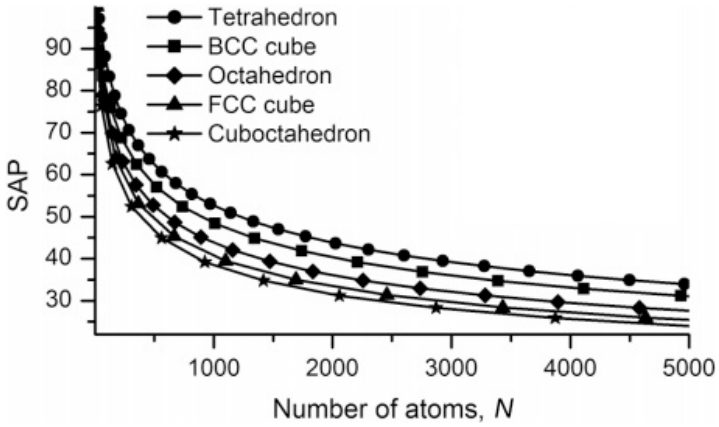

Figure 8: **Plot, showing the dependence of the surface atom percentage (SAP) in the total number of atoms in a crystal.** Shown are the numbers for different crystal morphologies and, in the case of a cube-shapedcrystalic case, for different close packing schemes. (from [102]).

Surface modifications contribute significantly to the free energy of the system [103–105]. Independent of the large number of surface atoms, semiconductor NCs with the same exterior bonding geometry as a known bulk phase often exhibit strong variations in electronic behavior.

These changes arise because of systematic variations in the density of elec-

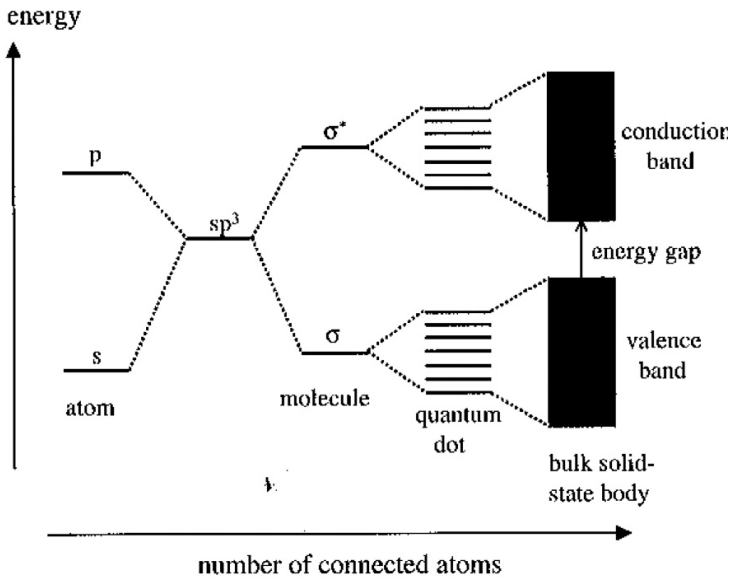

Figure 9: **Evolution of the density of states.** With increasing number of atoms in a system the density of states increases, starting from single atoms with two discrete levels, going to the bulk with the valence and the conduction band (from [106].

tronic energy levels as a function of size of the interior. NCs can be considered as intermediate between the molecular regime with its well-defined energy levels and the bulk materials with its continuous bands (figure 9) [18, 106].

The possibility of changing the semiconductor band gap by varying the particle size was one of the reasons for the great interest in research on semiconducting NCs. The band gap is the energy difference between the valence band and the conduction band. In a bulk semiconductor an electron (e^-) can be excited from the valence to the conduction band by absorption of a photon with energy larger than the band gap. This results in a hole (h^+) in the valence band. Influenced by each others charge, the electron and hole do not move independently from each other because of the Coulomb attraction. The formed e^--h^+ bound pair is called an exciton and has its lowest energy state slightly below the lower edge of the conducting band. At the same time its wave function is extended over several lattice spacings, i.e. the exciton radius (also termed Bohr radius) is large, since the effective masses of the charge carriers are small and the dielectric constant is high [96].

In Bulk CdS and CdSe the Bohr exciton radii are approximately 3 and 5 nm. Reduction of the particle size to a few nanometers produces the unusual situation that the exciton size can exceed the crystal dimensions. To fit into the NC, the charge carriers have to assume higher kinetic energies leading to an increasing band gap and quantization of the energy levels to discrete values. This phenomenon is commonly called quantum confinement effect [101]. With decreasing particle size, the energetic structure of the semiconducting

NCs changes from a band-like one to discrete levels. Therefore, in some cases a description by means of molecular orbital theory may be more appropriate, using the terms HOMO (highest occupied molecular orbital) and LUMO (lowest unoccupied molecular orbital) instead of conduction and valence band. This ambiguity in terminology reflects the properties of semiconducting NCs lie in between those of the corresponding bulk material and molecular compounds [36].

Besides the electronic properties also the unique optical properties are exhaustively explored. Absorption of a photon in a NC occurs, if energy exceeds the band gap. Due to quantum confinement decreasing the particle size results in a hypsochromic blue shift [100, 107]. The first exciton peak shows a sharp absorption. The position depends on the band gap and thus on the particle size. Therefore polydisperse samples typically exhibit only a shoulder in the absorption spectrum at the position of the exciton transition [108].

After absorbing a photon with an energy hν_e, the NCs emit light of a longer wavelength $h\nu_f$ after a brief interval, the fluorescence lifetime. The emitted photons have an energy corresponding to the band gap of the NCs and so the emission color can be changed by tuning the particle size. The full width at half maximum (FWHM) of the emission peaks is usually about 20 - 25 nm, which is narrow compared to organic fluorescent dyes.

By knowing the wavelength of absorption and emission it is also possible to calculate the diameter of the corresponding particles [109]. For spherical CdSe particles the diameter d in nm and the molar extinction coefficient ε can be calculated according to

$$d = (1,6122 \cdot 10^{-9})\lambda^4 - (2,675 \cdot 10^{-6})\lambda^3 + (1,6242 \cdot 10^{-3})\lambda^2 - 0,4227\lambda + 41,75 \tag{3}$$

$$\varepsilon = 5857 \cdot d^{2,65}\Big[\frac{1}{cm \cdot M}\Big] \tag{4}$$

λ is the position of the absorption peak in nm. Similar expressions can be also found for CdS and CdTe nanoparticles. There is no detectable influence of the synthetic methods, the surface ligands, or the solvents on the ε values of the NCs, as long as the size and composition of the inorganic NCs are the same [109]. Due to their versatility, NCs offer a wide spectrum of possible applications, ranging from photovoltaic devices to biological or medical applications [29, 32, 100, 110–112].

1.3.1 Preparation of Nanoparticles

The ability to prepare NCs in the gas phase by laser vaporization must be considered one of the great achievements of NC science [113, 114]. Early work on bare clusters in the 3 - 50 atom range has shown that remarkable changes occur in the electronic structure in this regime [36]. The first controlled synthesis

and systematic studies of nanometer sized semiconductor crystals were performed by Ekimov and Éfros already in 1982 [115,116]. They studied spherical semiconductor NCs, so called quantum dots, embedded in an insulating glass matrix. Ekimov's samples were the first to exhibit the quantum-confined blue shift of the first absorption (exciton) peak, varying as a^{-2} (with a being the NC radius) [115].

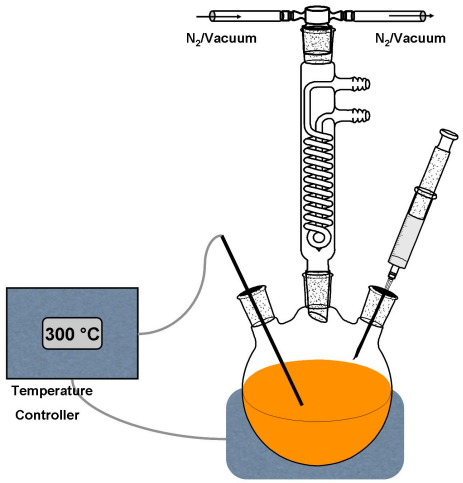

Figure 10: **Apparature for the synthesis of NCs at high temperature**. In a three-neck flask, one of the organometallic precursors (e.g. Cadmium stearate) and the surfactant are heated to the desired temperature. The second precursors (e.g. Se) is injected into the hot reaction solution.

The inorganic core of a semiconductor NC is usually capped by an organic outer layer of surfactant molecules, which provide sufficient repulsion between the crystals to prevent agglomeration [96]. The physical properties originate from the inorganic core, while the organic layer around is responsible for the chemical behavior of the particles. The synthesis of particles has been realized for many materials, such as indium [117], iron oxide [118], or ZnSe [119], but the II-VI semiconductors CdS and CdSe are widely studied. Their synthesis is based on high temperature (200 - 360 °C) thermolysis of organometallic precursors in the presence of stabilizing surfactants. Experimentally this is realized by injecting the organometallic precursors into a three-neck flask, containing the other component, the solvent, and the surfactant (figure 10). Also InP and GaAs particles have been successfully synthesized in such a way [120,121].

An important parameter in the reaction is the selection of the surfactant. They control the speed of the reaction by dynamic interaction with the surface of the growing crystal. New monomers can only attach to binding sites not occupied by surfactant molecules [99]. Generally, surfactants consist of a polar head group and a long non-polar alkane chain, which influences the dynamics of the growth. The polar head-group mainly affects the binding

efficiency, while the alkane chain influences the diffusion properties. Tri-*n*-octylphosphine oxide (TOPO) and tri-*n*-octylphosphine (TOP) are widely used as surfactants. Amines or carboxylic acids are also applied as surfactant molecules [99]. The TOPO molecules are conically shaped and are as densely packed on the NC surface as the curvature of the surface allows. Thus, the density increases with decreasing size. On a flat crystal surface only half of the binding sites are occupied whereas the surface is completely covered on a 2 nm diameter Cd crystallite [36, 122, 123].

At the surface of a pure semiconductor defects in the crystal structure can occur [124, 125]. These inhomogenities act as traps for electrons or holes. To overcome this, a passivation around the crystal is needed. The passivation either consists of an inorganic layer (e.g. SiO_2 around Si or $Al_{1-x}Ga_xAs$ with GaAs) or an organic one (e.g. phosphines or amines). This organic layer can be directly achieved by synthesizing the NCs in an organic solvent [36].

The growth of an inorganic shell around semiconductor NCs also suppresses the effect of blinking [126]. Blinking is a well-known phenomenon in NCs, where the photoluminescence of the particles is quenched by a non-radiative Auger recombination, during which the exciton energy is acquired by an extra electron or hole [127]. It occurs, when a nanocrystal is becoming ionized. A shell around the nanopartilce might suppress the ioniziation and thus the blinking of the crystal. By growing a shell of CdS around a CdSe nanocrystal, these "off" states can be reduced down to 20 ms [127].

1.3.2 Crystal Structure and Shape

As the above mentioned optical and electronic parameters not only depend on the size but also on the shape of the semiconducting NCs, a lot of research has been done to investigate differently shaped NCs [21–23, 25]. Shape control can be achieved by manipulating the growth kinetics. The crystal structure is highly anisotropic (Wurtzite structure, figure 11), thus the different crystal faces exhibit different reactivities [22].

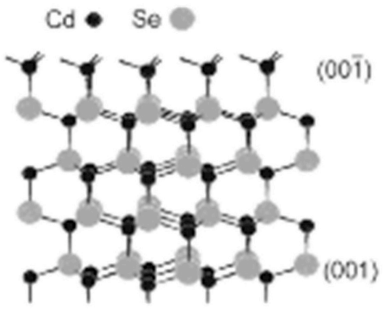

Figure 11: **Atomic model of CdSe in the wurtzite structure demonstrating the differences between the (001) and the (00$\bar{1}$) faces.** On the (001) face Cd atoms have only one dangling bond, while on the (00$\bar{1}$) face Cd atoms have three dangling bonds (from [21]).

Wurtzite CdSe is intrinsically an anisotropic material with a unique c-axis. When the overall growth rate is fast, growth is generally fastest along this axis. If the overall growth rate is low, a nearly spherical, but still faceted shape minimizing the surface area is favored [21]. If the growth rate is increased significantly, the result is a rod-like faceted shape, where the long axis is the c-axis of the wurtzite crystal structure [22]. Systematic variation in the surfactants can thus control the shape of semiconductor NCs in this system [21].

During the growth of spherical CdSe NCs in hot TOPO the surfactants dynamically adsorb to the growing crystallites, allowing atoms to add and substract for high crystallinity [128, 129]. This enables the growing crystallites to anneal, resulting in good crystallinity, while suppressing particle aggregation. The relative growth rates of the different faces can be controlled by suitable variation of the ratio of TOPO, hexylphosphonic acid (HPA), and octadecylphosphonic acid (ODPA) [22]. Changing the ratios of the three allows the controlled formation of CdSe NCs with rod, arrow, teardrop, and tetrapod shapes [21, 130].

1.3.3 Heterostructures

More complex NCs are synthesized out of a combination of two or more inorganic materials (figure 12) [131, 132]. In the core/shell NCs an additional inorganic material is uniformly grown around a NC core (figure 12A). It can be used to increase the robustness and the fluorescence efficiency of a semiconductor core [126, 127, 131, 133], and to provide a surface to which molecules can attach easily [91].

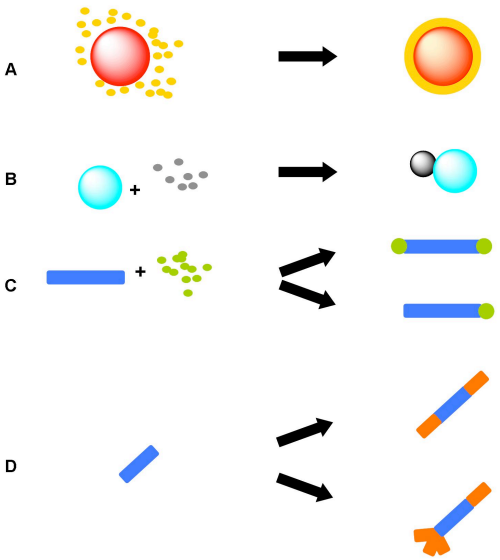

Figure 12: **Scheme of possibilities for the formation of hybrid structures.** A Core/shell particles; B: Heterodimers; C: Dumbbells; D: Rods or branched NCs out of different material (adapted from [130]).

More elaborate approaches, which have been reported recently, can lead to NCs with a finer topological control of their composition. One example is the NC heterodimer, in which two domains of different materials are joined together (see also chapter 1.4.2) through a specific facet (figure 12B). Possible combinations are the grouping of a magnetic and a fluorescent NC, or two metal sections and so on [134, 135]. Another example is the dumbbell shaped NC (figure 12C), made of a semiconductor nanorod and one or two domains of another material, such as a metal, like gold, or another semiconductor, grown either on one or on both tips of the nanorod [136, 137]. This growth scheme exploits the anisotropy of the wurtzite structure as described above. In the same way as the growth can be favoured along the c-axis also the deposition of a second material might be ffavoured on these sites. Additionally in some cases even the small difference in surface energy between the two +/- (001) facets can become evident as the possibility to choose between the growth of material on only one tip or on both tips of the nanorod [138].

Further progress has also been done in the elaboration of linear and branched NCs with sections made of different semiconductors (figure 12D) [139], or oligomers with several spherical domains of different material attached to each other in a way that resembles the spatial organization of atoms that form molecules [140, 141].

1.3.4 CdSe Rods

The synthesis of shape-controlled nanocrystals has been realized by Ellis already in 1964, by growing mercury whiskers by the use of vapor-liquid-solid growth [142]. In solution the anisotropic growth of CdSe particles has been successfully realized, by diluting a cadmium and a selenium precursor in tributyl or trioctyl phosphine and injecting into hot, liquid TOPO [22] (see also section 1.3.1). The resulting rods are monodisperse in diameter and length [20].

Growth of Gold Domains The two basal facets of the Wurtzite structured rods expose unsaturated and unpassivated bonds. Therefore the growth of gold domains occurs specifically at the ends of the CdSe rods. By controlling the reaction conditions it is possible to grow the gold domain either to one or to both ends of the rod [136, 137]. If the gold tip grows on one or on both sides of the rod is dependent on the amount of gold precursor ($AuCl_3$) present in the solution. If the molar ration between the CdSe rods and the gold is low, the gold tips grow at both ends of the rods. Adding large excess of the gold results in matchstick like structure, with only one gold tip. This effect can be explained by a ripening process [137]. In the beginning of the growth the gold starts growing at both ends of the CdSe rod. Both tips are growing until a critical size is reached. At this time, one tip grows larger than the other one. The larger tip continues to grow while the other tip is dissolving. Kinetics as well as energetic contributions to the fluctuation leads to ripening and one-sided growth. Both are suppressed for low gold concentrations, leading to

nano dumbbells [137].

1.4 Magnetic NCs

Magnetic NCs are widely explored in the last years due to their potential application in high density magnetic storage [33, 103, 143–148]. The density of information, stored on a media has reached the value of 100 Gbits/in^2 [149]. For densities above the Tbits/in$_2$ the lateral size of each bit should be smaller than 10 nm. Each particle must be precisely addressable and there must not be any interaction effect between the particles. A system based on the self assembly of magnetic nanorods perpendicular to the plane would be a solution for achieving a large density [150]. Also in biomedical applications magnetic particles are of interest. Cells can take up the particles and application of a magnetic field enables the sorting of cells or analysis in magnetic resonance tomography [151].

1.4.1 Co particles

Co nanorods can be synthesized by decomposition of an organometallic compound under hydrogen in the presence of a long amine and a long acid [152]. Decomposition of [CoN(SiMe$_3$)$_{22}$] under H_2 in the presence of lauric acid (LA) and hexadecylamine (HDA) results in the formation of Co nanorods [153,154], which can be functionalized with a gold tip in further reactions [155]. The resulting nanorods are homogenous in diameter while their length is adjustable from 40 - 100 nm by the reaction conditions [150]. They are crystalline and they spontaneously organize side by side along their long axis perpendicular when dried on a surface, e.g. on a TEM grid. These nanorod lattices are ferromagnetic at room temperature. Their strong coercive field is characteristic and is a consequence of their large magnetic anisotropy (magnetocrystalline and shape). As a consequence of their large size, they conserve their ferromagnetic properties above room temperature [150]. When the density of particles per unit area is higher than a determined threshold, the 2D self-assemblies behave as a continous ferromagnetic thin film [33].

Growth of Gold Domains The selective growth of Au on the Co nanorods requires the promotion of (i) the deposition of Au on Co over galvanic displacements of cobalt by gold and (ii) heterogeneous growth over homogenous nucleation [156]. As homogenous nucleation is energetically more demanding than growth on preformed NCs, it is possible to find conditions that allow the selective growth of Au on Co nanorods [155]. Temperature and nature of the reducing agents, the choice of the gold precursor, and the surface chemistry of the cobalt nanorods can influence the selectivity. Thus the concentration and nature of the surface ligands, specifically their affinity for selected surfaces and their dynamics, may allow complete or face selected passivation. Using [AuClPPh$_3$] as gold precursor and keeping the reaction temperature above 40

°C results in the specific growth of Au nanoparticles at the end of the Co rods, while at lower temperature, nonselective deposition of Au particles over the whole nanorod structure is observed [155]. The dimensions of the particles are not changed during the growth, indicating a pure heterogenous growth mechanism. The Cobalt serves as seed for the Au growth. For the gold tipped nanorods, the (111) gold lattice planes grow parallel to the direction of the (002) planes of the Co structure. Regarding the lattice parameters of 2,35 Å (*hkl*) for gold and 2,02 Å (*hkl*) for cobalt, an epitaxial growth is not possible. For the gold, growing at the side of the nanorods, the gold (002) planes (d(*hkl*) = 2,04 Å) grow on the (002) ones of cobalt. Epitaxial growth is here possible [155]. Functionalization of metal-tipped Co nanorods could facilitate their attachment and organization on flat substrates or their use in biological and medical applications.

1.4.2 $CoPt_3$ Nanocytals

Spherical $CoPt_3$ nanoparticles are synthesized by reduction of platinum acetylacetonate and thermocompsition of cobalt carbonyl in the presence of 1-adamantanecarboxylic acid and hexadecylamine. The mean particle size can be varied from 1,5 to 7,2 nm [157, 158]. The synthesized $CoPt_3$ particles represent single crystal domains and display a chemically disordered face-centered cubic (fcc) structure. The particles are stable in non polar solvents under normal atmosphere for several months without precipitating [157].

Growth of Gold Domains The growth of a gold domain on presynthesized $CoPt_3$ NCs has successfully been realized by working with gold(III)chloride ($AuCl_3$) as a precursor [151]. Structural characterization shows that the gold domain as well as the $CoPt_3$ domain have cubic fcc Bravais lattice, sharing a common (111), (100), or (110) facet. The facet is depending on the size of the initial $CoPt_3$ seeds. The growth of gold on $CoPt_3$ is highly epitaxial. There is no formation of alloys observable, the growth of a gold domain does not influence the magnetic properties of the particle [151]. The growth mechanism of the gold domains on $CoPt_3$ NCs is still not completely understood. The gold only grows on one facet on the originally synthesized NC. The one-side growth of gold on $CoPt_3$ is not similar to the one-sided growth of gold on CdSe nanorods as no intermediates with two gold domains could be isolated [136]. Also the initial formation of a gold shell, which forms the gold domain in a dewetting process, is not applicable [135, 159]. According to this mechanism a thin shell grows uniformly around the particle and then coalesces into a single domain. A shell formation could not be observed in the growth process of the heterodimer structure [151].

1.5 Biomolecules

Hybrid nanostructures, containing inorganic materials, such as nanocrystals, with the biological functions, provided by proteins or DNA, constitute a promising area of nanotechnology [160–162]. Biology creates molecules with a high control on the size and the structure. Their physicochemical properties as well as their capability for self assembly based recognition are constrained [163]. DNA has been exploited as template for the assembly of metal ions into conducting wires, because of its precisely controlled size and structure [143, 164]. The physicochemical properties of lipids or polypeptides have led to the fabrication of vesicles and membranes by pure self-assembly. Molecular based self-assembly of virus particles can be used for novel macromolecular architectures or molecular machines.

1.5.1 Desoxyribose Nucleic Acid (DNA)

DNA contains the genetic instructions of living organism. The main role of DNA molecules is the long term storage of information. Its structure was first described by Watson and Crick in 1953 [165]. DNA consists of 4 different nucleotides assembled in a polymer chain. The backbone is formed of a sugar (2-desoxyribose) and phosphate groups. Attached to each sugar is one of four possible bases: adenine, thymine, guanine, and cytosine (figure 13).

Two of these strands are oriented anti-parallel to each other, forming a helical structure. The asymmetric ends of the DNA strands are referred as the five prime (5′) and three prime (3′) ends, with the 5′ end carrying a phosphate group and the 3′ end presenting a terminal hydroxyl group (figure 13). They interact with each other by hydrogen bonds between the bases. According to their structure, only cytosine and guanine can interact with each other, and adenine with thymine. The DNA chain has a diameter of 2,2 to 2,6 nm and one nucleotide unit is about 0,33 nm long [166]. If the sugar in the backbone is ribose instead of desoxyribose, the resulting molecule is called ribose nucleic acid (RNA). Modern biology and biochemistry make intensive use of recombinant DNA technology. They can be injected into cells or bacteria in the form of plasmids [167]. The genetically modified cells of bacteria can be used to produce products such as recombinant proteins, or be used in medical research [168]. Also in nanotechnology, DNA plays a major role. The use as molecular ruler has successfully been introduced, as well as the design of DNA chips. For this, DNA of different length has been immobilized on solid substrates. The effect of DNA length on the assembly of has been investigated [169], as well as the hybridization of ssDNA, immobilized on surfaces [170]. The characterization of DNA on surfaces is possible by staining the DNA strand with a fluorescent dye, or by AFM imaging [171, 172]. Highly complex 2D and 3D structures of DNA have been realized, where also single molecules can be immobilized at defined positions [173]. Furthermore gold nanoparticles have been covered by DNA [174].

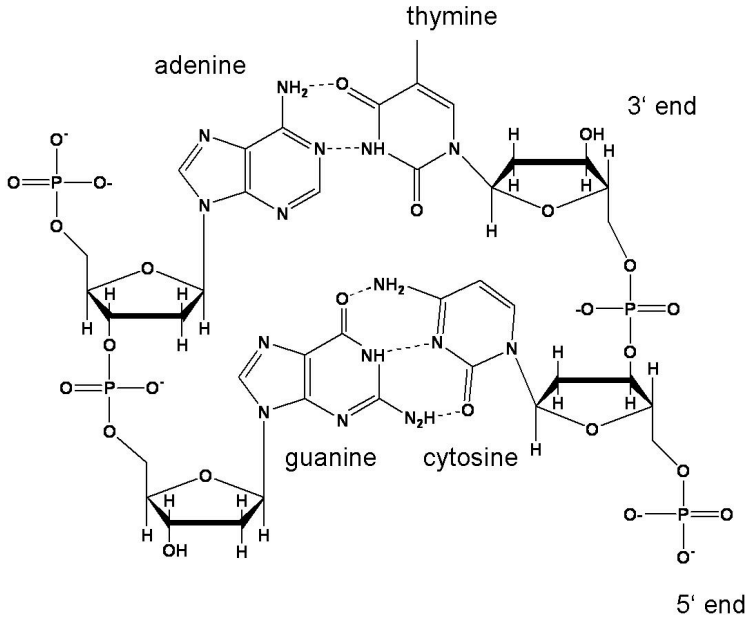

Figure 13: **Schematic of two DNA molecules, interacting with each other over hydrogen bonds in the bases.** 4 different bases are present in DNA: adenine, thymine, guanine, and cytosine. Due to their structure, only adenine and thymine can form hydrogen bonds, as well as guanine with cytosine. The backbone is formed of a sugar and phosphate groups.

1.5.2 Viral Nanoparticles (VNPs)

Viral Nanoparticles (VNPs) are of great interest as building blocks for film assemblies for new materials. 2D as well as 3D crystals can be obtained by the self-assembly of the particles [175, 176]. Two VNPs from plants are in the center of research of many groups, the tobacco mosaic virus (TMV) and the cowpea mosaic virus (CPMV).

The TMV is a rod like virus, with a length of about 300 nm, which is adjustable by genetic modifiation of the virus. Both ends of the virus contain a free single stranded RNA, where the base sequence is known [177]. This enables the functionalization specifically at the ends of the virus. The longest part of the RNA is coated by a protein, which can be removed by different methods [178, 179].

The CPMV is a virus with a spherical form. The structure is known to nearly atomic resolution and the genetic properties are well characterized [180, 181]. The coat protein of these 30 nm diameter particles consists of 60 copies of two different subunits, the small and the large. The small subunit consists of the A domain, while the large subunit can be devided in the B and C domain [160]. As the capsids are robust, they maintain their integrity at 60 °C for one hour and resist pH values in the range from 3,5 to 9,0 [182]. Functional groups are present on the interior and the exterior surface, making them open for different kinds of functionalization. Organometallic complexes, quantum dots, and biomolecules such as biotin have successfully been immobilized on the virus nanoparticles [160, 182, 183]. CPMV, modified with a histidine-tag, have been successfully modified on surfaces over a Ni-NTA (nickel nitrilo triacetic acid) complex, which allows the study of the pattern morphology by atomic force microscopy [184].

Part II
Materials and Methods

2 Materials and Methods

2.1 Analysis Methods

To characterize nanometer sized materials highly accurate spectroscopic and microscopic methods are required. As the resolution of optical microscopy is limited by the wavelength of light mainly electron microscopy (scanning electron microscopy (SEM) and (scanning) transmission electron microscopy ((S)TEM) was used to analyze the substrates. The resolution of high precision electron microscopes is less than 1 nm [185]. It is limited by aberrations of the electron lenses. SEM images were also used to characterize nanopatterned substrates by analyzing the interparticle distance as well as the quality of the hexagonal pattern. The surphace morphology can be also determined by mechanical sensing, which is used in atomic force microscopy (AFM). The resolution is limited by the diameter of the tip, which is sensing the surface. To characterize the surface properties in ensemble measurements, x-ray photoelectron spectroscopy (XPS), quartz-crystal microbalance with dissipation monitoring (QCM-D) and optical absorption and fluorescence measurements were performed. XPS gives information about the chemical composition on the surface, while in QCM-D in-situ measurements are possible.

2.1.1 Electron Microscopy

Mainly scanning electron microscopy (SEM) was used to characterize the substrates. An electron beam is here focused in the vacuum onto the probe material. The electrons interact with the top layer of the substrate, leading to different interactions between the electrons and the probe material (figure 14).

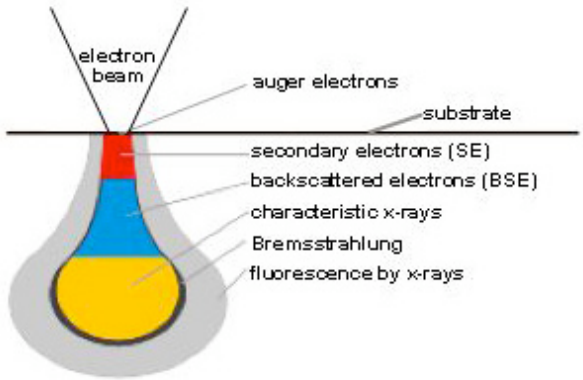

Figure 14: **Interaction of the electron beam with the surface.** The primary electron beam penetrates the surface, resulting in the formation of secondary electrons (SE), backscattered electrons (BSE), characteristic x-rays, Bremsstrahlung, fluorescence x-rays, and auger electrons. SE and BSE can be used for imaging.

In SEM secondary electrons (SE) and back-scattered electrons (BSE) are used for imaging. The SEs result from inelastic interaction with the probe material, where the BSEs are the outcome from elastic scattering. When high energy primary electrons (PE) from the source penetrate the surface, they undergo elastic scattering with electrons from the material or elastic scattering with the nuclei. The higher the atomic number of the investigated elements the more likely that backscattering will occur. The primary current can be divided into three parts:

$$i_0 = i_{BSE} + i_{SE} + i_{SC} \tag{5}$$

where i_{BSE} and i_{SE} are the fractions for the back scattered and secondary electrons and isc is the current which goes through the specimen. These scattered (SC) electrons distribute in a thick substrate. If this is thin enough, the electrons transmit and can be collected at the backside of the specimen. This is used in transmission electron microscopy (TEM).

The electrons for scanning the probe surface may be generated from a conducting material by heating it to a specific point at which the energy of the electrons is larger than the work function barrier of the conductor (thermionic source), or by applying a strong electric field that causes electrons to tunnel through the barrier (field emission source). SEM measurements in this work were done using a Ultra 55 electron microscope (Zeiss SMT, Oberkochen, Germany) with a field emission gun (FE-SEM) working with accelerating voltages ranging from 0.1 to 30 kV. The images were recorded with an In-lense detector.

For image acquisition in the SEM, the surface needs to be conductive. To prevent charging, non-conductive glass substrates were coated with a thin layer of carbon (Bal-TEC Med020 Modular High Vacuum Coating System, Witte, Germany).

2.1.2 Order Parameter

The micelles assemble on the surface in a quasi-hexagonal arrangement, reflected by the position of the gold dots. The quality of the order can be judged by fast Fourier Transformation (FT) analysis of the SEM images; ideally the FT image also shows an hexagonal arrangement. For a statistical analysis of the structural parameters, including the order and the interparticle distance, further image analysis is needed.

The arrangement of particles, self-assembled on a surface, can be somewhere between completely random and a crystalline order. The random orientation is similar to an amorphous structure, without any long-range order, while in the occurrence of crystalline assembly, long-range order can be assumed. To quantify the hexagonal arrangement of the micelles on the surface, the order parameter $|\psi|$ of a pattern was determined by considering the nearest particles around a center one. The local order is then described by

$$\psi_6(\vec{r}) = \frac{1}{N}\sum_j \sum_k exp(6i\theta_{jk}) \tag{6}$$

θ_{jk} is the inclination of the vector between the two particles j and k. N is the number of all nanoparticles over which the local order is measured. For a perfect hexagonal order $|\psi|$ equals one. For decreasing order, as an effect of structural disorder, the value approaches zero.

The order parameter and the average interparticle distance of metallic nanoparticle arrays can thus be evaluated. SE micrographs of this work have been analyzed by ImageJ[1] (Research Services Branch, image analysis software, NIH, USA), giving the order parameter $|\psi|$ as well as the average interparticle distance of the array.

2.1.3 Atomic Force Microscopy

The atomic force microscopy (AFM) translates interactions on an atomic level into mechanical forces exercized on a cantilever. It was first investigated by Binnig et al. in 1986 [186]. A sharp tip on a flexible cantilever is brought in close proximity of the substrate. Attractive as well as repulsion forces between the sample and the tip can now be measured. Standard AFM tips are of silicon nitride with a tip diameter of 10 to 50 nm.

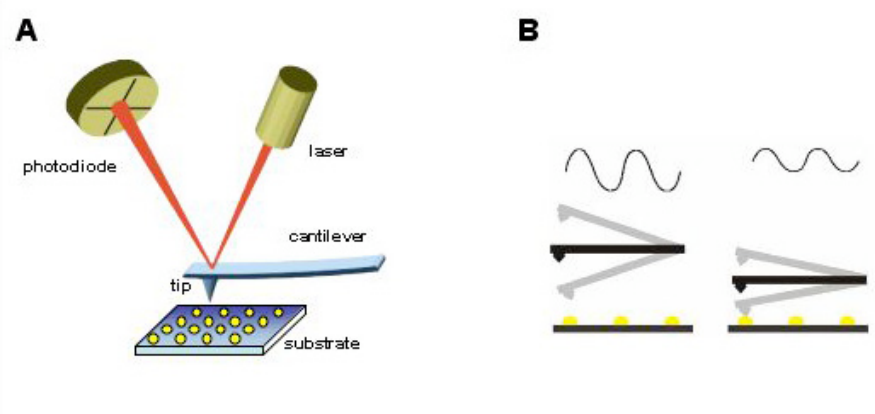

Figure 15: **Schematical of the operation mode of an atomic force microscope.** A: A tip on a cantilever is sensing the surface. The deflection of the cantilever is sensed by a laser. B: In the tapping mode the damping of the resonance of the cantilever is detected, which is caused by attractive and repulsive interactions between the tip and the surface.

For the measurement the cantilever is scanned over a certain surface area (figure 15A). For imaging, mainly two measuring modes are used: contact mode and tapping mode. In the contact mode, the tip touches the substrate.

[1]Plugin for ImageJ kindly provided by Dr. P. Girard, EMBL, Heidelberg, Germany.

Movements of the cantilever reflect the roughness in the surface. The deflection is measured with a laser, using a spot, reflected from the top of the cantilever into a sectioned photodiode. In tapping mode the tip is oscillating directly over the surface (figure 15B). The oscillation frequency is close to the resonance frequency of the cantilever. Bringing the tip closer to the substrate influences the vibration. Damping in the oscillation amplitude give information about topographic properties, while shifts in the phase can be related to the stiffness of the underlying material.

AFM measurements presented in this work were carried out in tapping mode with an Asylum Research MFP 3D microscope.

2.1.4 X-Ray Photoelectron Spectroscopy (XPS)

In X-ray photoelectron spectroscopy (XPS) information about the chemical composition of a surface is obtained. A X-ray beam with a low penetration depth into a solid is focused on a substrate ((figure 16). Standard radiation sources are Mg Kα or Al Kα, as their penetration depth is in the range of 1 – 10 μm. The special resolution of XPS measurements is about 1 mm^2. The X-ray photons react with the atoms on the surface. Electrons are emitted by the photoelectric effect. The kinetic energy E_{kin} of the emitted electrons is given by

$$E_{kin} = h\nu - BE - \phi_S \tag{7}$$

where $h\nu$ is the energy of the incident photon, BE the binding energy of the atomic orbital from which the electron originates, and ϕ_S the work function of the spectrometer [187]. The energy of the emitted electrons reflects the binding energy of the atom. As each element has unique binding properties, XPS can be used for the determination of the elements on the surface. By calibration it is also possible to get quantitative analysis of the components on the substrate.

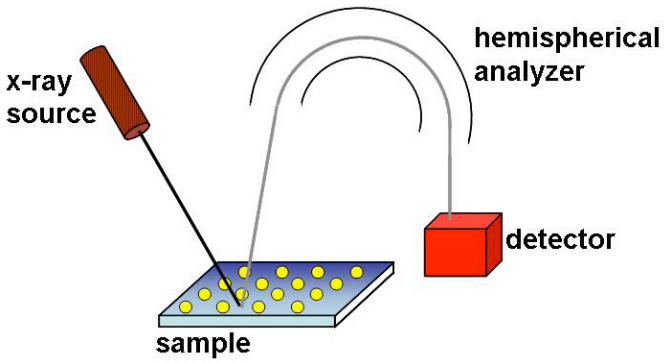

Figure 16: **Schematic of the working principle of a x-ray photoelectron spectroscope.** Photons from a X-ray source penetrate the surface, resulting in the emission of photoelectrons. Through an hemispherical analyzer electrons of a defined energy are send onto a detector.

Variations in the elemental binding energies arise from differences in the chemical surrounding and the polarization of the compound. These energetical shifts allow the identification of different chemical states of the materials.

XPS measurements were performed with a Spec. Hemispherical analyzer, equipped with a Mg Kα radiation source (1253,6 eV). Emitted photoelectrons were detected by a multichannel detector at a pass energy of 96 eV for the survey and 48 eV for the narrow scanned spectra. The step size was 0,5 for the survey and 0,1 for the narrow spectra with a repetition rate of 3, respectively 5 for the narrow spectra.

2.1.5 Quartz Crystal Microbalance with Dissipation Monitoring (QCM-D)

Quartz crystal microbalance with dissipation monitoring (QCM-D) measurements can be used for the in situ observation of the dynamics of film formation. It is a thickness-shear mode resonator, where the shear deformation of a quartz crystal is quantified. If molecules attach to the crystal, the mass is increasing and thus the resonance frequency is changing. Measuring the changes of the resonance frequency allows for the calculation of the adsorbed wet mass, according to Sauerbrey's equation [188]:

$$\Delta m = -C \cdot \Delta f \tag{8}$$

The mass sensitivity constant C is $17,7 ng \cdot cm^{-2} Hz^{-1}$. Sauerbrey's equation is only valid, if the adsorbed mass is small compared to that of the crystal and if the adsorbed film is rigid and homogenously distributed [189]. With the dissipation monitoring it is possible to obtain information about the viscoelastic properties of the adsorbed film. A purely elastic material will deform under stress. After that returns into the original shape. An ideal fluid in contrast is not showing any resistance against shear stress. Real materials have properties somewhere inbetween. Two models have been developed to describe the viscoelastic properties of materials: the Maxwell model and the Voigt model [190]. In both models a purely viscous damper and a purely elastic spring are used to describe the viscoelastic properties. In the Maxwell model, the two components are connected in series. Connecting the two in parallel results in the Voigt model. Both models can be used to calculate the thickness of an absorbed film in QCM-D measurements.

QCM-D experiments were performed in an E4 qcm-d from q-sense (Vaestra Froelunda, Sweden). The SiO_2 crystals as well the ones with a gold layer on top had a fundamental frequency of 4,95 MHz. The 5th harmonic was analyzed.

2.1.6 Optical Spectroscopy / Microscopy

An electron can be excited from the ground state S_0 to the first electronically excited state S_1 after absorbing a photon with an energy $E = h \cdot \nu_{ex}$. A molecule in its excited state can relax by various ways. In a non-radiative relaxation the

energy is dissipated as heat (vibrations) to the solvent. Conversion to a triplet state and subsequent relaxation causes phosphorescence. Fluorescence occurs when the electron relaxes back into the ground state, emitting a photon with an energy of $E = h \cdot \nu_{em}$. The energy of the emitted photon is less than the adsorbed one. The wavelength is shifted to longer wavelengths, as parts of the energy are lost through vibration (Stoke's shift). The Jablonski diagram (figure 17) describes most of the relaxation mechanisms for excited state molecules.

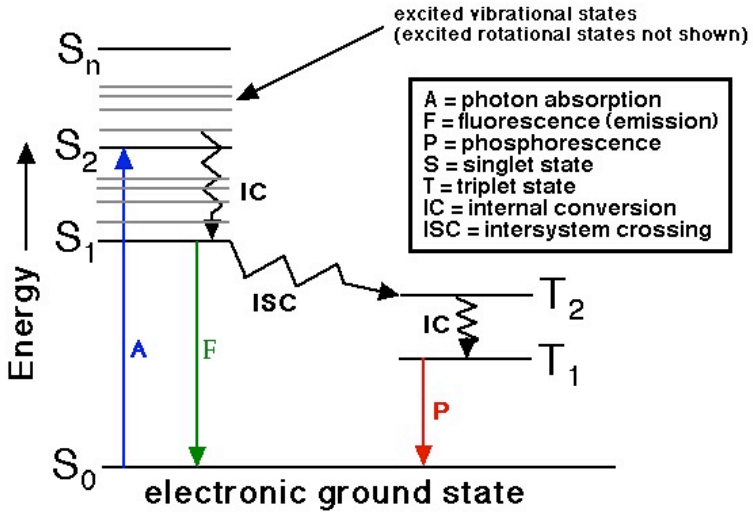

Figure 17: **Jablonski diagram, showing possible relaxation mechanisms for a molecule to relax from ist excited state into the ground state.** Fluorescence occurs, if a photon relaxes from S_1 to the ground state S_0. The energy of the emitted photon is less than the one of the absorbed photon.

Absorption measurements in this work have been performed with a Cary 4000 UV/Vis spectrometer from Varian (Darmstadt, Germany) A Fluorolog from HORIBA Jobin Yvan GmbH (Munich, Germany) was used for fluorescence spectroscopy. Fluorescent microscopy images have been performed on a Delta Vision Imaging System containing an Olympus IX 71 microscope from Applied Precision (Issaquah, Washington, USA).

2.2 Chemicals

Most chemicals have been used as purchased. Only the solvents for the polymer solutions (toluene p.a. and xylene p.a.) as well as the anisole have been dried over a molecular sieve.

The diblock copolymers for the micellar solutions are from Polymersource Inc. (Montreal, Canada).

From Merck KG (Darmstadt, Germany) we used toluene p.a., hydrogen per-

oxide (30 %), hexachloroplatinic(IV)acid (H_2PtCl_6,), NaOH solid, tetrahydrofurane extra pure (THF), ortho xylene p.a., meta xylene p.a., and para xylene p.a.. Methanol and acetone were used in VLSI quality from BASF (Ludwigshafen, Germany), isopropanol in p.a. quality from J.T.Baker (Deventer, Netherlands).

From Sigma-Aldrich (Steinheim, Germany) we received tetrachloroaureate (III) trihydrate ($HAuCl_4$), gold(III)chloride ($AuCl_3$), dodecylamine (DDA), didodecyldimethylammonium bromide (DDAB), 2-iminothiolane hydrochloride 98 % (TLC grade), biphenyl-6,6'-dithiol 95 %, tris(2-carboxyethyl) phosphine hydrochloride (TCEP, 0,5 M solution), mercapto-un-decanoic acid 95 % (MUA), lauric acid 98 % (LA), hexadecyl amine (HDA), 1,3-diisopropylbenzene 96 %, poly-(1-vinylpyrrolidone)-graft-(1-hexadecane), sodium (bis-trimethylsilyl)amide ($Na[N(SiMe_3)_2]$) (0,6 M solution in toluene), boric acid, sodium tetraborate decahydrat, 2-mercaptoethanol, and *n*-buthyl lithium (*n*-BuLi, 1,6 M solution in hexane). Triethylamine extra dry, hexamethyl disilazane ($NH(SiMe_3)_2$), and tri-*n*-octyl phosphine (TOP) were purchased from Fluka (Sigma-Aldrich, Steinheim, Germany). Cadmium stearate (min. 90 %) and tri-*n*-octyl phosphine oxide 99 % (TOPO) were obtained from Strem Chemicals Inc. (Newburyport, MA, USA).

Glass slides (20x20 mm), conc. sulfuric acid 95 – 98 %, 3 Å molecular sieve ("Perlform"), and diethyl ether p.a. were purchased form Karl Roth & Co. (Karlsruhe, Germany). Extra dry solvents, for working inside the glove box, were purchased from Acros (New Jersey, USA). In particular it was toluene, methanol, and chloroform. Also ethyl acetate p.a. and pure pentane were received from this company. 1,6-hexandeithiol 97 %, mercaptopropionic acid 99 % (MPA), bismuth(III)chloride 98 % ($BiCl_3$), and anisole 99 % were received from Alfa Aesar (Karlsruhe, Germany).

From Invitrogen (Karlsruhe, Germany) we used streptavidin and Alexa Fluor 488 labelled streptavidin, Alexa Fluor 532 labelled biotin, and SYBR Green I. Also the tablets, to obtain 150 mM PBS solution, were from Invitrogen. The TE-buffer concntrate (100x concentrate) was delivered by Serva Electrophoresis GmbH (Heidelberg, Germany). The Thiol Determination Kit, as well as EDC and sulfo-NHS were purchased from Perbio Science Deutschland GmbH (Bonn, Germany). The modified ssDNA was from eurofins MWG operon (Ebersberg, Germany). Biotin doped vesicles were from Avanti Polar Liquids Inc. (Alabaster, AL, USA).

The cut off columns were purchased from Millipore (Schwalbach/Ts., Germany), while the NAP 25 and NAP 10 comlumns were form GE Healthcare (Munich, Germany). Si-wafer in a 100 orientation (p-doped, one side polished, containing an oxide layer) were sourced from Topsil (Kaltenkirchen, Germany) The Millipore water ($R < 18M\Omega$) was obtained from a Gen-pure Milliporewater system from TKA GmbH (Niederelbert, Germany).

2.3 Experimental Section

2.3.1 Micellar Solution

Toluene p.a. was tried over a 3 Å molecular sieve and transferred into a glove box (M. Braun, processing gas: nitrogen). The same was done with the xylene isomers. Poly(styrene(x)-*block*-(2-vinylpyridine)(y)), PS(x)-*b*-P2VP(y), diblock copolymers are dissolved in the dried solvent. Defined amounts of water are added and the solution is stirred on a magnetic stirrer for 24 hours to form uniform micelles. A list of commonly used polymers is shown in table 1.

Table 1: List of PS (x)-b-P2VP (y) diblock copolymers, used in this work. x and y are the number of styrene and vinylpyridine monomers, Mn is the molecular weight of the single blocks.

PS(x)-*b*-P2VP(y)	Mn(PS) [g mol^{-1}]	Mn(P2VP) [g mol^{-1}]	Mn/Mw
245-*b*-223	25500	23500	1,05
501-*b*-235	52100	31000	1,05
1056-*b*-495	110000	52000	1,15
1824-*b*-523	190000	55000	1,10
2076-*b*-571	216000	60000	1,05
5355-*b*-714	557000	75000	1,05

Used glassware and the stirrers are cleaned with piranha solution before transferring them into the glove box.

After the polymer is completely dissolved in toluene, stoichiometric amounts of the metallic precursor were added. To dissolve it completely, the solution was stirred for 24h. The amount of added metal salt, defined by the loading parameter L, can be calculated after:

$$m_{precursor} = \frac{m_{PS-b-P2VP} \cdot M_{precursor} \cdot [VP] \cdot L}{M_{PS-b-P2VP}} \tag{9}$$

VP is the number of vinylpyridine molecules. Most experiments were carried out by working with Tetrachloroaureate(III)trihydrate ($HAuCl_4$) in order to create a gold-dot nanopattern. To generate a nanopattern of platinmum, hexachloroplatinic(IV)acid (H_2PtCl_6) is used. The loading parameter was usually set to $L = 0,5$ for both metal precursors.

2.3.2 Substrate Preparation

The glass cover slides as well as the Si-wafers are cleaned in hot piranha (30% H_2O_2 : conc. H_2SO_4 in a ratio of 1:3) for at least 30 minutes. Piranha is a strongly oxidizing solution, which removes organic residues from the surfaces. The substrates are then rinsed in Millipore water and treated for three minutes in ultrasound. Afterwards they are again rinsed with Millipore water and tried

with nitrogen prior to use. The cleaned substrates are hydrophilic and free of organic and inorganic residues.

Mono micellar films on glass or silicon substrates are prepared by dipping them into a micellar solution. They are retracted with a constant speed and dried in air. The retraction velocity was controlled by adjusting the voltage of the power supply of the motor of the dipping machine. For most experiments the speed was set to 12 mm/min. Finally the samples are treated in hydrogen plasma[2]. During the plasma treatment the metal particles forme and the polymer is removed. The retraction velocity was manually controlled by adjustment of the voltage setting.

The zero-mode waveguides (Pacific Biosciences, Menlo Park, CA, USA) are cleaned with isopropanol and acetone. After drying in a steam of nitrogen they are cleaned in a short oxygen plasma step at 0,3 mbar and a power of 150 Watt. To get the micelles inside structures in the substrate, the solution was spin coated on the substrates at different speeds.

2.3.3 Growth of gold Tips on CdSe rods

14 mg gold(III)chloride ($AuCl_3$), 40 mg dodecylamine (DDA), and 70 mg didodecyldimethylammoniumbromide (DDAB) are dissolved in 9 ml toluene in a vial inside the glove box. The mixture is set in the ultrasound, until the color changes from red to yellow.

Inside the glove box, a diluted solution of CdSe rods[3] is put on a magnetic stirrer and the yellow gold solution is added drop wise. Within 30 minutes the color of the CdSe rod solution changes from red over dark red to black, indicating the successful growth of the gold tips.

For purification the CdSe-Au dumbbells are precipitated with methanol and after centrifugation again dissolved in toluene.

2.3.4 PEG Passivation

All flasks were cleaned in hot Piranha, intensively rinsed with Millipore water and put in the ultrasound for three minutes prior to use.

Toluene p.a. was tried over a 3 Å molecular sieve and stored under nitrogen. Glass and silicon substrates decorated with gold nanodots are activated for one minute in an oxygen plasma at a pressure of 0,4 mbar at 150 Watt. The substrates are then transferred into a nitrogen filled flask and filled with 10 ml dried toluene. A small amount of PEG[4] is added to the toluene under nitrogen,

[2] TePla 100E microwave plasma system; isotropic chemical etching with a gas pressure of 0,4 mBar and a power of 150 W for 45 minutes

[3] CdSe rods were kindly provided by Dr. L. Carbone and A. Fiore from the group of Dr. L. Manna, NNL, Lecce, Italy.

[4] Trimethoxysilane modified PEG was kindly provided by F. Belz and T. Schoen from the group of Prof. J. P. Spatz, MPI for metals research, Stuttgart, Germany.

as well as a drop of triethylamine. The flask is then heated to 80 °C. After 24 hours the substrates are intensively rinsed with ethyl acetate and methanol and dried in a steam of nitrogen.

2.3.5 Thiol Functionalization

1,6-hexanedithiol was diluted in the 10^5-fold volume of toluene inside a glove box. The functionalization itself was carried out outside the glove box. The PEG passivated glass or silicon substrates were put into a glass petridish and covered with the dithiol solution. After three hours of incubation at room temperature the substrates were rinsed several times with toluene over 24 hours.

For the functionalization with biphenyl-6,6′-dithiol a stock solution in toluene was diluted to a concentration of 200 μM. In a glass petridish the freshly passivated substrates were covered with this solution and allowed to incubate for three hours at room temperature. The surfaces were then intensively rinsed with toluene over 24 hours.

2.3.6 Immobilization of the NCs

The immobilization of the NCs was done immediately after the functionalization. The wet thiolated surfaces were not allowed to become dry between the functionalization steps.

$CoPt_3$-Au Heterodimers and CdSe-Au Dumbbells The CdSe-Au dumbbells[5] are stored in the glove box under nitrogen, while the non air sensitive $CoPt_3$-Au heterodimers[6] are kept outside. Prior to the attachment both solutions, containing the NCs, are diluted to a low micromolar concentration. After diluting the CdSe-Au dumbbells are brought out of the glove box. The dithiol-functionalized surfaces are covered with the solution of the NCs. They incubated inside a petri dish at room temperature on a rocking platform. After three hours each substrate was rinsed three times with toluene and methanol. They were dried under a flow of of nitrogen prior to analysis.

Co-Au Matchsticks As the Co-Au matchsticks[7] are extremely air sensitive, the attachment was done inside the glove box . Few microliters of the concentrated black stock solution of Co-Au matchsticks were added to five milliliters of toluene. The passivated and thiol functionalized silicon substrates are transferred inside the glove box and covered with the particle solution inside a flask. After five hours of incubation the surfaces are rinsed three times with

[5] CdSe-Au dumbbells were kindly provided by A. Salant from the group of Prof. U. Banin, HUJ, Jerusalem, Israel

[6] $CoPt_3$-Au heterodimers were kindly provided by A. Fiore and A. Quarta from the group of Dr. L. Manna, NNL, Lecce, Italy.

[7] Co-Au matchsticks were kindly provided by Dr. K. Soulantica, INSA, Toulouse, France

toluene and methanol and tried in the nitrogen atmosphere in the glove box before their analysis.

To align the rods in a magnetic field, a drop of the particle solution was allowed to incubate for five hours inside the glove box. After establishing a magnetic field with an electromagnet on the substrate, the solvent was allowed to evaporate. Magnetic fields between 0,111 T and 1,11 T have been applied. To prevent the Co-Au matchsticks from aggregation during the magnetization they have been stabilized by adding extra hexadecyl amine (HDA) and applying a short ultrasound.

2.3.7 DNA as Linker

Surface Functionalization A 39 mer ssDNA strand with a thiol modification at the 5′ end was attached to the gold dots on a freshly PEG passivated surface. The used ssDNA had the following sequence:

5′-HS-aaa aaa aaa cgg gct cgc cac ttc ggg ctc atg agc gct-3′ (DNA-I),

with *a* being adenine, *c* presenting cytosine, *g* equals guanine and *t* is thymine.

The 9 adenine molecules towards the 5′ end work as spacer, so that the 30 other nucleotides are available for the hybridization of the ssDNA, attached to the nanoparticles. To prevent oxidation of the thiol groups with each other, a 10-fold molar excess of TCEP was added to the stock solution. The stock solution of single stranded DNA with a thiol group at the 5′ end (ssDNA-SH) was diluted to 1 μM with Tris-EDTA (TE)-buffer. PEG passivated glass substrates are functionalized with 30 μl of the ssDNA-SH solution in a petri dish.

The DNA solution was dropped on a piece of parafilm in a plastic petridish. The glass substrates were placed top down on the liquid. In a larger petridish a piece of paper was wetted with water; the petri dish with the substrate was put inside this petri dish and closed with parafilm. This helps to prevent the drying of the solution. After incubation for three hours the surfaces were rinsed with TE-buffer several times and put on a rocking platform over night. Prior to the attachment of the DNA functionalized NCs the surfaces were allowed to equilibrate in borate buffer for 20 minutes.

For absorption measurements, the ssDNA on the surface was stained with SYBR Green I. The stock solution was diluted in a ratio of 1:10000 with TE buffer. 60 μl of the diluted solution are put on top of a piece of parafilm inside a petridish. After 30 min incubation at room temperature the surface was thoroughly cleaned by rinsing several times with TE buffer. Before analyzing the substrates in the spectrometer, they were rinsed with Millipore water. Usually SYBR Green I is used for staining double stranded DNA. The absorption of the dye can here be detected at 520 nm. In contrast to other DNA stainings, it also binds to single stranded DNA. The absorption is here shifted towards longer wavelength.

CdSe-Au Dumbbells CdSe-Au dumbbells are brought into aqueous solution with mercaptoundecanoic acid (MUA). The NCs were precipitated with cold methanol (extra dry) and put inside the centrifuge for five minutes at 10000 rounds per minute (rpm). The precipitate was diluted in three milliliters of chloroform (extra dry). MUA was diluted in chloroform in a 10000-fold excess compared to the concentration of the NCs solution. Three milliliters of the MUA solution were mixed with the NCs solution. After mixing over night at 4 °C, two milliliters of borate buffer and 500 μl ssDNA-SH in a concentration of 10 μM were put on top and the pH was adapted to nine with a NaOH (pH10) solution. After shaking over night at 4 °C the particles are transferred into the buffer. The buffer solution was cleaned first in a NAP 25 and after in a NAP 10 column. The used ssDNA was functionalized with a thiol group at the 5′ end and had the following sequence:

5′-HS-aaa aaa aaa agc gct cat gag ccc gaa gtg gcg agc ccg-3′ (DNA-II)

The sequence of the DNA-II strand is comlementary to the DNA-I, except for the 9 adenine nucleotides at the 5′ end. For the functionalization of the polymer-coated nanoparticles, amino modified ssDNA was coupled to polymer coated nanoparticles over EDC/NHS chemistry. The solution of polymer coated nanoparticles was diluted in 5 ml PBS until the solution was only slightly red. The concentration is now at around 1 μM. A 1 mM concentration of EDC in PBS was added until a final concentration of 10 μM in the reaction solution was reached. A 100 mM Sulfo-NHS solution was added, until the concentration in the reaction solution was 5 mM. 1 ml of a 50 μM amino modified ssDNA was added. For a good mixing, the solution was se on a vortexer for two hours. Excess of EDC and NHS are removed by size exclusion chromatography in a 50 kDa cut-off column. The used ssDNA (DNA-III) has the same sequence as the DNA-II, but with an amino modification at the 5′ end.

5′-H_2N-aaa aaa aaa agc gct cat gag ccc gaa gtg gcg agc ccg-3′ (DNA-III)

For absorption spectrum measurements single stranded DNA with a Cy3 modification (DNA-IV) was allowed to hybridize with the ssDNA modified NCs. The sequence is the same as the DNA-I, but with the Cy3 modification at the 5′ end instead of the thiol group with the 9-a spacer:

5′-Cy3 cgg gct cgc cac ttc ggg ctc atg agc gct-3′ (DNA-IV)

100 μl of DNA modified NCs are mixed with 100 μl of a 100 μM solution of Cy3 modified DNA. After incubation for 5 hours at room temperature, the solution was cleaned in a 50 kDa cut off column until the washing solution did not show any absorption in the Cy3 range anymore.

Hybridization The ssDNA-SH modified NCs were heated to 70 °C, which is about 5 degrees less than the melting temperature of the used DNA. Also the substrates in the borate buffer were heated to 70 °C. 40 μl of the warm NCs solution were put inside a Petri dish with Parafilm and the warm surfaces were put on top. The DNA was allowed to hybridize for four hours at room temperature. The so functionalized substrates were intensively rinsed with

borate buffer and put on a rocking platform over night.

Directly before SEM analysis the substrates were rinsed with Milli pore water and dried under a flux of nitrogen.

Connecting Gold Dots via ssDNA To connect two gold dots on a passivated glass slide with ssDNA a strand out of 178 nucleotides (nt) containing a SH-group at the 5′ end[8] was hybridized with a 25 mer ssDNA, also modified with a SH group at the 5′ end. The 178 mer ssDNA had the following sequence:

5′-HS-cgg gct cgc cac ttc ggg ctc atg agc gct tgt ttc ggc gtg ggt atg gtg gca ggc ccc gtg gcc ggg gga ctg ttg ggc gcc atc tcc ttg cat gca cca ttc ctt gcg gcg gcg gtg ctc aac ggc ctc aac cta cta ctg ggc tgc ttc cta atg cag gag tcg cat aag gga g-3′ (DNA-V).

Accordingly the short ssDNA had the following sequence:

5′-HS-c ccc ccc tcc ctt atg cga ctc ctg cat tag-3′ (DNA-VI)

The 6 cytosines at the 5′ end work as spacer. The two DNA strands have an overlap of 25 nucleotides, leading to a stable connection between the two strands.

The ssDNA was stored at -21 °C. Before the hybridization the long DNA strand was heated to 90 °C to break possibly formed intramolecular hydrogen bonds. The two DNA strands were mixed in a 1:1 ratio and incubated for three hours. The resulting DNA strand contains now a thiol functionalization at both ends. To prevent the reaction of the free thiol groups with each other, TCEP was added to the reaction solution in 10-fold molar excess.

This bi-functionalized DNA was now attached to the surface. 30 μl of a 100 μM solution was put on a piece of parafilm inside a petridish, which was then put inside a lager one, containing a wet paper. After three hours of incubation at room temperature, the surfaces are thoroughly rinsed with TE buffer. They are stored in TE buffer; also the AFM analysis was performed in the buffer.

For fluorescence measurements the DNA was stained with SYBR Green I, according to the above mentioned protocol.

2.3.8 Micellar Nanolithography

In a glass vial 20 mg of the diblock copolymer PS 2076-*b*-P2VP 571 were diluted in 10 ml of dried toluene in the glove box. The solution was stirred over night to form uniform micelles. Alternatively 60 mg of PS 501-*b*-P2VP 223 were diluted in 12 ml of dried toluene in the glove box. Also this solution was stirred for 24 hours to ensure the formation of homogenous micelles.

Spherical CdSe quantum dots[9] in toluene were precipitated with mercap-

[8] The 178mer ssDNA (DNA-V) was kindly provided by Dr. N. Steinmetz from the group of Dr. D. Evans, JIC, Norwich, UK.

[9] Spherical CdSe particles were kindly provided by Dr. S. Kudera from the Department of Prof.

toethanol and mercaptopropionic acid. After centrifugation they are rinsed twice with toluene. The supernatant was poured away. The precipitate was put together with the micellar solution and stirred over night. The now hydrophilic quantum dots bind to the vinylpyridine in the core of the micelles.

Glass substrates and silicon wafers are cleaned in hot Piranha for at least 30 minutes. The surfaces are then rinsed with Millipore water, cleaned in the ultrasound and rinsed again with Millipore water. Before dip coating the substrates inside the micellar solution with the CdSe crystals they are dried in a flow of nitrogen.

2.3.9 Synthesis of $Bi[N(SiMe_3)_2]_3$

For the synthesis of the tris [bis (trimethylsilyl)amino] bismuth complex $Bi[N(SiMe_3)_2]_3$ we used a method described by *Carmalt* et al. [191].

1 ml (4,7 mmol) hexamethyl disilazane ($NH(SiMe_3)_2$) is filled into a 100 ml 3-neck flask inside the glove box. The flask is attached to a vacuum line and cooled to 0 °C with an external ice bath. Under stirring 3,0 ml (4,7 mmol) of a 1,6 M n-buthyl lithium (n-BuLi) solution in hexane is added drop wise. After stirring for one hour at 0 °C, the solution is allowed to warm and heated in a water bath to remove excess of solvents in the vacuum. A white precipitate ($Li[N(SiMe_3)_2]$) keeps in the flask, which is dissolved in 10 ml diethyl ether. The flask is again cooled down to 0 °C. 500 mg (1,6 mmol) bismuth(III)chloride ($BiCl_3$) are dissolved in a mixture of 10 ml diethyl ether and 2,5 ml tetrahydrofurane (THF). The solution is slowly added to into the flask under continuous stirring. The solution changes its color from white to yellow. After one hour of stirring the solution is allowed to warm up to room temperature. All volatiles are then removed by vacuum. The precipitate is dissolved in 15 ml of pentane and filtered through a medium-porosity (P4) glass frit, resulting in a yellow, oil like solution. Drying in the vacuum leaves a yellow solid which is used for further synthesis without further purification. The product is stored in the glove box, as $Bi[N(SiMe_3)_2]_3$ is an air sensitive complex.

2.3.10 Au@Bi Core-Shell Particles

We used two different approaches for the growth of the core-shell particles. The growth of particles on nanopatterned substrates has been successfully demonstrated for other metals [64]. According to the there described method, we are comparing two different ways of growing a shell around the gold dots on the surface. In a first approach, the dip-coated silicon substrates are activated in an oxygen plasma for three minutes at 150 W and an oxygen pressure of 0,4 mbar. This short plasma treatment reduces the gold salt to elementary gold, by leaving the diblock copolymer on the surface. By adding a gold salt and a reducing agent it is possible to enlarge the gold particles on the surface

J. P. Spatz, MPI for metals research, Stuttgart, Germany.

from 12 to 40 nm. This intramicellar approach ensures that the hexagonal pattern is not destroyed. In a second approach, we use silicon substrates, where the polymer has been completely removed. As the gold dots can sink inside the silicon oxide layer of the substrate, an additional passivation layer is here not necessary.

The growth itself has been carried out in the same way on the two different substrates. 1,3-diisopropylbenzene and poly-(1-vinylpyrrolidone)-graft-(1-hexadecane) are mixed in a 3:1 weight ratio and stored over a 3 Å molecular sieve in the glove box as stock for all reactions. 114 mg of the synthesized $Bi[N(SiMe_3)_2]_3$ complex, 76 mg sodium(bistrimethylsilyl) amide ($Na[N(SiMe_3)_2]$, 0,6 M solution in toluene) and 16 g of the mixture out of 1,3-diisopropylbenzene and poly-(1-vinylpyrrolidone)-*graft*-(1-hexadecane) are mixed in a multi neck flask (figure 18). This flask ensures that each surface is treated equally inside the solution and it makes it possible to control the reaction time of the individual substrates, without interrupting the vacuum or the nitrogen atmosphere. The yellow solution is heated to 170 °C under nitrogen (temperature measured outside the flask). The solution changes its color from pale yellow to orange-brown.

Through each neck one gold nanopatterned silicon substrate is put inside the reaction solution. After different reaction times the substrates are rinsed with 1,3-diisopropylbenzene and directly used for the growth of the CdSe wires. For SEM analysis the samples were additionally rinsed with methanol and tried under a flux of nitrogen.

2.3.11 Solution-Liquid-Solid Growth of CdSe Rods and Wires

The freshly prepared substrates with the Au@Bi nano patterning are directly used for the growth of the CdSe wires.

5 g tri-*n*-octylphosphine oxide (TOPO) and 69 mg Cd stearate are mixed in a multi neck flask (figure 18) under nitrogen atmosphere and heated to 120 °C. After reaching 100 °C, a vacuum is applied for about 30 minutes. Then the mixture is heated to 240 °C under a nitrogen atmosphere. Selenium and TOP are mixed in a weight ratio of 1:10. Through each neck one substrate is put inside the solution. One neck is kept free, through which 400 mg of TOP and 400 mg of selenium (Se:TOP) are syringed inside the flask. After different reaction times the substrates are rinsed with isopropanol and toluene and put in a petri dish with isopropanol on a rocking platform over night. After rinsing with methanol and drying with nitrogen they are analyzed in the SEM and with XPS.

2.3.12 Solution-Liquid-Solid Growth of Co Rods

Anisole was tried over a 3Å molecular sieve and stored under argon. All working steps, besides the heating, have been carried out inside a glove box, with argon as working gas.

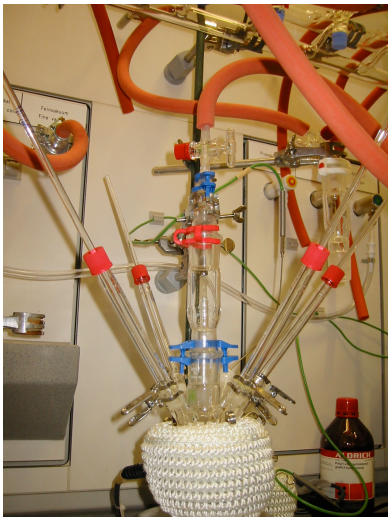

Figure 18: **Multi-neck flask for the SLS growth of CdSe wires on substrates.** Through each neck a gold nanopatterned Si substrate can be introduced.

200 mg $Co[N(SiMe_3)_2]_2$ (0,5 mmol), 120 mg hexadecylamine (HDA, 0,5 mmol), and 100 mg lauric acid (LA, 0,5 mmol) are each dissolved in 1 ml of dried anisole. The HDA and the LA solution are mixed with each other, resulting in a white gel. Adding the green Co solution results in a dark blue solution, which was filled up to 10 ml with anisole. This stock solution was then used for the reactions. The molar ratio between the three components was always kept constant. But changes have been done in the final concentration of the cobalt precursor, the temperature and the reaction time. A silicon surface, nanostructured with platinum dots, was put inside a Fisher-Porter bottle and covered with the stock solution. The so prepared bottle was attached to a Schlenk line. The tubes are evacuated thoroughly and filled with argon. After applying a short vacuum to the Fisher-Porter bottle, it was filled with hydrogen up to a pressure of 3 bars. The bottle is then put in a pre-heated oil bath at 100 °C for 26 hours.

After the reaction was finished, the bottle was transferred back inside the glove box, where the substrate was rinsed with anisole, a solution of HDA in toluene, toluene and methanol. After letting them dry inside the glove box, the substrates are analyzed in the SEM.

2.3.13 Modification of Streptavidin with Traut's Reagent

2-iminothiolane (Traut's Reagent) was dissolved in PBS (pH 8,0). For the thiolation reaction Traut's reagent was added to 150 μl of a streptavidin (SAv) solution (c = 1mg/ml). To test the necessary amount, a 10-fold and a 100-fold excess of the iminothiolane solution was added. After 12 h incubation at 4 °C, the protein was cleaned with size exclusion chromatography (cut-off column

with cut at 30 kDa). The number of introduced thiol groups was determined with a Thiol Determination Kit from Pierce. The same method was used for the modification of Alexa Fluor 488 modified SAv. A 10-fold excess of Traut's reagent was added to a 1 mg/ml solution of the protein. After incubation at 4 °C for 12 hours, the SAv was cleaned in a 30 kDa size exclusion column.

2.3.14 Layers of Viral Nanoparticles

The experiments in the QCM-D are performed under a flow of 20 μl/min. Vesicles, doped with biotin, are added on a silicon oxide surface in a concentration of 50 μg/ml in a buffer (10 mM HEPES, 150 mM NaCl, 2 mM EDTA, 3 mM NaN_3, pH 7,4) upon saturation. A 1 mg/ml stock solution of streptavidin was diluted 1:100 in PBS. The resulting 10 μg/ml solution was added in the flow on the bilayer. The modified CPMV stock solutions are diluted 1:10 in PBS. The resulting solution (c = 10 μg/ml) is added on top of the SAv layer. The steps are repeated until three SAv layers have been added. Each solution reacted with the surface until saturation. Between each step the surface was intensively rinsed with PBS.

The same protocol was used for the modified SAv. The concentration of the protein was 20 μg/ml, the concentration of the CPMV was the same, as well as the flow speed. To attach the HS-SAv to the gold surface, a 20 μg/ml solution was incubated on the surface upon saturation. The biotin modified CPMV was added in a concentration of 10 μg/ml. After saturation was reached, the surface was intensively rinsed with PBS.

Part III
Results and Discussion

3 Metallic Nanoparticle Arrays

The synthesis of nanoparticles out of a broad variety of materials is in the interest of research since long time [192]. Also alloys and oxides can be produced [193]. The limit in possible application is the ordered arrangement of these nanoparticles on a surface.

One well studied method is the block copolymer micellar nanolithography, which enables the synthesis of well ordered nanostructures over large areas, where the interparticle distance as well as the size of the distance can be controlled by the experimental parameters. [83] So far, interparticle distances of 28 nm up to 250 nm [62, 63] have been realized. The particle size ranges between 3 and 30 nm [64]. After the preparation of the monomicellar film on a glass substrate the hexagonal arrangement can be imaged in the SEM (figure 19A, B, C, D).

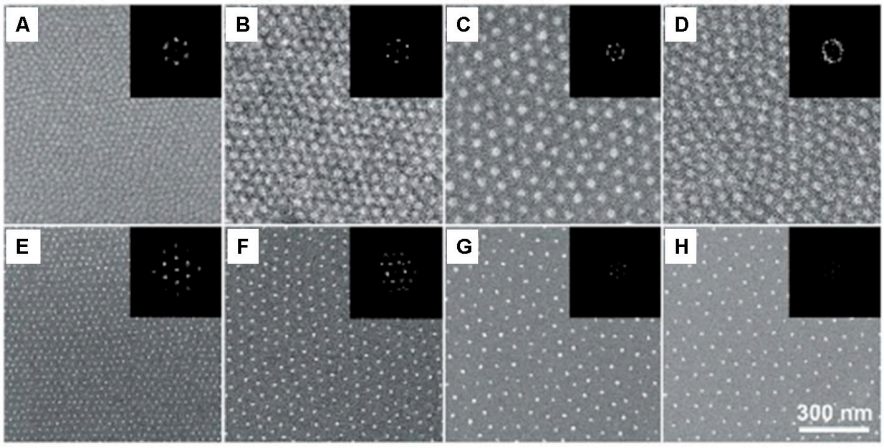

Figure 19: **SEM micrographs of the micellar film of different polymers.** The inset is showing FT images. A: PS 190-*b*-P2VP$[HAuCl_4]_{0,2}$ 190; B: PS 500-*b*-P2VP$[HAuCl_4]_{0,5}$ 270; C: PS 990-*b*-P2VP$[HAuCl_4]_{0,2}$ 385; D: PS 1350-*b*-P2VP$[HAuCl4]_{0,2}$ 400; E, F, G, and H showing the corresponding gold pattern after plasma treatment; from [62].

The micelles assemble in a quasi-hexagonal packing on the flat surface. The vinylpyridine core, containing the metal salt, appears as round little disks (figure 19A, B, C, D). Subsequent hydrogen plasma treatment reduces the metal precursor to elementary gold and burns the organic shell. The pattern of the gold dots reflects the array of the micellar layer (figure 19E, F, G, H) [62].

The interparticle distance is dependent on the molecular weight of the polymer, the dipping velocity and the polymer concentration. The influence of these parameters will be discussed later in this chapter.

The formation of the elementary metal out of the precursor as well as the burning of the polymer can be followed by XPS measurements. As the polymer contains a lot of carbon, the signal should be very intense for the micellar

layer and should decrease during the plasma process. Also the formation of the elementary gold should be visible, as the ions and the element have different electron binding energies [83]. The results are exemplarily shown for the PS 2076-*b*-P2VP 571 polymer. All other polymer showed the same characteristics (figure 20)

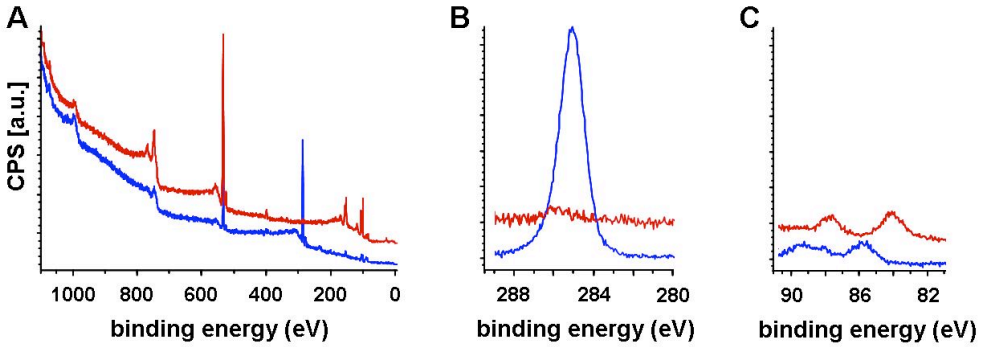

Figure 20: **XP spectra of a surface dip coated in the PS 2076-*b*-P2VP 571 polymer solution before (blue line) and after hydrogen plasma treatment (red line);** shown are the survey (A), the C-1s signal (B) and the Au-4f signal (C); in the survey an increase of the signal for SiO_2 can be observed due to the plasma process; the carbon signal nearly vanishes during the plasma, while in the Au-4f signal a shift of both peaks can be observed

.

In the survey the increase of the Si-2p signal at 99,3 eV can clearly be seen. The signal at 104,1 eV refers to siliconoxide. The increase of both peaks is due to the removal of the polymer layer, shielding the electrons from the surface. But not only the intensity is changing, but also the relative intensity of the peaks to each other. After the plasma treatment, the SiO2 peak is becoming more prominent. Obviously the oxide layer of the silicon substrate is growing in the plasma process. This might be due to impurities in the plasma process as the initial vacuum is only controlled down to 10^{-2} mbar. The signal for C-1s at 285,5 eV originates from the diblock copolymer. As the surface is completely covered with it after the dip coating, the signal is very prominent before the plasma treatment (figure 20B, blue line). After the plasma treatment (figure 20B, red line) the signal is nearly vanished. Carbon impurities from the air (e.g. CO_2) will always occur, as the substrates are extremely reactive directly after the etching process.

In figure 20C the reduction of gold ions into elementary gold is shown. For gold one can usually detect a $4f_{7/2}$ peak at 84,0 eV, and a $4f_{5/2}$ peak in a distance of 3,7 eV [187]. Both peaks are visible in the spectrum after the plasma treatment (figure 20C, red line). Directly after the deposition of the micelles the peaks are shifted of about 2 eV (figure 20C, blue line), indicating that gold ions are present on the surface. The shift of the Au-4f signals is already observed

after few minutes of plasma treatment, as the reduction of the metal is faster than the complete removal of the polymer film from the substrate [64].

Even thought the reduction of the metal salt is finished after few minutes in the plasma, the final formation of the gold cluster needs the complete plasma procedure. Interrupting the plasma process, result in an increased diameter of the particles (see chapter 5.1.1).

In TEM cross-section [63] it was shown that the dots on the surface have spherical shape. So it is possible to obtain the diameter of the gold nanodots via AFM analysis (figure 21).

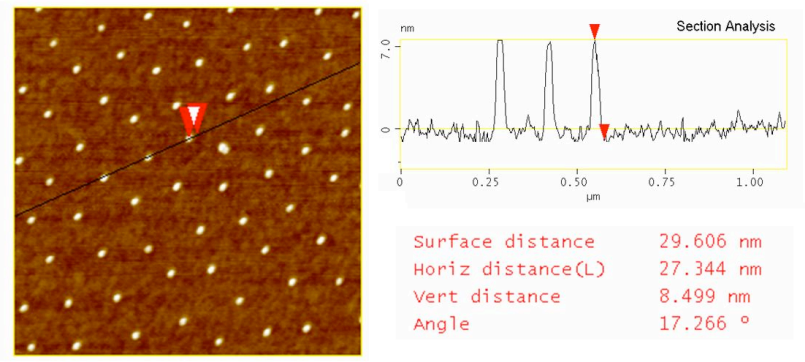

Figure 21: **AFM image of a nanopatterned gold dot surface obtained by working with PS 2076-*b*-P2VP 571.** Cross section analysis (black line in the image) gives a height of the marked gold dot (red arrows) of 8,5 nm; the scan size is 1 μm.

In the AFM the height of the gold dots can be determined by a section analysis. The gold dots have a sharp height profile. In this case, the loading of the micelles was set to L = 0,3, resulting in a height and thus a diameter of the particles of 8,5 nm. The size of the gold dots is dependent on the amount of metal precursor added to the micellar solution, as well as the molecular weight of the polymer.

It is also possible to create nano-pattern of other metals than gold with the help of the block copolymer nanolithography. Working with hexachloroplatinum acid results in nanopattern with platinum dots, where the interparticle spacing as well as the size is equivalent to the ones obtained with gold.

3.1 Influence of Polar Solvents

Since goldchloride, used as metal precursor, is extremely hygroscopic, water is also getting inside the polymer solution, influencing the order and the interparticle distance. To analyse the influence of water on the quality of the nanopatterned substrate, defined amounts of water were added to the polymer solution, with dried toluene as solvent. In SEM analysis we studied how

already small amounts of water, added to the micellar solution of PS 501-*b*-P2VP 235, PS 1056-*b*-P2VP 495, and PS 2076-*b*-P2VP 571, can influence the resulting nanopattern on the surface (figure 22).

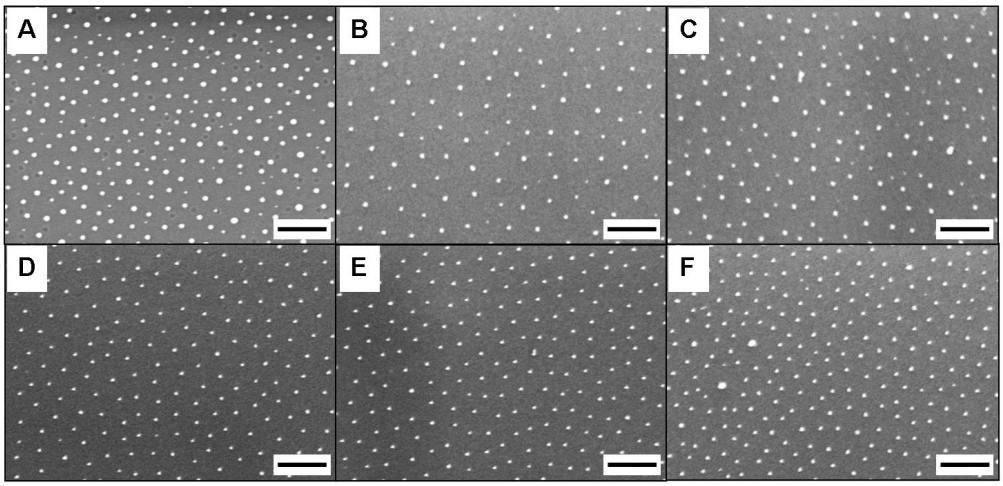

Figure 22: **SEM images showing the influence of water to the order of the nano patterned surface created with the PS 2076-*b*-P2VP 571 polymer.** Different amounts of water (A 0 μl, B 0,5 μl, C 1 μl, D 2 μl, E 5 μl, F toluene saturated with water) result in a different orders of the surface and homogeneous or inhomogeneous size distribution of the gold pattern on the surface. The scale bars correspond to 200nm.

Working with completely dry toluene results in gold dots with inhomogeneous size (figure 22A). Also the hexagonal order is disturbed, which is reflected in the value of the order parameter (ψ = 0,41). The interparticle distance was measured to 107$\pm$20nm. Adding 0,5 μl of water induces an improvement of the whole pattern. The order parameter rises to ψ = 0,60, the lateral also rises 121$\pm$13nm (figure 22B). In strong contrast is the result, after addition of 1 μl of water to the polymer solution (figure 22C). The order parameter drops to ψ = 0,39 and the interparticle distance was determined to 119$\pm$30 nm. However, adding a total amount of 2 μl of water improves the pattern again. On the resulting surface the gold particles have a lateral distance of 112$\pm$13 nm with an order parameter of ψ = 0,51 (figure 22D). Additional water slightly increases the value of the order parameter to ψ = 0,51 for 5μl (figure 22E) and ψ = 0,52 for the water saturated toluene (figure 22F), but the size of the dots becomes inhomogeneous again. The resulting interparticle distance was determined to 115$\pm$14 nm and 107$\pm$18 nm. Large gold dots can be found, where the surrounding is not hexagonally arranged any more. Gold particles with a diameter of up to 25 nm have been determined on the substrate with absence of water, 5 μl water and a saturation of water. The average diameter is 18$\pm$7 nm. For the other substrates the average diameter is 12$\pm$4 nm[10]. The water re-

[10]The diameter of the gold particles was quantified by MatLab (The MathWorks Company,

acts with the gold precursor in the hydrophilic core of the micelle. A complete absence of water leads to a irregular pattern. A homogenous formation of the micelles in solution is not possible. Already small amounts of water stabilize the micellar system. They are more homogenous in size and also the metal precursor is homogeneously distributed, resulting in a regular diameter of the final gold dots and a regular hexagonal pattern. The interparticle distance is only varying in the range of the errors. There is no essential effect of the water. Only the values after adding 1 μl water to 10 ml toluene do not fit in this results. It can can not be explained by a destabilization of the micelles, as higher amounts of water improve the pattern again.

To see if this effect is specific for water or can be induced by any polar solvent, we performed the same experiments with a ethanol, a solvent, which is better mixable with toluene, but still polar. In SEM analysis the resulting effect on the quality of the pattern was controlled (figure 23).

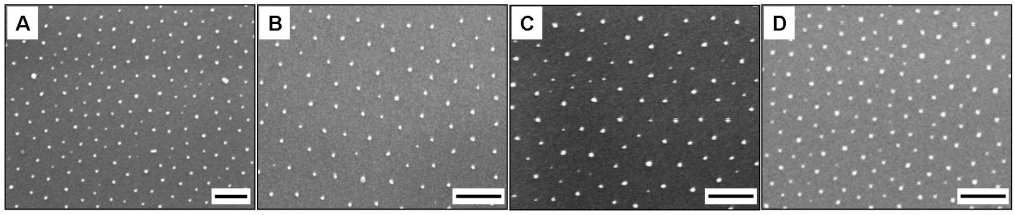

Figure 23: **Influence of Ethanol on nanostructured surfaces: SEM images of gold dot surfaces generated by working with PS 2076-*b*-P2VP diblock copolymer after addition of defined amounts of ethanol per 10 ml of toluene.** A: 0,5 μl of ethanol added; B: 1 μl; C. 2 μl; D: 5 μl. The scale bars correspond to 200 nm.

Adding 0,5 μl ethanol to 10 ml of the polymer solution results in an interparticle spacing of 113$\pm$22 nm, while the order parameter ψ is 0,51 (figure 23A). Addition of 1 μl ethanol results in an increase of the order parameter ψ to a value of 0,67. The interparticle distance was measured to be 112$\pm$15 nm. The value of the order parameter is high compared to the substrates before, meaning a highly ordered surface. In contrast is the diameter of the gold particles. The diameter is extremely inhomogeneous ($14\pm7nm$). Increase in the concentration of ethanol leads to a decrease of the order parameter ψ down to 0,45 (interparticle distance: 107$\pm$20 nm), which is further reduced to ψ = 0,36 (interparticle distance: 121$\pm$35 nm) if 5 μl ethanol were added.

The ethanol interacts with the core of the micelles, comparable to water, influencing strongly the order parameter and slightly the lateral distance.

Addition of 0,5 μl of ethanol or water to 10 ml dried toluene result both in an improvement of the hexagonal pattern. The initial order parameter of ψ = 0,41 is improved in both cases. The further addition of water or ethanol results in completely different reactions of the system. Adding water leads to a

Aachen, Germany) analysis of the SEM images, kindly programmed by H. Boehm from the group of Prof. J. P. Spatz, MPI for metals research, Stuttgart, Germany.

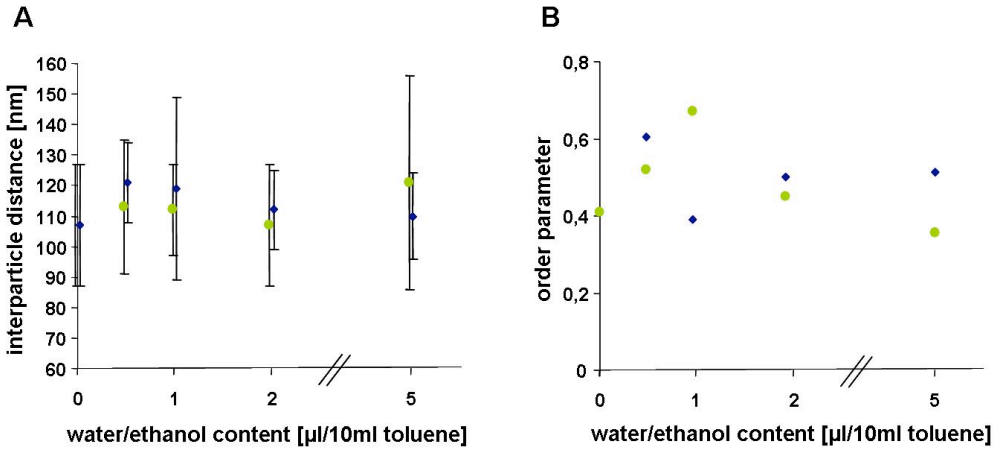

Figure 24: **Comparison of the influence of water and ethanol on the lateral distance and the order parameter of a PS 2076-*b*-P2VP solution.** A: The influence on the lateral distance is in the range of the errors. B: The order parameter is strongly influenced by the addition of both solvents. Blue squares: water; green circles: ethanol.

worsening of the pattern, while the ethanol improves the order. Adding more than 1 μl water to 10 ml toluene improves the pattern, but the diameter of the gold dots becomes polydispers. In contrast, the addition of ethanol disturbs the hexagonal pattern, leading to an order parameter of only 0,35.

Addition of controlled amounts of water results in a more controlled manufacturing of the polymer solutions. The addition of 2 up to 5 μl of water per 10 ml of dried toluene lead to hexagonal pattern, with uniform diameter of the gold dots and a good hexagonal pattern.

Addition of water stabilizes the micelles, leading to a homogeneous size distribution of the gold particles and a well ordered pattern. Ethanol is also able to stabilize the core of the micelles but the interaction is not as strong as with the water. Regarding ethanol, there is a certain threshold. Exceeding this limit induces a swelling of the micelles, especially the cores. The gold precursor is no more tightly attached inside the micelle and can diffuse, leading to a brought size distribution in the diameter of the gold dots. Only the effect of a degradation after addition of 1 μl of water can not be explained with this effect.

3.2 Tuning the Interparticle Distance

The interparticle distance as well as the particle size can be controlled independently from each other. Three parameters can be varied to tune the interparticle distance: (i) the molecular weight of the polymer, (ii) the concentration of the micellar solution and (iii) the retraction velocity of the substrate out of the solution.

3.2.1 Molecular Weight of the Diblock Copolymer

The use of block-copolymers with different molecular weight is probably the most evident possibility to change the interparticle spacing, as the diameter of a micelle is bigger with an increasing chain length and thus a higher molecular weight. The diameter of a dry micelle can be estimated according to the following equation:

$$M_{micelle} = \frac{p \cdot M_W}{N_A} = \rho_{micelle} \cdot \frac{4}{3}\pi \cdot R^3 \tag{10}$$

where $M_{micelle}$ is the weight of a single micelle, ρ the number of polymer chains per micelle, M_W the molecular weight of the polymer and N_A the Avogadro constant [69]. According to equation 10 the radius R is in the third power proportional to the molecular weight of the diblock copolymer (eq. 11):

$$R^3 \propto M_W \tag{11}$$

If the micelle density, $\rho_{micelle}$, is equal to the bulk density of polymers ($PS = P2VP = 1,1 g/cm^3$), the size can roughly be calculated for a given number of polymer molecules per micelle [69].

An increase of the interparticle distance is observed in dependence of the polymer mass. Freshly cleaned glass slides are dipped into solutions of diblock copolymers with different molecular weight with a constant retraction speed of 12 mm/min. After subsequent hydrogen plasma the surfaces were characterized in the SEM (figure 25).

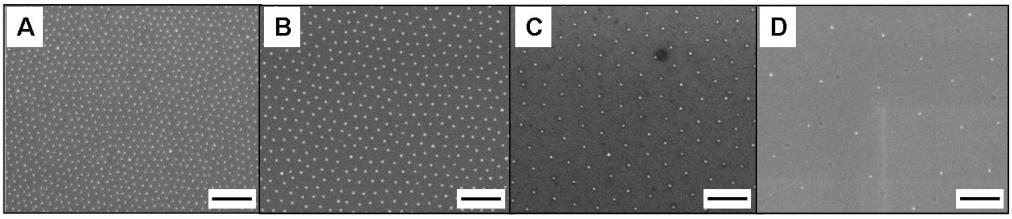

Figure 25: **SEM images of nanopatterned gold surfaces with different interparticle spacing coming from different molecular weights of the used polymers.** The particle spacing ranges from 38±6 nm for PS 245-*b*-P2VP 223(0,2) (A); over 60±8 nm for the PS 501-*b*-P2VP 235(0,5) polymer (B); and 112±14 nm for PS 2076-*b*-P2VP 571(0,5) (C); to 242±47 nm for the PS 5355-*b*-P2VP 714(0,2) polymer (D). The scale bars correspond to 200 nm.

By varying the molecular mass of the polymer it is possible to obtain different interparticle distances of the gold nanodots. The distances range from 38 nm for the PS 245-*b*-P2VP 223 polymer to 242 nm for the PS 5355-*b*-P2VP 714 polymer.

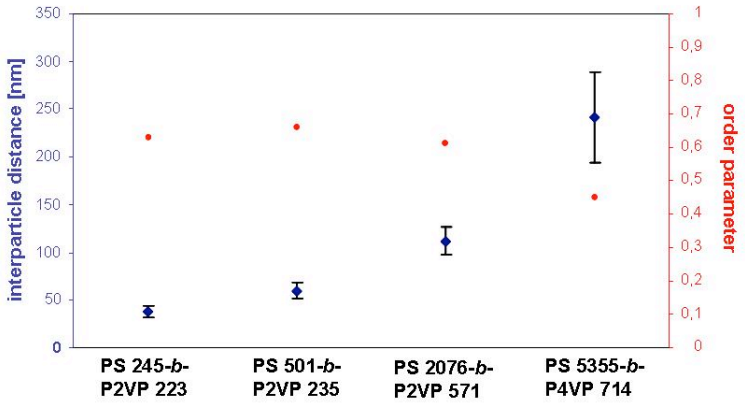

Figure 26: **Interparticle distance and order parameter in dependence of the diblock copolymer.** The smaller the diblock copolymer and thus the micelles are, the bettwe is the obtained order on the surface, which is due to the softness of the micelles.

With the PS 245-*b*-P2VP 223 polymer an interparticle distance of 38±6 nm and an order parameter ψ of 0,63 is obtained (figure 26). For the PS 501-*b*-P2VP 235 polymer the distance of the dots is calculated to 60±8 nm with ψ= 0,66. The PS 2076-*b*-P2VP 571 polymer gives also a well ordered surface with ψ= 0,61 and an interparticle spacing of 112±14 nm, while working with the PS 5355-*b*-P2VP 714 polymer leads to a distance of 242±47 nm and an order of the structure of ψ = 0,45. Especially for the PS 5355-*b*-P2VP 714 polymer the order parameter decreases. The very soft shell of the polymer surrounding the stiffer core can explain this. The softness is increasing with longer polymer chains, which then causes a less precise hexagonal deposition of the micelles for very long diblock copolymers.

The particle distance can theoretically be calculated using equation 10. The diameter of the micelles should be the same as the particle distance, within a certain error due to the polydispersity of the used diblock copolymers.

The spacing on the surfaces can vary from the calculated value, as the micelles do not behave as spherical particles. On the surface they spread as soon as they are in contact with the surface. This leads to a larger value than the theoretical one. This spreading behavior is dependent on the concentration of the polymer in the solution. So this is the second parameter how to control the nanopattern on the surface. By working with the same polymer it is thus possible to vary the interparticle spacing by changing the concentration of the polymer [95]. The advantage by working with the same diblock copolymer is that the size of the particles stays constant. A stock solution of a polymer can be diluted to lower concentrations, leading to substrates with different interparticle spacing but the same size of the gold dots.

Also the speed of retracting the substrates out of the solution influences the interparticle distance. Increasing withdrawal speed leads to smaller interpar-

ticle distances on the surface [95].

3.3 Influence of the Solvent and Vapor

The above-described effects can be explained by assuming different thicknesses in the micellar film, deposited on the surface. If the thickness of the adsorbed film is in the range of the diameter of the micelles, they assemble in a spherical shape. Is the height of the film less than the diameter of the micelles, they spread on the surface. This leads to an increase of the interparticle spacing. The thickness of a film on surfaces, obtained by dip coating, can be calculated to [194]

$$h_\infty = 0,946\sqrt{\frac{\sigma}{\rho \cdot g}} \cdot Ca^{2/3} \tag{12}$$

With Ca being the capillary number ($Ca = \mu U/\sigma$), the height depends on the withdrawal speed U, the liquid viscosity μ, the surface tension σ, and the density ρ

$$h_\infty = 0,946\frac{(\mu U)^{2/3}}{(\rho g)^{1/2} \cdot \sigma^{1/6}} \tag{13}$$

g denotes the standard gravity (9,81 m/s^2). This equation is only valid for capillary numbers $Ca << 1$, since the viscous contribution to the normal pressure is neglected in the derivation.

Besides the retraction speed U and the liquid viscosity μ, which is dependent from the concentration of the polymer dissolved in the solvent, also the surface tension σ plays an essential role in the film thickness. It is possible to compare the height of the solvent film, in dependence of the retraction velocity and the surface tension, by varying the solvents (figure 27). As xylene is also known to be a versatile solvent for block copolymer micellar nanolithography, we compared the resulting film of ortho xylene with the one from toluene[11] .

Calculated are the film thicknesses for toluene (μ = 0,60 mPa·s, σ = 28,4 N/m, ρ = 0,87 g/cm^3), and ortho xylene (μ = 0,81 mPa·s, σ = 30,1 N/m, ρ = 0,87 g/cm^3) (values from [195]). The two solvents lead to differences in the thickness of their films on the surface. Therefore also the lateral distance of the resulting gold pattern should be different. As changing the solvent leads to the variation of several parameters, we designed experiments, where only the surface tension is changing, keeping all other parameters (dipping geometry, temperature, etc.) constant. This can be realized by controlling the amount of vapor above the dipping solution. The amount of vapor above the corresponding solvent is known to influence the surface tension. Having low vapor above the surface, should lead to a decrease of the surface tension and to larger interparticle distances.

[11] Experiments from this chapter have been carried out in collaboration with H. Boehm from the

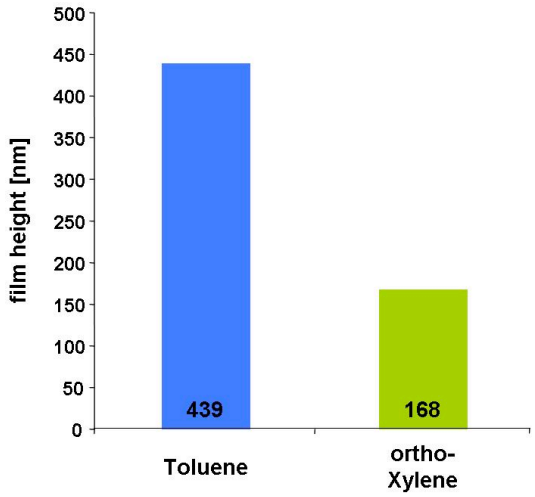

Figure 27: **Film thickness in dependence from the surface tension.** The surface tension is dependent on the solvent; blue: toluene; green: ortho xylene.

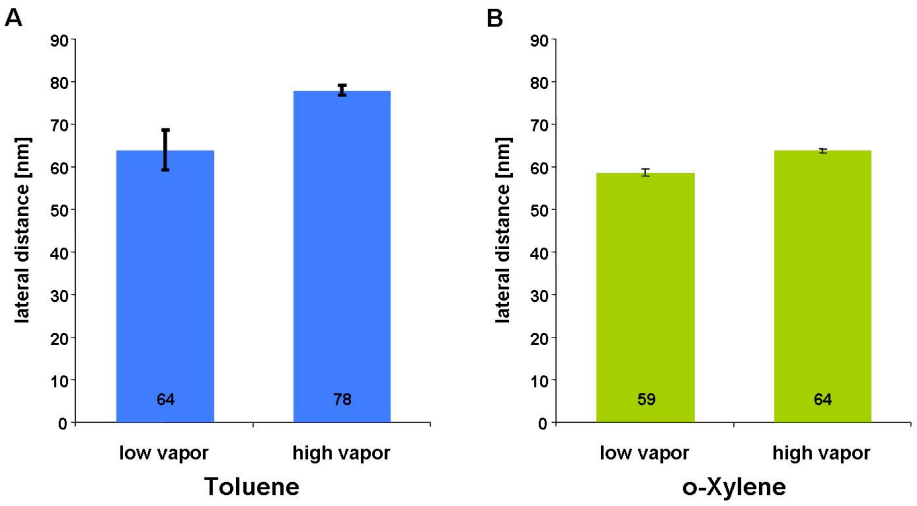

Figure 28: **Influence of the vapor and thus the surface tension on the interparticle distance, working with two different solvents and the PS 1056-*b*-P2VP 495 polymer in a concentration of 5 mg/ml.** A: A high amount of vapor above the dipping solution woth toluene as solvent leads to an increase of the interparticle distance. B: The same effect can be observed for working with ortho xylene (o-xylene) as solvent.

A gold nanodot pattern, obtained by dip coating a toluene solution of PS 1056-*b*-P2VP 495, is strongly influenced by the amount of vapor above the solution (figure 28A). An increase in the vapor and thus a decrease of the surface tension results in an increase of the interparticle distance from 64±9 nm to 78±2 nm. This is in accordance with the above made calculations, where a decrease of the surface tension results in a lower film thickness and thus in a larger interparticle spacing.

According to the above made calculations (equation 13, figure 27), working with xylene instead of toluene as solvent should increase the interparticle distance, as the film height is here less. Also the single isomers differ in their properties. A 5mg/ml PS 1056-*b*-P2VP 495 solution with ortho xylene as solvent results in an interparticle spacing of 58±1 nm Increasing the amount of vapor above the dipping solution results in an increase to 64±1 nm.

Both solvents show the expected results that a decrease in the surface tension results in an increase of the interparticle distance. Comparing the results, obtained with polymer solutions with toluene or xylene as solvent, with the calculations with the pure solvents, it becomes obvious that it is not possible to compare the values for working with toluene with the ones of o-xylene. The lateral distances of the xylene solution should be larger than the ones of the toluene solution, as the thickness of the xylene film is lower than the one from toluene. But o-xylene results in similar interparticle distances as toluene, in fact they are even smaller. Obviously there must be further parameters, influencing the lateral distance, besides the ones, regarded in equation 13.

A parameter, which is completely ignored, is the influence of the surface. In a micellar solution there is always equilibrium between free monomer chains and the micelles [81]. The process of assembly of the micelles happens in two steps. As the repulsion forces between the hydrophobic polystyrene shell and the hydrophobic surface are too high, the micelles cannot directly assemble on the surface. So in a first step a brush of the monomer chains from the solution is formed on the surface [67, 78]. The vinylpyridine can interact with the hydrophilic surface while the polystyrene is forming a brush. For the micelles it is now possible to bind to the surface, covered with the polystyrene brush. The formation of the brush is influenced by the polarity of the surface. The density of the monomers and thus the polystyrene brush can vary.

3.4 Spin Coating of Polymer Solutions on Structured Substrates

Zero-mode waveguides have been developed in order to improve the analysis of DNA strands. These nanostructured devices of fused silica and aluminum offer a new method for highly efficient single molecule analysis at high fluorophor concentrations [196].

Common optical approaches for studying single molecule events include fluorescence correlation spectroscopy (FCS) or total internal reflection fluo-

group of Prof. J. P. Spatz, MPI for metals research, Dept. Prof. Spatz, Stuttgart, Germany.

rescence microscopy (TIRF) [197, 198]. These approaches provide observation volumes on the order of 0,2 femtoliters requiring pico- or nanomolar concentrations of the fluorophor in order to isolate individual molecules in solution. To study enzymatic controlled events, higher concentrations are required, as lower ligand concentration can influence the mechanistic pathway of enzyme kinetics [196].

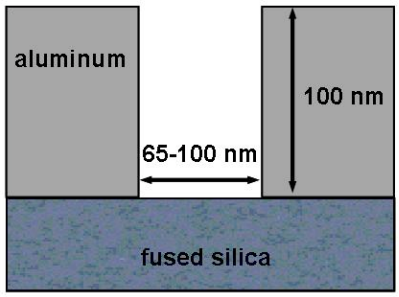

Figure 29: **Schematic of a zero mode waveguide (ZMW).** On top of the underlaying fused silica is a film of aluminum with a height of 100 nm. This film contains wells with an adjustable diameter between 65 and 100 nm.

Zero-mode waveguides (ZMWs, figure 29) consist of fused silica and a 100 nm thick layer of aluminum. The wells, obtained by lithography, have an adjustable diameter between 65 to 100 nm [199]. These structures offer the possibility for the analysis of single molecule events in high concentrations but still in a good signal to noise ratio. To immobilize single enzymes in the bottom of the well, an anchoring point is necessary. We functionalized the bottom of the wells with gold dots by spin coating a micellar solution of PS 245-*b*-P2VP 223 and of PS 2076-*b*-P2VP 571 at different spin speeds. To get the number of occupied wells and the number of gold dots per well the chips are imaged in the SEM and after analyzed by MatLab[12].

In the SEM one can easily distribute between wells with or without gold dots (figure 30). The wells appear as black circles, while the gold dots on the bottom can be seen as white dots. Besides the empty wells, we observed also wells with two up to six gold dots. The percentage of wells filled with one or more gold particles is dependent on three parameters: (i) the polymer solution, (ii) the speed of spin coating, and (iii) the diameter of the wells.

The diameter of the wells was ranging from 65 nm, over 80 nm to 100 nm. The spin-speed was set to 2000 rounds per minute (rpm) and 8500 rpm (figure 31). Between 150 and 300 wells have been analyzed for each parameter.

For the PS 245-*b*-P2VP 223 the percentage of wells, filled with one or more gold dots, was always larger than for the PS 2076-*b*-P2VP 571 polymer. This trend can be observed for both spin speeds. At a speed of 2000 rpm 71% of the wells with a diameter of 100 nm were occupied with at least one gold dot

[12]MatLab kindly programmed by H. Boehm from the group of Prof. J. P. Spatz, MPI for metals research, Stuttgart.

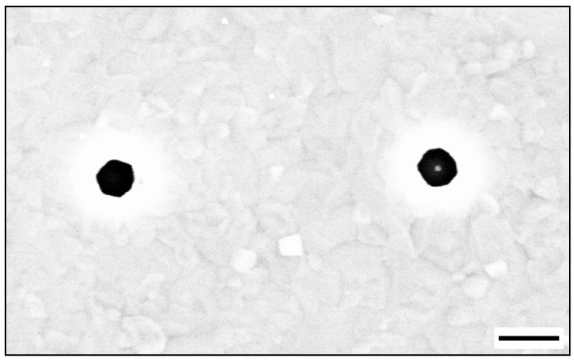

Figure 30: **SEM image of ZMW chip containing wells with a diameter of 100 nm.** One of them contains a gold dot (right), while the other one is empty (left). The scale bar corresponds to 200nm.

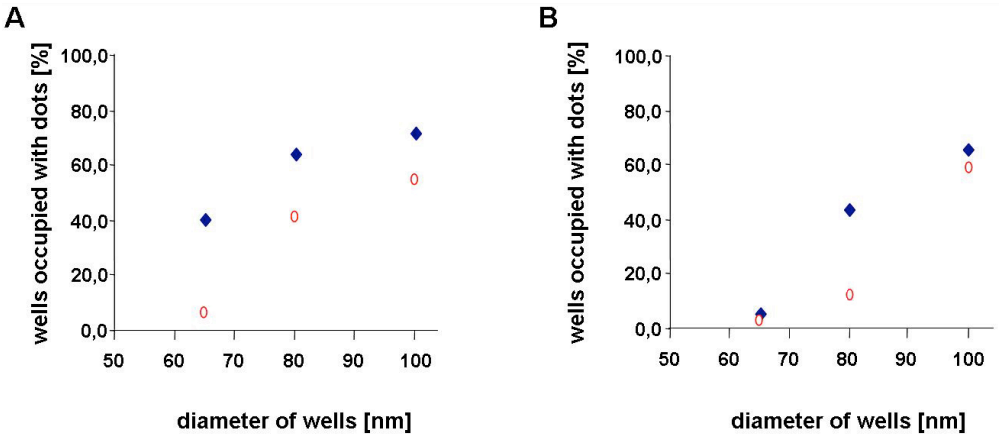

Figure 31: **The number of wells, containing gold dots, is dependent on the speed, on the diameter of the well and on the polymer.** A: the spin speed was set to 2000 rpm. The PS 245-*b*-P2VP 223 polymer (blue squares) yields in a higher percentage of occupied wells compared to the larger PS 2076-*b*-P2VP 571. B: Also at a spin speed of 8500 rpm the occupation with the smaller polymer (blue squares) is higher as with the larger one (red circles).

after spin coating with the PS 245-*b*-P2VP 223 polymer solution. With rising the spin speed to 8500 rpm this number goes down to 65 %. For the PS 2076-*b*-P2VP 571 the values are at 54 % for the 2000 rpm spin speed and 58 % for the faster speed. As the diameter of the wells is decreasing, the percentage of occupation is decreasing for both polymers at both spin-speeds. For the PS 245-*b*-P2VP 223 one can reach a maximum occupation of 39 % of the 65 nm wells at a spin speed of 2000 rpm, while it is decreasing to 5 % for the higher speed. For the 80 nm wells the values are 63 % (at 2000 rpm) and 43 % (at 8500 rpm). The values for the PS 2076-*b*-P2VP 571 are 6 % (at 2000 rpm) and 3 % (at 8500 rpm) for the 65 nm wells and 40 % (at 2000 rpm) and 12 % (at 8500 rpm) for the 80 nm wells.

In the spin coating process, the micelles are pulled inside the wells by capillary forces. Evaporation of the solvent leads to a rupturing of the micellar film on the surface. The solvent filled wells are attracting the micelles, pulling them inside. This effect is dependent on the interaction and surface tensions of the solvent, the polymer, and the surface [15]. The number of of micelles trapped inside a structure is dependent on the spin speed, the depth of the wells and the mass of the polymer. The faster the spin sped, the higher are the forces on the micelles. The diameter of the PS 2076-*b*-P2VP 571 micelles overcomes the diameter of the structures. So they have to be deformed in order to be positioned inside the wells. The needed force for the deformation of the micelle is obviously to high to be overcome by the capillary forces, pulling the micelles inside the wells. Especially at higher spin speeds, where additionally gravitational forces are pulling the micelles away from the holes. The smaller micelles of the PS 245-*b*-P2VP 223 can easily sink inside the wells, as here the the micelles have approximately the same or even a smaller diameter. This results in a higher occupation at lower as well as at the faster spin speeds, as there is no additional force needed for the deformation of the micelles.

The average number of gold dots inside the occupied wells reaches a maximum value of 2,3 for the PS 2076-*b*-P2VP 571 polymer, spin coating the 100 nm wells at a speed of 8500 rpm. A value of one can be reached only for the 65 nm wells, spin coating with 8500 rpm with either of the polymer solutions (table2). Calculated was the average only by counting the number of wells containing gold dots.

Table 2: Average number of gold dots inside the wells of a ZMW.

		100 nm wells	80 nm wells	65 nm wells
245-*b*-223	2krpm	2,2	1,7	1,3
	8,5krpm	1,6	1,4	1,0
2076-*b*-571	2krpm	2,2	1,4	1,0
	8,5rpm	2,3	1,1	1,0

The average number is higher for the micelles, obtained by the smaller polymer, than by the one, obtained by the PS 2076-*b*-P2VP 571 polymer. Due to sterical effects, it is hardly possible that more than one micelle sinks inside a

well with a diameter of 65 nm. Capillary forces between the micelles and the wells lead to an assembly of micelles in the larger wells, leading to higher occupation. If the gravitational forces are increased by higher spin speeds, the number of gold dots inside one well decreases.

To see if the effect can be also observed for other spin speeds, meaning smaller differences in the applied forces, the experiments have been done also at 1000 rpm and at 4000 rpm for the smallest, the 65 nm, wells (figure 32).

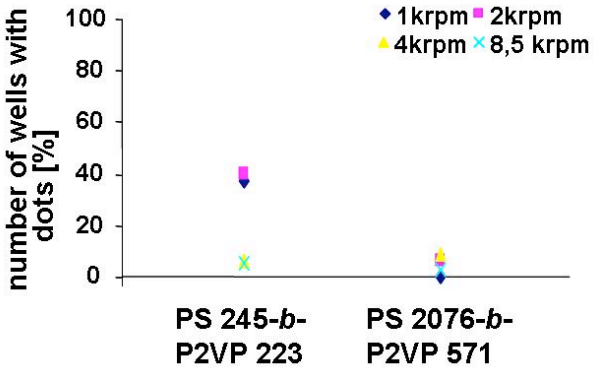

Figure 32: **Spin coating of a prestrucutred surface with wells of a diameter of 65 nm.** The number of wells, containing gold dots is strongly dependent on the polymer.

For the PS 245-*b*-P2VP 223 polymer the difference between 1000 rpm and 2000 rpm are negelectable. For the slowest spin speed the percentage of occupied wells is 37 %, while it is 39 % for the 2000 rpm. The same is for the 4000 rpm and the 8500 rpm spin speeds. The values change from 6 % to 5 %. For the PS 2076-*b*-P2VP 571 polymer the values are ranging from 1% (at 1000 rpm), over 6 % (at 2000 rpm), and 8 % (at 4000 rpm), to 3 % (at 8500 rpm). There is hardly any difference between the different spin speeds. Obviously, the needed force for the deformation of the micelles is high and cannot be overcome by capillary forces. In contrast are the results for the PS 245-*b*-P2VP 223 polymer. There is a threshold, above which the micelles are ruptured away from the surface. Spinning with 4000 rpm or 8500 rpm is not showing significant differences in the number of dots per well. THe forces, applied by spinning with 4000 rpm overcome the capillary forces, attracting the micelles to the structure.

With block copolymer micellar nanolithography it is therefore not only possible to obtain flat structures with a nanopatterning of gold dots. By choosing the fitting parameters, as the mass of the polymer and the spin speed, it is also possible to functionalize prepatterned substrates in a controlled way.

4 Immobilization of Inorganic Nanocrystals

Various applications of nanoparticles require tailor-made immobilization strategies based on the individual characteristics of the employed particles. In this part of the work, different methods for the immobilization of inorganic nanocrystals (NCs) are investigated. The gold nanopatterned surfaces, presented in chapter 3 of this work, are good platforms for the attachment of NCs, as the distance between the gold dots on the surface can easily be adjusted (figure 33). Thus the distance between neighboring particles here is much larger as in previous described methods and it can be tuned in a much broader range than achievable by changing the length of the surfactants.

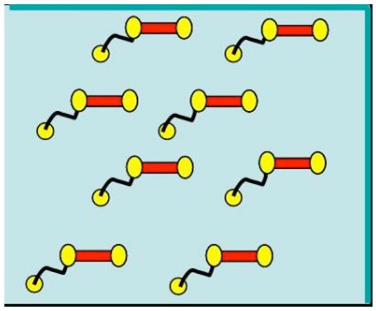

Figure 33: **General method for the attachment of inorganic nanocrystals on nanopatterned substrates.** The NCs are immobilized on the quasi-hexagonally arranged gold dots on glass or silicon substrates. This enables the control of the interparticle distance as well as their density

In a first approach we are using short organic molecules as linkers between the NCs and the gold dots on the surface. Different alkyl molecules with a thiol functionalization at both ends of the chain (alkyl dithiols) are utilized. While one of the functional thiol groups can bind to the gold dot on the surface, the other works as anchoring point for nanocrystals wearing a gold tip at either end.

Due to their tunable electronic and optical properties semiconductor NCs have tremendous promise for *in vitro* and *in vivo* imaging. They can emit light in regions of the spectrum where tissue is transparent [200]. For the processibility of the nanocrystals, it is necessary to transfer them into aqueous solution [110]. Under these conditions a second approach was successfully employed, using DNA as linking molecule.

In a third approach the micellar nanolithography is combined with the semiconducting NCs. Exchange of the TOPO ligand by hydrophilic molecules leads the CdSe particles into the core of the micelle. Dip-coating substrates enables the precise positioning of preformed particles, without the use of linkers.

4.1 Employed Nanocrystals

We applied the different immobilization strategies successfully to spherical CdSe quantum dots (figure 34A), $CoPt_3$-Au heterodimers (figure 34B), CdSe-Au dumbbells (figure 34C), and Co-Au matchsticks (figure 34D).

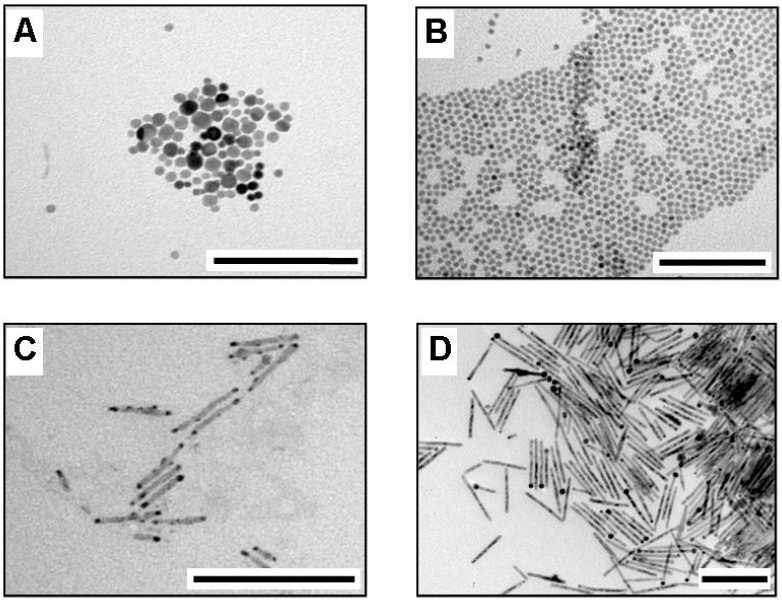

Figure 34: **TEM images of colloidal nanocrystals, employed in this work:** A $CoPt_3$-Au heterodimers (image taken by A. Fiore, NNL, Lecce, Italy), B: spherical CdSe nanoparticles (image taken by Dr. S. Kudera, MPI, Stuttgart, Germany), C: CdSe-Au dumbbells (image taken by A. Salant, HUJ, Jerusalem, Israel), D: Co-Au matchsticks (image taken by Dr. K. Soulantica, INSA, Toulouse, France). The $CoPt_3$-Au heterodimers, the CdSe-Au dumbbells and the Co-Au matchsticks were immobilized over their gold domains. The spherical CdSe particles on the other hand were directly attached to the surface in a micellar approach.

CdSe rods and dots are of interest because of their unique fluorescent properties. It is possible to grow gold tips selectively to one or both ends of the rods [137]. Even though the growth of the gold domain quenches the fluorescence of the particles, it also improves their application, as these can serve as anchoring point for the specific modification of the particles [201]. The size of the gold tips can be adjusted by the amount of precursor and the reaction time (figure 35). Usually it is in the range of a few nanometers. The CdSe rods used for this work have a diameter of three nanometers whereas the gold tips range from 3 to 5 nm. The spherical CdSe dots had a diameter of 4 nm.

CdSe-Au dumbbells, $CoPt_3$-Au heterodimers, and Co-Au matchsticks are immobilized to a nanopatterned gold surface over their gold domains as these

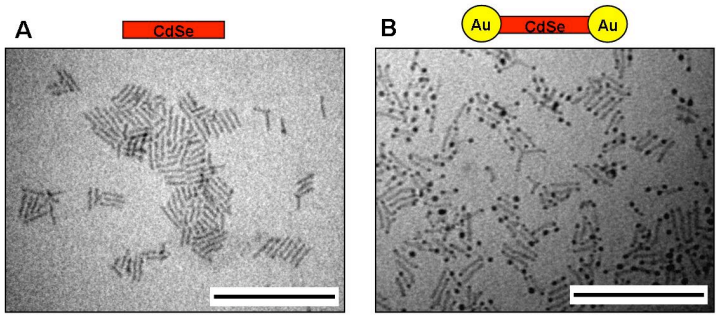

Figure 35: **Growth of Gold domains to CdSe rods.** TEM images of CdSe rods (A) and dumbbells (B). The growth of the gold domains at the end of the rods can be followed in the electron microscope. The scale bars correspond to 100 nm. The images are kindly provided by A. Salant, HUJ, Jerusalem, Israel.

are offering specific binding sites for thiol containing molecules. In this work the used $CoPt_3$-Au heterodimers had a smaller $CoPt_3$ domain with a diameter of eight nanometers. The attached gold domain is in the range of about 20 nm in diameter. The cobalt particles, used in this work, had a length of 40 - 50 nm and a diameter of 5 nm. The gold ends have a diameter of 5 - 6 nm. The spherical CdSe dots have been immobilized on the surface in a micellar approach.

4.2 Dithiol Molecules as Linker

4.2.1 Alkane Dithiols

Thiolgroups preferably bind to gold, with a strong bond interaction between sulfur and gold estimated to be 40 - 45 kcal/mol [202]. It is known that alkane thiols form stable self assembled monolayers (SAM) on homogeneous gold in an all-trans conformation. However, variation of the functional group at the chain end can have an enormous effect on the formation of the SAM, which usually forms in two steps. Initially, the thiol-head groups adsorb to the gold surface. This happens within minutes or even seconds. In a second phase the hydrocarbon tails orient themselves, which can take up to hours. This second step is therefore most affected by the variation of end groups [202].

Using bifunctional thiols, it is possible that the second thiol group also attaches to the gold, at least in certain amounts. To ensure that a freely addressable thiol group is present on every gold dot on the surface it is important to choose a molecule which can not form loops. *Kohale* et al. have shown that alkane dithiols with a chain length of eight carbon atoms hardly form any loops [203]. In microcantilever sensor experiments they showed that only one thiol group binds to the gold while the other is freely accessible (figure 36).

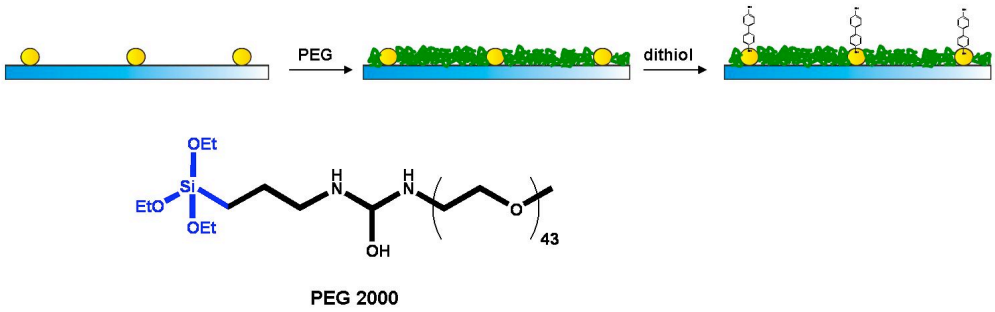

Figure 36: **Schematic drawing of the surface preparation.** The glass or silicon oxide between the gold particles on the surface is passivated by a monolayer of PEG. The dithiol crosslinkers (figure 37) are attached only to the gold, resulting in a thiol functionalization of the nanodots. The PEG is needed to prevent added molecules to physisorb on the surface.

With 1,6-hexanedithiol (figure 37) it is therefore possible to get active thiol groups on the gold dots of the surface. Another possibility to immobilize free thiol groups on the surface is to work with dithiols with a rigid backbone. Their molecular structure prevents bending and thus the formation of loops. One example for these kinds of molecules is a biphenyl molecule. Due to their stiff backbone the biphenyl crosslinkers are not able to form loops, leading to addressable thiol groups on the gold nanoparticles on the substrate. Therefore, the biphenyl-4,4'-dithiol (figure 37) is an alternate molecule for the immobilization of inorganic nanocrystals over their gold tip to the surface.

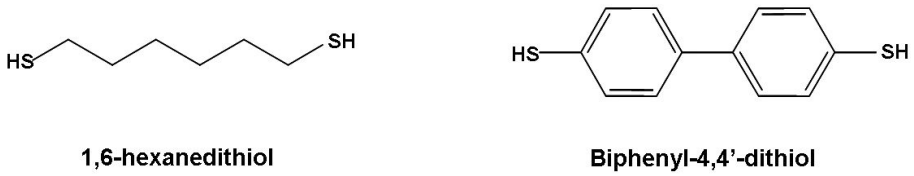

Figure 37: **Chemical structure of the used bithiol molecules.** Left: 1,6-hexandithiol is used for the immobilization of CdSe dumbbells and $CoPt_3$ heterodimers. Right: Biphenyl-4,4'-dithiol is used for the attachment of Co matchsticks.

Intensive rinsing after the functionalization is necessary to get rid of all free thiol molecules. If they stick on the surface, the NCs bind to the substrate instead of the gold dots. If they get diluted in solution again, chains of the NCs are forming. They can be connected with each other over their gold domains. To prevent physisorption of linkers or nanocrystals to the silicon substrate between the gold nanodots, a monolayer of poly-ethyleneglycol (PEG) is first bound to the surface. Therefore the PEG molecule is modified with a

trimethoxysilane group through which a covalent linkage to the silicon oxide surface is possible. These PEG monolayers have a height of about 6 nm [204], which is less than the diameter of the gold dots. Thus, they are still addressable by functional molecules (figure 36).

These passivated and functionalized gold dot surfaces can now be used for the immobilization of different kinds of nanocrystals (figure 38) with a defined interparticle distance.

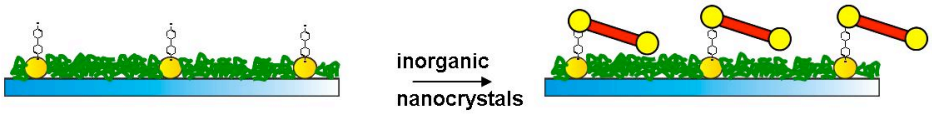

Figure 38: **General immobilization of inorganic nanocrystals via dithiolated molecules.** Inorganic nanocrystals (NCs), containing a gold domain, are incubated on a thiol functionalized nanopatterned surface (figure 36). The linkage is formed between the gold on the surface and the one on the NC. The PEG layer prevents the particles to stick on the silicon substrate.

4.2.2 Heterodimers and Dumbbells

$CoPt_3$-Au heterodimers, carrying their gold domain on one side, are successfully attached to a 1,6-hexanedithiol functionalized gold nanodot surface (figure 39A). As the diameter of the gold tip of the heterodimers (20 nm) is larger than the one of the particles on the surface (10 nm) it is not clearly visible how the heterodimers are lying on the substrate. However, as the diameter of all particles on the surface is increased, obviously every gold dot on the surface is occupied by at least one heterodimer.

It is also possible to link dumbbells to these surfaces. It is known, that the free thiol groups on the surface favour the gold rather than the CdSe. As the gold tips are placed at the end of the rods, the matchsticks or dumbbells are selectively attached over these ends (figure 39B).

Analyzing the sample in the AFM gives a height profile, which allows a more detailed analysis of the attachment (figure 39C). The gold domain of the dumbbell is laying on top of one gold dot on the surface. The blue arrow marks a height of about 7 nm. This corresponds to the diameter of the dumbbell, adding the gold dot from the surface minus the thickness of the PG passivation layer. The diameter of the gold-tips on the dumbbells is in the range of four to five nanometers. Due to the PEG passivation the gold dots from the surface have a visible height of about two to three nanometers. This together results in a height of seven to eight nanometers, as can be seen in the AFM. The detected length (red arrow) of 70 nm corresponds to the length of the here used CdSe dumbbells. The diameter of the gold domains is larger than the diameter of

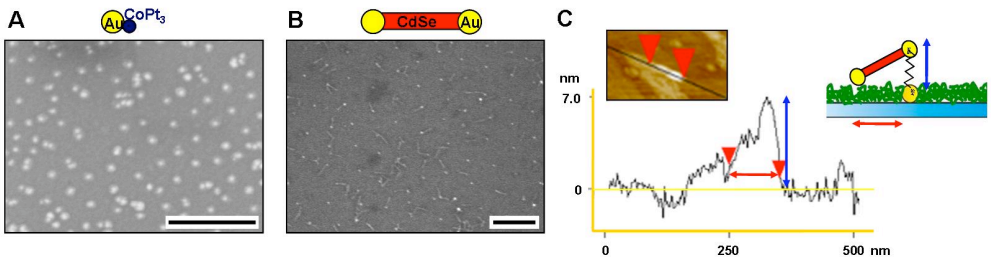

Figure 39: **SE micrographs of inoganic NCs, immobilized on a nanopatterned surface via dithiol linkers.** A: $CoPt_3$ heterodimers and B: CdSe dumbbells immobilized on a nanopatterned surface. The scale bars correspond to 200 nm. C: AFM image of CdSe dumbbells on a surface. The dumbbell is lying with one end on a gold dot, while the other end probably sinks into the PEG.

the CdSe rod itself. This is visible in the peak, where the dumbbell lies on the dot of the surface. Such a peak occurs not at the left end of the rod. This might be due to the PEG layer. The dumbbell can sink inside it, which is additionally forced by the pressure, coming from the AFM tip.

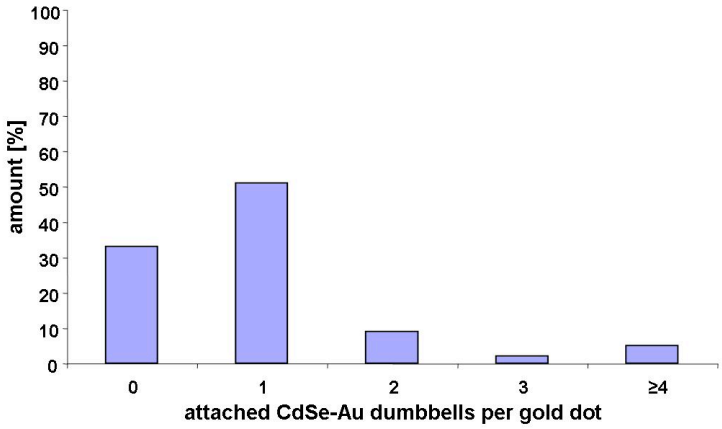

Figure 40: **Number of CdSe dumbbells attached to one gold dot.** To 33 % of the gold dots there are no dumbbells connected. 51 % are decorated with one CdSe-Au dumbbell, 9 % with two of them. 2 % are surrounded by three dumbbells, 5 % by four or more.

Counting the number of gold dots, occupied by a nanocrystal is quite difficult for the $CoPt_3$-Au heterodimers, as they hardly can be distinguished from the pattern on the surface. In case of the CdSe-Au dumbbells this is possible, as the rods can easily be distinguished in the SEM (Figure 8). 33 % of the gold dots are without any modification after the attachment of the dumbbells. Half of the dots (51 %) are connected with one NC, 9 % with two. Three CdSe dumbbells surround about 2 %, while the last 5 % have 4 or more particles around

them. The dissemination is similar to a Poisson's distribution, but does not follow exactly.

In a surface area of 1 μm^2 one finds around 35 CdSe dumbbells, which are not connected with any gold dot on the surface. It is not possible to distinguish whether the 1,6-hexandithiol sticks inside the PEG layer or the particles themselves. The attached particles are not oriented in any way. Also intensive rinsing after the attachment is not leading to an alignment. Even though most of the gold dots are connected to only one CdSe dumbbells, there occur clusters of dumbbells around the gold dots. It is hard to distinguish, if all particles are really attaching the gold dot or if the dumbbells are connected to each other.

4.2.3 Cobalt Matchsticks

With the biphenyl-4,4'-dithiol magnetic cobalt matchsticks are immobilized over their gold tip to the nanostructured surface (41).

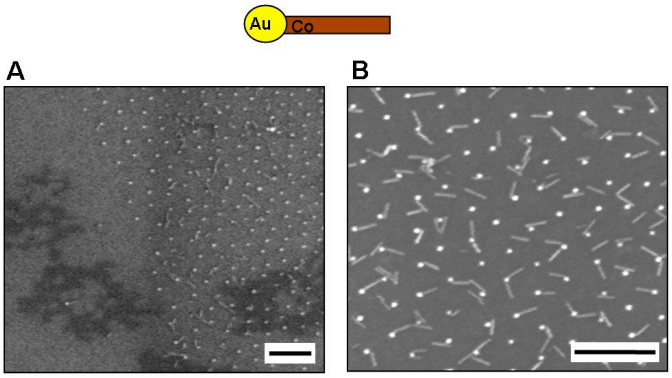

Figure 41: **SE micrographs of a successful immobilization of Co matchsticks to a nanopatterned surface.** A: The non patterned are serves as internal control for the specificity of the attachment to the gold. dots B: Co rods immobilized on the surface. The scale bars correspond to 200 nm.

The SEM analysis revealed that the Co matchsticks are linked to the gold dots on the surface over their gold tip. However, as the gold domain on the matchstick is smaller then the gold dot on the surface, it is not directly visible. The part of the surface covered by the PEG layer stays free of Co nanoparticles, being an internal reference on the surface (figure 41A). Due to their random orientation in liquid there is no order of the particles on the substrate after the attachment (figure 41B).

Analyzing the SEM images, the number of attached Co-Au matchsticks per surface gold dot can be determined (figure 42). 21 % of the gold dots stay free. 51 % have one particle attached to them, while 20 % have two. Three particles can be found around 5 % of the particles, 4 or 5 NCs surround the

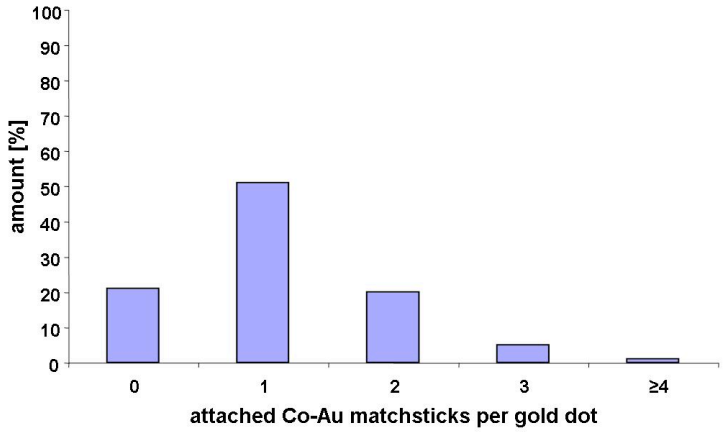

Figure 42: **Distribution of Co-Au matchsticks linked over a biphenyl to the surface.** 21 % of the gold dots stay free, 51 % have one Co-Au matchstick attached, 20 % have two. 5 % of the gold dots are surrounded by three matchsticks. 4 or 5 matchsticks are attached to the last percent of gold dots.

last percent of dots. The dissemination is similar to the one obtained by the attachment of the CdSe-Au dumbbells over 1,6-hexanedithiol, but the number of free gold dots on the surface is lower. The higher occupation rate can be due to the longer reaction time inside the glove box. Looking in more detail on how the particles are attached to the surface, it becomes obvious that not all particles are attached at their ands but at their sides. Looking to the TEM images of the cobalt matchsticks, one finds particles, having their gold not on the tip, but at the side. This is only a small percentage, but is reflected on the surface. Counting the number of nanoparticles, not attached to a gold dot on the surface, on finds about 40 Co-Au matchsticks in a surface area of 1 μm^2. This amount is analogous to the one from the CdSe-Au dumbbells. It is again not possible to distinguish if the linker or the particles stick to the PEG layer, as neither more intensive rinsing after the functionalization nor after the particle attachment led to a decrease of the number.

The Co-Au matchsticks show a magnetization along their z-axis, which can be used for the alignment on the substrate. Application of a magnetic field during evaporation of the solvent should lead to an orientation of the particles parallel to the external field (figure 43)

A magnetic field of 0,111 T [13] did not show any effect on the order of the substrate (figure 44A). The Co matchsticks are still randomly distributed over the surface. Under a magnetic field of ten times the magnitude hardly any single crystals are attached to the surface. The force of the magnetic field seems to be strong enough to detach the particles from the surface again.

[13]The experiments under a megnetic field have been carried out together with Dr. K. Soulantica, INSA, Toulouse, France.

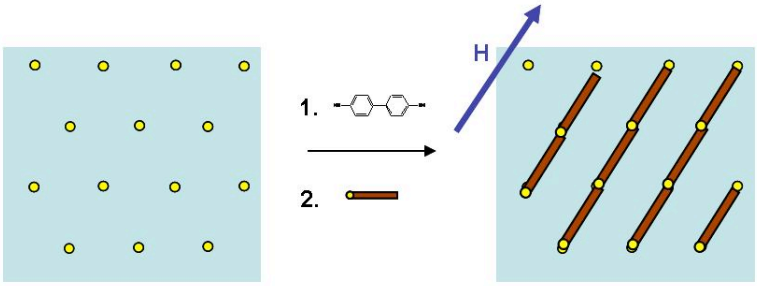

Figure 43: **Schematic drawing of the alignment of cobalt matchsticks in a magnetic field H.** A PEG passivated, thiol functionalized nanopatterned substrate is incubated with a solution, containing the Co matchsticks. Application of a magnetic field leads to the alignment of the particles in the direction of the external field.

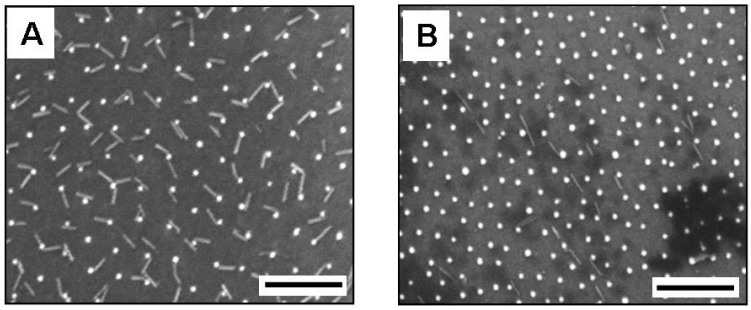

Figure 44: **SE micrographs of Co matchsticks, after alignment in a magnetic field** A: applying a magnetic field of 0,111 T did not show any effect. B: A magnetic field of 0,555 T aligns the rods in one major direction. The number of occupied dots is decreased. The scale bars correspond to 200 nm.

Under a magnetic field of 0,555 T the cobalt matchsticks become oriented on the surface (figure 44B), but the coverage of the gold particles on the surface is less than under the lower magnetic field. They align along one axis, which is probably the direction of the applied magnetic field. The original direction of the magnetic filed is not known. All working steps with the cobalt particles require working under inertgas conditions. A precise handling of the silicon substrates is extremely difficult. During the setup of the magnet it might happen, that the substrate is turning. The field lines are then no more perpendicular to the dipping line. As after the application of the magnetic field further rinsing is required, it is not possible to mark the original direction of the applied magnetic filed. It can be assumed by the alignment of the rods, as they have their main axis of magnetization along their z-axis. The low coverage can be due to the rigid linker molecule. Once, the particles are attached, they are forced in a new orientation by the magnetic field. The stiff biphenyl group is not able to twist or bend around in a wide range. Application of the magnetic field already during the attachment is not possible, as here the particles stick to the wall of the flask, in which the reaction is carried out, instead of binding to the surface.

We have shown the successful immobilization of inorganic nanocrystals, carrying a gold domain, on a nanopatterned surface via dithiol linkage. The gold dots on the surface work as anchoring points for the dithiol molecules. By choosing fitting bifunctionalized molecules it is possible to obtain surfaces with thiol functionality on the gold dots. A monolayer of PEG successfully prevents physisorption of the molecules on the glass or silicon wafer. The inorganic NCs can now specifically bind to the gold dots over their gold domains. AFM analysis hints that their gold domain is lying on top of the gold dots on the surface. The dissemination is in both cases similar to a Poisson's distribution, but does not follow exactly. Application of an external magnetic field enables the orientation of anisotropic magnetic cobalt particles along their z-axis. An improvement of the alignment might be possible by choosing a more flexible linker.

4.3 DNA as Linker

The linkage described above over thiols can only be controlled via the concentration of the reaction partners. A more flexible but very precise immobilization of water-soluble particles can be realized by working with DNA as linker molecule. DNA enables the specific attachment via hybridization of complementary strands. The hybridization is a potentially reversible process. By heating the substrate the second strand can be removed again, if the melting temperature is overcome. The melting temperature of the DNA strand can be engineered by choice of the nucleotides.

Most colloidal nanocrystals can either be synthesized in aqueous solution or in organic solvents. However, so far some materials such as Co still need to be synthesized in organic solvents at high temperature. These conditions

lead to improved shape control, high crystallinity and good monodispersity of the nanocrystals. This process involves their surface to be coated with a monolayer of surfactants that render the NCs hydrophobic. Several methods exist for converting hydrophobic materials into hydrophilic particles, which is a prerequisite for biological applications. They rely on two main principles: either the particles are enclosed by a shell of new material (silanization, polymer coating), or the surfactants are exchanged with amphiphilic molecules as depicted in figure 45 [110, 205].

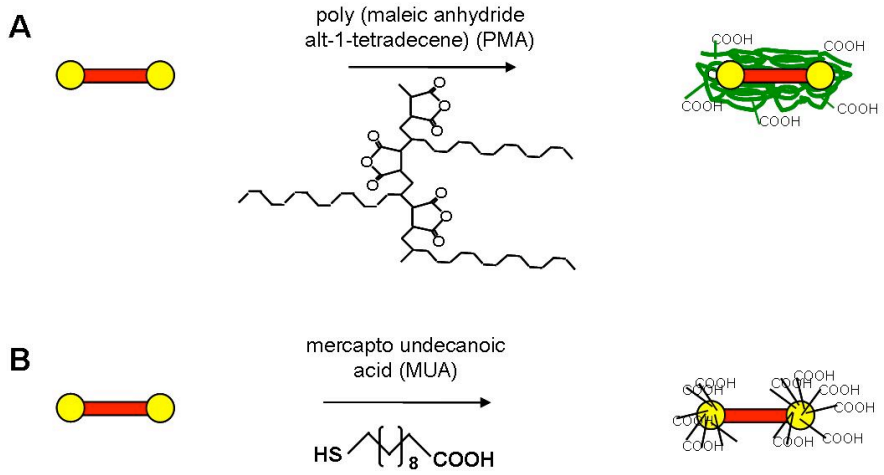

Figure 45: **Transfer of TOPO coated NCs from organic solvent into water.** A: Formation of polymer shell around the particle. The polymer (poly(maleic anhydride alt-1-tetradecene, PMA) intercalates with TOPO. Therefore this method is also applicable to any sort of particles, also without gold domains. B: Ligand exchange specifically at the gold tips of the particles with mercaptoundecanoic acid (MUA). This enables further modification only at the gold domains.

In the first case, a second layer of organic molecules is added around the TOPO coated particles. This layer consists of amphiphilic molecules that can intercalate with the first hydrophobic surfactant layer with their hydrophobic chain. The hydrophilic part of the polymer ensures the water solubility of the particles. For improved stability of the system a cross-linked polymer can be used. Poly(maleic anhydride alt-1-tetradecene) (PMA) intercalates in the TOPO shell of pre-synthesized particles. Addition of bis(6-aminoheyl)amine results in cross-linking of the polymer chains around the nanoparticles. The NCs become water soluble upon hydralization of the unreacted anhydride groups and can be further functionalized at the resulting carboxylic acid groups [206]. The functional groups are distributed homogenously all over the crystal. The diameter of the particles is increased by about one nanometer through this procedure. The major properties of the particles (e.g. fluorescence, magnetic moment) are not affected by this transfer into water [206].

The second mentioned approach uses the exchange of surfactants. Am-

phiphilic molecules with a thiol group can exchange the phosphates on the gold domains of the NCs. Mercaptoundecanoic acid (MUA) binds with the thiol group preferentially to the gold domain of the particle while the carboxylic acid group renders them water-soluble. With this approach the specific functionalization at the gold tips remains possible.

We show the successful attachment of DNA to nanoparticles. In a first step, they are transferred into water by two different methods, a ligand exchange and the formation of a polymer shell. In both cases, it is possible to add DNA to the NCs. The so modified particles are than attached to a surface, carrying the complementary DNA strand on the gold nanodots.

4.3.1 Functionalization of NCs with DNA

Single stranded DNA (ssDNA) can be bound to nanocrystals in aqueous solution. Two approaches have been tested. At first, ssDNA with an amino group at the 5'-end (H_2N-DNA) is attached to polymer coated CdSe rods via standard EDC/NHS chemistry. The carboxy groups around the polymer shell serve as reaction partners for the amino group of the DNA strand resulting in a connection over a peptide bond (figure 46A).

The second method is based on the ligand exchange of the particles. The MUA coated CdSe dumbbells are treated with a thiol functionalized ssDNA strand. The MUA can now be exchanged by the ssDNA strand (figure 46B).

Additionally, DNA represents a particularly good ligand system. The negatively charged phosphate backbone attaches on the CdSe particle and thus stabilizes it [37, 174, 200].

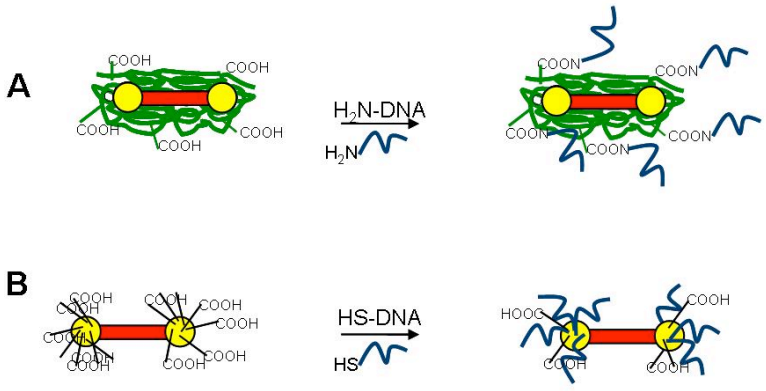

Figure 46: **Schematic of the functionalization of water-soluble inorganic nanocrystals (NCs) with DNA.** A: The polymer-coated nanoparticles can be functionalized with amino-DNA with EDC/NHS coupling chemistry. The DNA is distributed homogenously over the surface. B: Thiol-DNA can exchange the mercaptoundecanoic acid (MUA), resulting in a specific functionalization of the NCs with DNA at the gold domains.

The successful attachment of the DNA to the nanocrystals can be controlled in both cases by optical absorption measurements. The DNA modified dumbbells are allowed to hybridize with a complementary ssDNA strand, carrying a Cy3 dye at the 5′ end, here only used as absorber for light. After cleaning with a cut off column (MW = 50kDa), both solutions are analyzed by measuring their absorbance spectra (figure 47).

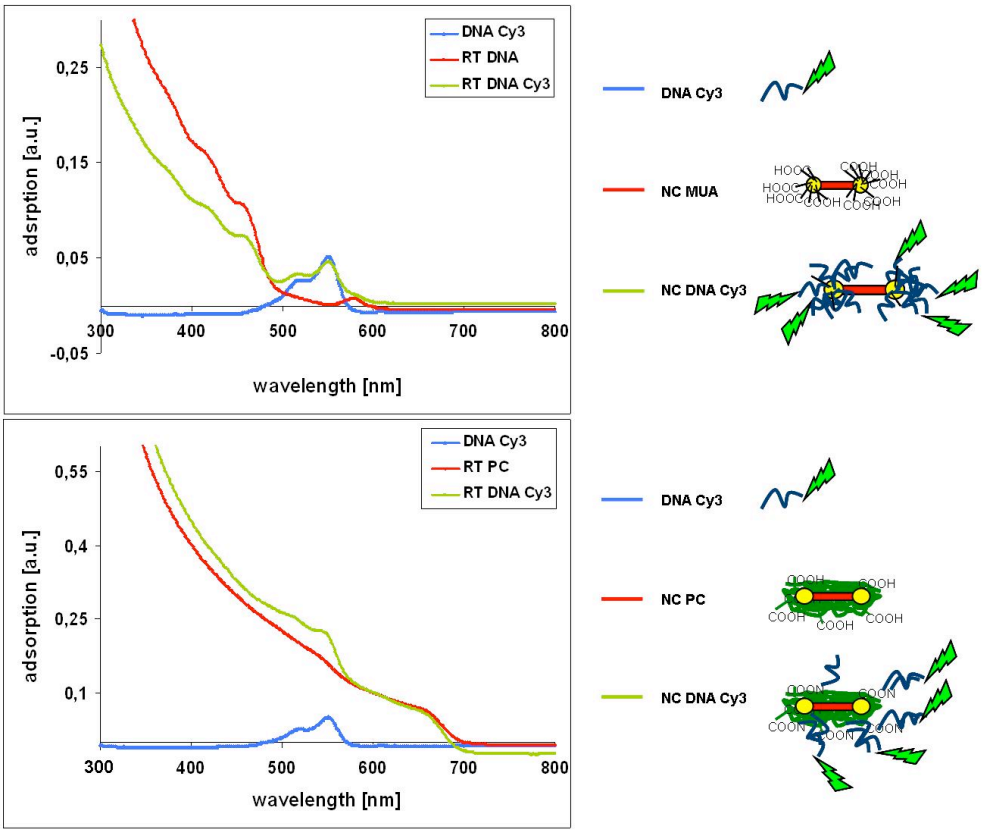

Figure 47: **Absorption spectra showing the successful immobilization of DNA to CdSe-Au dumbbells after transferring them into water with MUA (A) or after polymer coating (B).** A: Cy3-labelled DNA (blue line) as well as the MUA coated NCs (red line) work as reference. After the hybridization the specific peaks of both are visible (green line). B: Cy3-labelled DNA (blue line) and polymer coated NCs (red line) work as reference for the DNA coated nanoparticle (green line).

The spectra of DNA modified CdSe-Au dumbbells, transferred into water with MUA (figure 47A, red line) shows absorption at wavelengths below 600 nm, which corresponds to the absorbance of the dumbbells. The Cy3 absorption peak at 550 nm is clearly visible in the reference spectrum of the Cy3 labeled ssDNA (figure 47A, blue line). After the successful hybridization the characteristic peaks of both become visible (figure 47A, green line). Repeated

washing is not changing the relative intensities. The absorption below 500 nm results from the NC, while the one at 550 nm has its origin in the successfully attached DNA, carrying the Cy3 dye.

The same measurements were performed for polymer coated CdSe dumbbells (figure 47B). The polymercoated dumbbells (red line) do not show absorption overlapping with that of Cy3 (blue line). After hybridization a peak at 550 nm is detectable (green line), proving the successful hybridization of the DNA strands. Due to the polymer shell, the noise in the spectrum of the NC is extremely broad. Which might also be due to the gold tips, as they do not have a TOPO coating around them. Nevertheless, the shoulder at 550 nm occurs after the hybridizaiton with the complementary Cy3 labeled DNA.

It is possible to functionalize NCs with ssDNA. Polymer coated as well as MUA modified particles have successfully been modified with it. Comparing the two methods, shows advantages as well as disadvantages for both methods.

The polymer coated particles are more stable in aqueous solution than the MUA modified ones. The polymer shell forms uniformly around the particle, forming a protecting shell around it. It is therefore possible, to transfer all kind of particles into aqueous solution, independent from their material, as long as the surfactant contains a long alkane chain, which intercalates with the polymer [207]. It is not necessary, to grow gold domains to the particles, which is then quenching the fluorescence of semiconducting particles for example.

Inorganic NCs, transferred into water by ligand exchange with MUA, often start to precipitate already after few days. Additionally, their fluorescent properties are suppressed by the gold domains. Nevertheless, there is one major advantage by working with MUA. The specifity of the gold domains stays intact. It is possible to exchange the MUA by other thiol containing molecules, resulting in a specific functionalization of the gold domains. This point is the reason, why further experiments have been always carried out with particles, transferred into water via ligand exchange with MUA.

4.3.2 Functionalization of Nano Patterned Surfaces with DNA

In order to align the DNA modified particles the complementary ssDNA has to be immobilized on the gold dots of the surface. In order to prevent physisorption of the DNA on glass, a PEG monolayer was brought on the surface. The successful attachment of the ssDNA on the surface was followed by fluorescence measurements (figure 48). Staining the ssDNA with SYBR Green I the fluorescence at 568 nm can be observed.

SYBR Green I is widely used to visualize DNA. In contrast to many other staining methods, as ethidium bromide (EtBr), it is also sensitive to ssDNA. The emission wavelength is in the green spectrum at 520 nm for dsDNA, but working with ssDNA shifts the emission peak towards larger wavelengths.

After the nanoparticles as well was the nanopatterned surface has success-

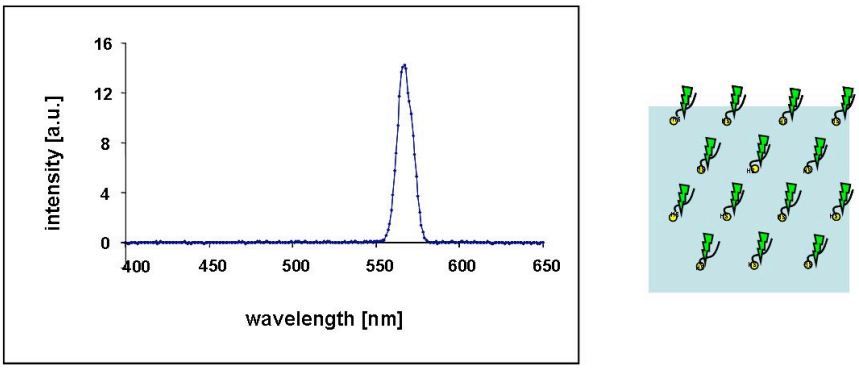

Figure 48: **Fluorescence spectrum of a surface, modified with ssDNA after staining.** The staining was performed, using SYBR Green I which can also be used for the staining of ssDNA. Fluorescence is therefore detected at 568 nm.

fully been modified with DNA, the particles can now be immobilized on it. Hybridization of the complementary DNA strands should result in a more controlled alignment of the particles.

4.3.3 Hybridization

The hybridization of the DNA modified CdSe-Au dumbbells with the DNA modified nanopatterned substrate takes place at room temperature. Initial heating of the particles and the surface close to the melting temperature of the ssDNA increases the reaction kinetics, as eventually occurring intramolecular bridges are cleaved. The successful hybridizaiton was proved in SEM analysis (figure 49).

MUA coated and DNA functionalized CdSe-Au dumbbells are attached over their gold domain to the gold dots of the surface. The maximum number of rods attached to one gold dot was found to be three (see inset figure 49). Analyzing the surfaces, by counting the number of rods attached to each gold dot, results in an average number of two rods per gold dot, which was found at 78 % of the gold dots. Only 4 % of them were not functionalized with any nanocrystal. 9 % of the gold dots have one dumbbell attached to them. The maximum number of dumbbells was found to be three at 9 % of the gold particles on the surface (figure 50).

In an area of 1 μm^2 up to 30 unbound NCs were found. This number has been reduced to a maximum of 13 by intensive rinsing. We were not able to distinguish if it is already the DNA, sticking to the PEG, or the modified particles, or probably both.

The particles are aligned in two directions. The alignment is caused by applying a strong flow (50 ml/min) on the surface after the hybridization. The DNA is a flexible molecule, which can be bended. This enables the NCs to

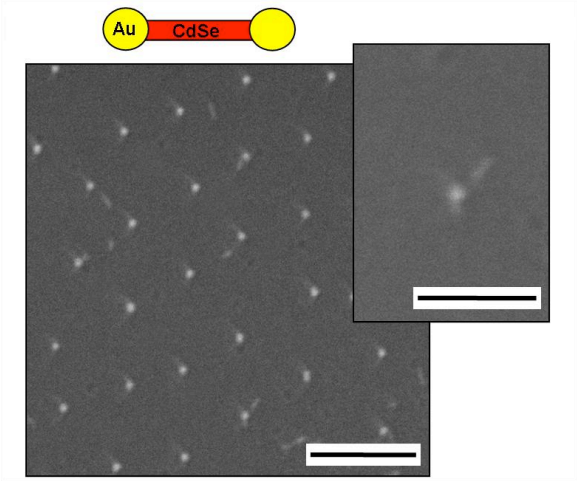

Figure 49: **SEM image of CdSe-Au dumbbells immobilized on a surface with DNA.** The DNA modified CdSe-Au dumbbells are immobilized on the surface after successful hybridization. Most gold dots on the surface have two dumbbells attached, while the maximum number was found to be three (see inset). The scale bars correspond to 100 nm.

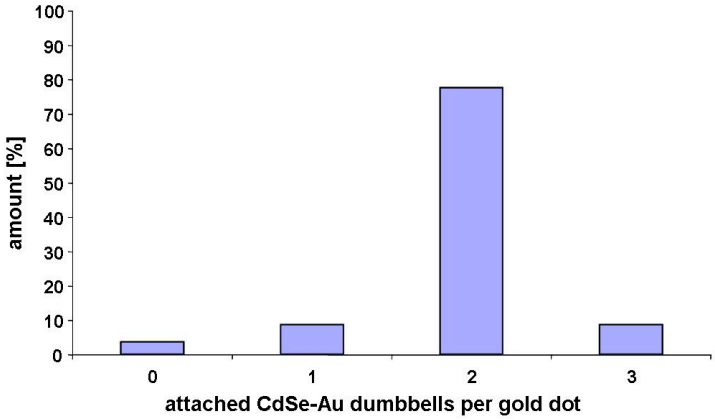

Figure 50: **CdSe-Au dumbbells attached to the surface via DNA assembly.** 78 % of the gold dots is covered with two dumbbells. 9 % have one dumbbell and further 9 % have three, which was also the maximum number. Only 4 % of the dots remain unoccupied.

bend on the wet surface around the particles. After drying the surface, the particles can not be moved again by application of a further flow. Hybridization under flow conditions should allow the alignment of the CdSe-Au dumbbells in one direction. To see, if hybridization under a flow is possible, we performed QCM-D experiments, following the kinetics of the attachment steps (Figure 19A, B). A schematic of the single steps is shown in figure 51C.

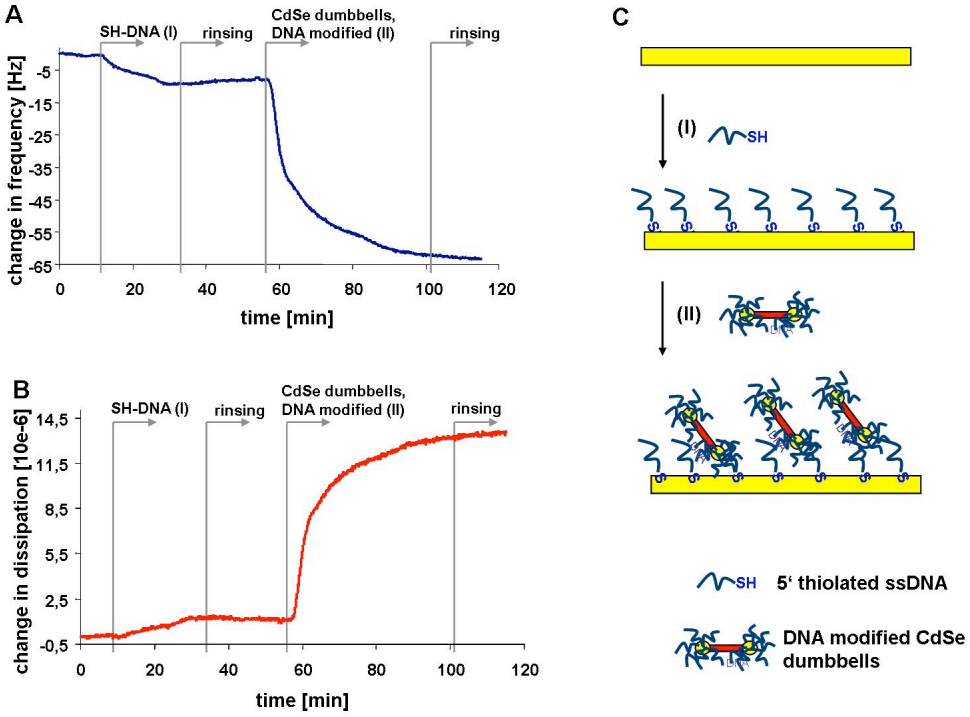

Figure 51: **QCM-D measurement of DNA modified dumbbells on a homogenous Au crystal.** A, B: Under contant flow 5′ thiolated DNA is attached to the gold, resulting in a change in the frequency (A) as well as in the dissipation (B) (t = 9-28 min). After saturation and intensive rinsing, to remove physisorbed DNA, the DNA modified CdSe dumbbells are added (t = 56-100 min), resulting in changes in frequency (A) and dissipation (B). Even after intensive rinsing (t = 120 min) the measured values stay constant, indicating a successful hybridization C: Schematic drawing, showing the stepwise attachment of first the DNA and second the CdSe dumbbells. Shown is the 5th overtone.

Single stranded DNA, modified with a thiol group at the 5′ end, binds to an activated gold surface (t = 9 - 28 min). The resulting change in frequency (Δf = -6 Hz) and dissipation ($\Delta D = 0{,}8 \cdot 10^{-6}$) are in good agreement with the literature [208]. They suggest the presence of multiple contacts between each ssDNA strand and the gold surface. The negatively charged backbone of the DNA is known to stick to hydrophobic surfaces. The thickness of the adsorbed was calculated after the Voigt model (crossref Intro QCM-D) to 2,1 nm. The

used DNA strand consits of 39 bases, resulting in an expected contour length of approximately 12 nm. The calculated height is more consistent with the average diameter of DNA (2,2 - 2,6 nm), supporting the observation that the DNA backbone interacts with the gold surface.

Even though the DNA is kind of lying on the surface, the strands are still active towards hybridization. Addition of CdSe dumbbells (t = 56 - 100 min), modified with the complementary DNA, results in a large change of frequency of –50 Hz. Also in dissipation the change is evident ($\Delta D = 11 \cdot 10^{-6}$). Calculating the thickness, results in a height of 16 nm for the attached nanocrystals. The here used NCs had a length of 40 nm and a diameter of 4 nm. Assuming, that there is only a monolayer forming, the particles seem to stand on the surface, tilted under a certain angle. Fitting the hybridization curve with an exponential fit, results in a time constant of 6,19 for the change in frequency (R^2 = 0,997) and 5,63 for the dissipation change (R^2 = 0,998). Repeating the experiments results in the same time constants.

The use of DNA as linker for the immobilization enables a more controlled attachment of inorganic NCs on a nanopatterned surface. The percentage of occupied dots is higher as in the case of the dithiol molecules. Also the distribution of attached particles per dot is smaller compared to working in toluene. To most of the dots two CdSe nanoparticles are connected. An alignment seems to be possible under flow conditions. The immobilization on the surface via DNA is also reversible. Adding a DNA strand, matching to one of the immobilized strands, results in the release of the nanoparticles from the surface.

The advantage of the coupling over dithiol molecules is, that no further modification of the particles is necessary. They can be attached directly after their synthesis. The growth of a gold domain to the NCs is mandatory in both cases.

4.3.4 Bridging of Gold Dots with Single Stranded DNA

Single stranded DNA can be synthesized in nearly any length. Even though DNA consists of only four nucleotides, a lot of information can be stored in a small molecule, as the nucleotides are freely variable. DNA consists of 4 different nucleotides, so that one nucleotide refers to 2 bit on a size of 0,33 nm.

Linking ssDNA between two or three anchor points on a surface is offering the possibility for further more complex functionalization of the surface by its pre defined sequence. It should be so possible to arrange different kind of nanocrystals in a controlled and programmable way on a surface. Gold nanoparticles on a surface can work as anchor points for the ssDNA (figure 52).

Two 5'-SH modified ssDNA strands with 20 bases matching towards the 3' end are hybridized and then added to the PEG passivated nanostructured surface. This results in a linkage with ssDNA over several hundred base pairs,

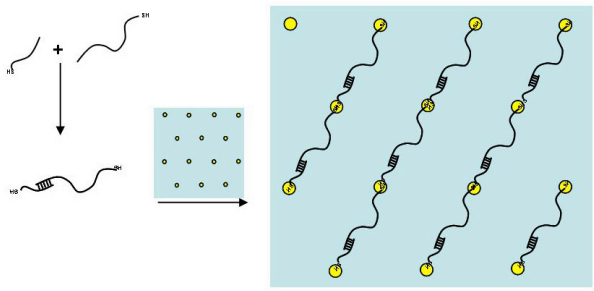

Figure 52: **Scheme for the attachment of ssDNA between gold dots on the surface.** A long ssDNA strand, with a thiol modification at the 5′ end, is first hybirdized with a short strand, also with a thiol group at the 5′ end. They overlap in 20 bases, resulting in a stable connection. The bifunctionalized ssDNA can bridge two gold dots.

which are now addressable for further modification. To bridge a distance of 60 nm we immobilized a DNA consisting of 178 nucleotides. 20 nucleotides are necessary for the stable connection with the second DNA strand; all the others stay freely accessible (figure 52).

With this setup, we were able to immobilize ssDNA between the gold dots on the surface, with a lateral distance of 60 nm (figure 53).

The gold dots on the surface, with a lateral distance of 60 nm, were obtained by dip coating a glass substrate in a PS 501-*b*-P2VP 231 polymer solution. The successful attachment of the DNA was followed by fluorescence microscopy. After staining the ssDNA with SYBR Green I, the fluorescence in the nanopatterned area of the substrates is detectable. The PEG passivated part on the surface (upper part in the fluorescence microscope image, figure 53A) refers as internal control. In the intensity profile goes along the grey line in the fluorescence image (figure 53B). It starts in the passivated area (position 1), where a background can be measured. Going towards the dipping line, a sharp increase in the intensity is visible (position 2). Going to the homogenously structured part of the surface (position 3), the fluorescence intensity decreases, compared to the dipping line, but is still higher, than the background. The peak in the intensity at the dipping line can be related to the higher density of gold dots in this area. Further analysis ha been carried out in the AFM (figure 53C). The measurements were performed under TE buffer. The ssDNA connects two gold dots on the surface, but every dot is connected to another via DNA.

Using ssDNA for the further structuring of nanopatterned substrates, enables the building of a programmable surface. Long DNA strands can bridge the gap between neighbouring particles on the surface. The 153 free nucleotides of the DNA offer specific binding sites for DNA modified nanoparticles. Assuming that a pairing over 12 bases results in a stable connection, 12 positions for a precise immobilization can be distinguished.

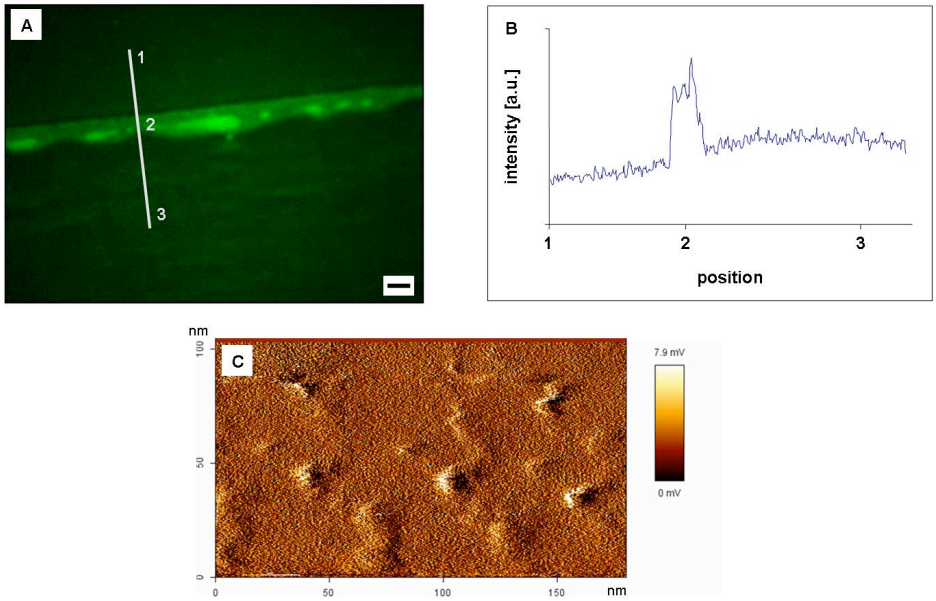

Figure 53: **ssDNA attached between gold nanodots on a PEG passivated glass slide. The interparticle distance of the gold dots is 60 nm.** A: Fluorescence microscopy image after staining the ssDNA with SYBR Green I; the scale bar corresponds to 1 μm. B: Intensity profile along the grey line in the fluorescence image (A) C: AFM image of ssDNA bridging the gold dots on the surface.

4.4 Micellar Nanolithography with Semiconducting Nanocrystals

For applications, in which the optical properties of e.g. CdSe particles are of main interest, the before described methods are not applicable. Growth of the gold domain influences the optical properties of the CdSe particles as the fluorescence is quenched by the gold.

For optical applications it is necessary to find a method to precisely position the particles on the surface without the need to grow gold domains on the particles. A combination of micellar nanolithography and inorganic nanocrystals offers a new way for the controlled immobilization, where it is not necessary to grow a gold domain on the particles. Experiences in the use of block copolymer micellar nanolithography can be combined with well established synthesis routs for the nanocrystals.

Several experimental processes and theoretical models have been developed for the incorporation of inorganic nanoparticles into polymeric nanostructure . *Gindy* et al. demonstrated pattern formation using mixtures of hydrophobic nanoparticles and block copolymers [209]. *Lin* et al. showed recently that the pattern of diblock copolymer domains in films could be influenced by nanoparticles [210]. By working with gold nanoparticles, *Chiu* et al. showed that they could be either found inside the block copolymer domains or at the interface of the two block copolymer domains [76]. Precise control of the deposition of the nanoparticles within block copolymer films is important for developing organized hybrid materials to obtain practical functionality [211].

So far, only the hydrophobic shell of block copolymers has been brought in contact with nanocrystals. The hydrophobic TOPO shell makes them stick to the polystyrene of an amphiphilic poly(styrene-b-vinylpyridine) block copolymer [211]. This results in the formation of a homogenous film of the quantum dots, which is interrupted by holes, coming from the vinylpyridine. For a selective positioning of single dots it is therefore far better to render the quantum dots hydrophilic so that they can interact with the vinyl pyridine in the core of the micelle (figure 54).

Exposure to excess of mercaptoethanol and mercaptopropionic acid results in the exchange of the TOPO shell around the CdSe particles. The Cd^{2+} ions are an attractive binding site for thiols. It is thus possible to generate hydrophilic CdSe dots, which can now be incorporated into micelles of the PS 2076-*b*-P2VP 571 block copolymer, as depicted in figure 54. The modified quantum dots are not stable in aqueous solution after treating them with mercaptoethanol and mercaptopropionic acid. Already after several hours they start to precipitate. Mixing the hydrophobic quantum dots with a micellar solution of the diblock copolymer, stabilizes the particles. The solution is stable for at least several weeks. Dip coating of substrates in a block copolymer quantum dot solution leads to a mono micellar film, where the quantum dots are hexagonally arranged on the surface (figure 55).

The interparticle distance between the quantum dots, as determined from the SEM images, is 117$\pm$34 nm (figure 55). This distance can be reached by

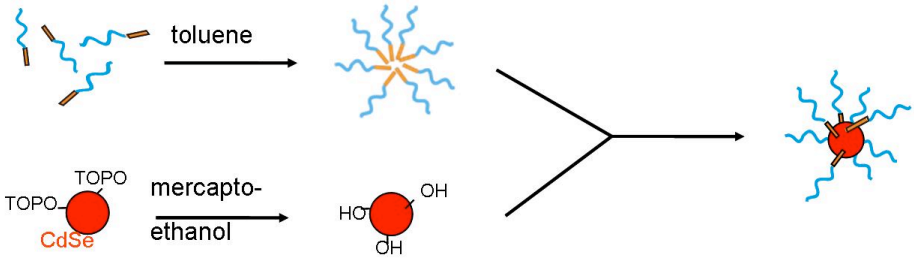

Figure 54: **Micellar Nanolithography with spherical CdSe dots (quantum dots).** TOPO coated CdSe dots are made hydrophilic by exposure to an excess of mercaptoethanol and mercapto propionic acid. They can now react with the hydrophilic core of the PS-*b*-P2VP micelles in a solution of toluene.

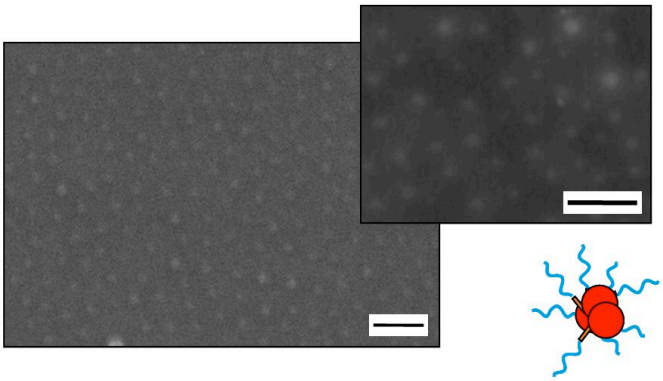

Figure 55: **SEM image of spherical CdSe particles, deposited on the surface by block copolymer micellar nanolithography.** The inlet shows a STEM image, where an inhomogeneous size distribution of the core of the micelles, occupied with the CdSe dots, is visible. The scale bars correspond to 200 nm.

working with PS 2076-*b*-P2VP 571. It is in accordance with the distance reached by working with metal salts as precursor, as described in part one of this thesis. STEM analysis (figure 55) shows, that each micelle is occupied by not only one quantum dot but by three or four. Working with smaller polymers may result in a lower number of dots per micelle. In the SEM the exact number of dots per micelle can not be distinguished. Also experiments with the smaller PS 501-*b*-P2VP 231 polymer did not give the exact number of CdSe dots per micelle. The interparticle distance here is 55±20 nm. But it seems that there is also more than one quantum dot inside one micelle.

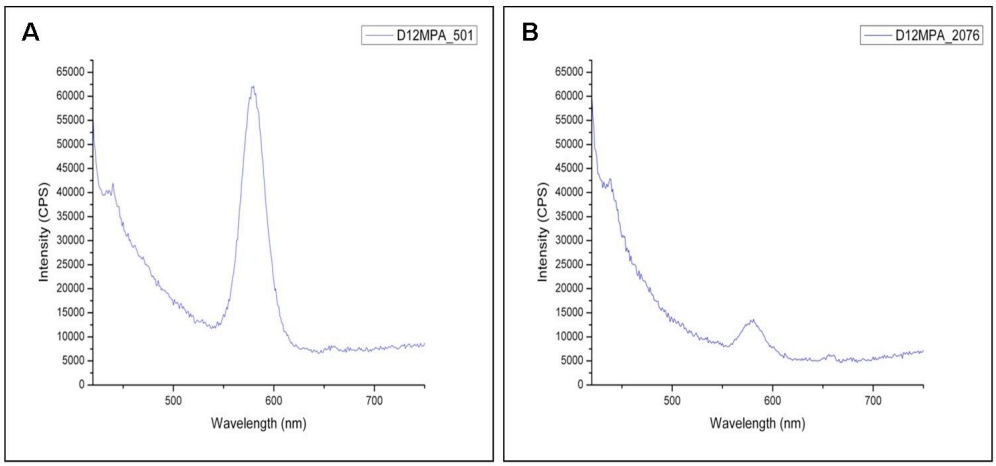

Figure 56: **Fluorescence of spherical CdSe particles immobilized on a glass slide via micellar nanolithography.** A: Pattern, obtained by working with PS 501-*b*-P2VP 231, B: PS 2076-*b*-P2VP 571

The fluorescence of the immobilized CdSe dots was also measured on the surface (figure 56). Working with PS 501-*b*-P2VP 231 yields higher fluorescence intensity (figure 56A) on the surface as working with the larger PS 2076-*b*-P2VP 571 block copolymer (figure 56B). This is in accordance with the number of dots on the surface. With the smaller interparticle spacing of the shorter polymer, the dots are deposited on the surface closer to each other than with the larger PS 2076-*b*-P2VP 571 polymer. The intensity of the fluorescence should be dependent on the density of the particles. Comparing the density of the particles with the fluorescence intensity gives rise to the relative number of dots inside the micelles.

To calculate the density of dots, a hexagonal order is assumed. The height h between three dots (figure 57) can be calculated according

$$h^2 = \frac{3}{4}a^2 \tag{14}$$

where a is the interparticle spacing. The surface area A inside this triangle is

$$A = \frac{1}{2}h \cdot a$$

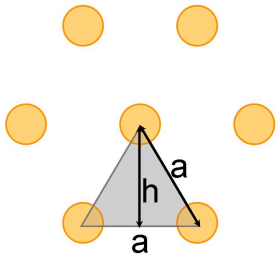

Figure 57: **Scheme for the calculation of the density of particles on the surface.** Assumed is a hexagonal arrangement of the particles on the surface.

. Each quantum dot is surrounded by six triangles, while one triangle contains three different quantum dots. Therefore each quantum dot occupies an effective surface area of $2A$. Taking this calculation into account, the density of the particles on the surface ρ can be calculated with the following equation:

$$\rho = \frac{2}{\sqrt{3} \cdot a^2} \tag{15}$$

The interparticle distance for particles, deposited with the PS 501-*b*-P2VP 231 polymer is 55 nm, while it is 117 nm when the particles are immobilized on the surface via PS 2076-*b*-P2VP 571. Calculating the areal density with these values results in a density of $\rho_{501} = 381,7$ particles / μm^2 for the PS 501-*b*-P2VP 231 and in case of the PS 2076-*b*-P2VP 571 of $\rho_{2076} = 81,4$ particles / μm^2. Thus, the density is 4,5 times higher by working with the smaller polymer. In the fluorescence spectrum the maximum intensity for the PS 501-*b*-P2VP 231 surface is at 62500 cps, while it is at 15000 cps in the other case. The intensity is 4,2 times higher for the smaller polymer, which is in accordance with the density calculation (table 3). It seems that working with these two different block copolymers does not change the number of quantum dots within one micelle.

Table 3: Relation between density of the particles and the fluorescence.

Polymer	Density	Fluorescence Intensity
501-*b*-231	381,7	625000
2076-*b*-571	81,4	15000
Ratio	4,5	4,2

We could show that it is possible to immobilize pre synthesized CdSe dots without any linker on a glass substrate in a defined pattern. This can be realized by combining the micellar approach with pre-synthesized nanoparticles. As the chemistry of nanoparticles is mainly dependent on the organic shell of the particles, this method should be also applicable for other colloidal NCs.

The number of CdSe dots per micelle might be tuned by working with even

smaller block copolymers. Working with a polymer, that would generate gold dots in the size of 4 nm with a metal precursor, could help to have only one quantum dot inside one micelle.

5 Growth of Particles on Substrates

One of the first studies of growing nanowires directly on a substrate was done already in 1964 by Wagner and Ellis [142]. They studied the growth of silicon whiskers in the gas phase and called it the vapor-liquid-solid (VLS) mechanism. figure 58 schematically shows the tip growth for 1-D material grown from nanoparticles on a substrate.

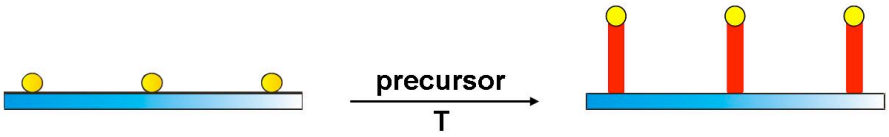

Figure 58: **Growth mechanisms for a VLS growth.** A nanopatterned substrate is heated to the reaction temperature and the precursor is added. Supersaturation inside the nanoparticles leads to the tip growth of a wire. The position of the resulting particles is controlled by the nanopatterning of the surface.

The substrate coated with nanoparticles is heated to the reaction temperature. The feed gas, containing the precursor for the growth, is then introduced into the reaction chamber. The molecules are split locally at the nanoparticles or thermally, if the temperature is high enough to dissociate the bonds. Nucleation between the nanoparticles and the precursor molecule results in an alloy of the nanoparticles, which, when supersaturated, leads to precipitation of the adsorbed material. Upon precipitation, the material crystallizes and forms a wire. Growth can occur with the nanoparticles seeded at the tip of the wire. The nanoparticles on the surface control the size and the position on the substrate [212]

Analogous to the well known VLS mechanism, also a solution-solid-liquid (SLS) growth of nanoparticles is possible. In the SLS approach the catalyst is a colloidal metal nanoparticles that is either injected into the solution together with the precursor molecules needed to grow the desired NCs, or is nucleated *in situ*. Each of these catalyst nanoparticles promotes unidirectional growth of NCs directly in the solution. Demonstrated examples are nanorods and wires of CdSe, InAs, InP, Si and Ge. So far it is not fully understood whether the catalyst particle (which should be in an almost molten state) becomes supersupersaturated with the precursor atoms, which then precipitate out forming a wire, or whether it simply offers a preferential site for the decomposition of the precursor molecule, followed by a rapid diffusion of the monomers along the surface of the catalyst, at which they coalesce and ultimately generate a wire. In principle, the SLS approach yields hybrid nanocrystalline materials, with the seed as tip at the end of the growing rod or wire.

A possible application for the substrates is to be found in the harvesting of solar energy, as the semiconductor nanowires are known to be efficient absorbers for light in the visible spectrum [25].

5.1 Growth of CdSe

Here, we present an approach to produce substrates with a wide array of long semiconductor nanowires protruding from it. The basis of the substrates is a flat surface patterned with gold dots with controlled diameter and controlled interparticle spacing, arranged in a quasi-hexagonal order, as described in the first part of this work. In a catalysed growth process we are able to use the gold dot particles as seeds for the growth of semiconductor nanowires with a length in the range between few tenth of nanometers and several micrometers. The process ensures that the wires form an epitaxial link with the gold dots and thus the underlying surface.

The process of wire growth involves two steps. First a catalyst for the growth of the wires has to be deposited and subsequently the wires are grown. This process is similar to a published recipe from the group of *W. E. Buhro* [109]. For the growth of the semiconductor nanowires the substrates with the bismuth covered gold particles are emerged into a solution of cadmium stearate in TOPO (tri-*n*-octylphosphine oxide) and the precursor for Se is injected into this growth solution. The temperature of solution needs to be set to 150-250° C for the process to occur. The final length of the wires can be controlled by the amount of Bi on the substrate and the reaction time. All growth experiments have been carried out with surfaces, dip coated in the PS 2076-*b*-P2VP 571 polymer.

5.1.1 Au@Bi Core Shell Particles

Even though it is possible to grow gold tips selectively to the end of CdSe nanorods, it is not possible to do it vice versa. For the growth of CdSe rods directly on a surface it is therefore required to grow a shell of a catalyst around the particles. As catalyst we are using bismuth [213]. The bismuth is deposited selectively onto the gold particles by emerging the substrates covered with gold dots into the growth solution containing (bistrimethylsilyl) amide $Bi[N(SiMe_3)_2]$. The size of the resulting core-shell particles is controlled by the reaction time. The growth of the particles can be followed by SEM analysis (figure 59 and figure 60).

Activating the nanopatterned silicon substrates for three minutes in the oxygen plasma (0,4 mbar, 150 W), results in the formation of gold clusters on the surface in a hexagonal arrangement. ImageJ analysis results in an interparticle distance of 111±18 nm and an order parameter ψ of 0,53 (figure 59A). The growth of the core-shell particles is not influencing the interparticle distance, also the order stays constant. After one hour in the reaction solution the interparticle distance has been measured to 124±22 nm, while the order parameter ψ slightly decreases ($\psi = 0,45$, figure 59B). Even longer reaction times are not influencing the distance or the order. After two hours, the distance is 106±21 nm ($\psi = 0,43$) (figure 59C), and after 4 h the distance between the particles is 105±23 nm ($\psi = 0,43$) (figure 59D). Leaving the nanopatterned substrates

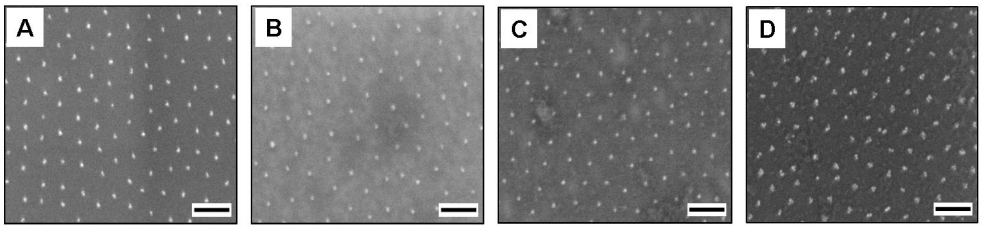

Figure 59: **SEM images of substrates after growth of bismuth over different times; all samples have been activated in oxygen plasma for 3 minutes at 150 W and a pressure of 0,4 mbar.** A: reference, silicon substrate dip coated inside a PS 2076-*b*-P2VP 571 solution and plasma activated; B: one hour of growth; C. after two hours of growth; D: after four hours of growth. The scale bars correspond to 200nm. The growth of the Bi shell can be followed by analyzing the diameter of the particles. The interparticle distance as well as the order parameter are not changing during the reaction.

for longer than three hours in the reaction solution results in the formation of multidots (figure 59D).

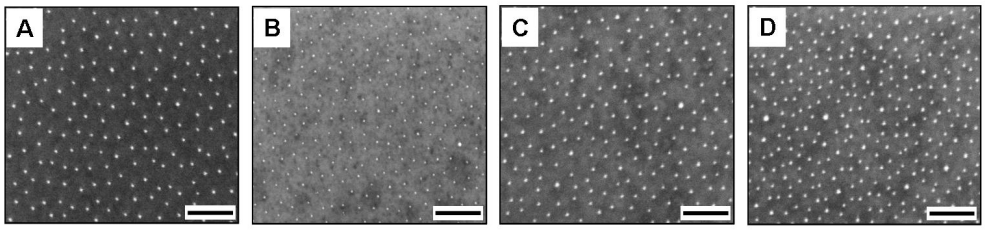

Figure 60: **SEM images of substrates after growth of bismuth over different times; all samples have been activated in hydrogen plasma for 45 minutes at 150 W and a pressure of 0,4 mbar.** A: reference, silicon substrate dip coated inside a PS 2076-b-P2VP 571 solution and plasma treated; B: one hour of growth; C. after two hours of growth; D: after four hours of growth; scale bars correspond to 200nm. The growth of the Bi shell can be followed by analyzing the diameter of the particles. The interparticle distance as well as the order parameter are not changing during the reaction.

Substrates, containing nanodots without polymer shell, were put inside the reaction solution for different times. The growth of the particles can be followed in the SEM (figure 60). Also here the interparticle distance as well as the order parameter has been determined by ImageJ analysis. The interparticle distance of the reference is 108$\pm$18 nm and the order parameter ψ is 0,46 (figure 60A). During the growth process the distance as well as the orderparameter is not affected. The interparticle distance was measured to be 106$\pm$19

nm ($\psi = 0,46$, figure 60B) after one hour, 102±17 nm ($\psi = 0,47$, figure 60C) after two hours, and 104±20 nm ($\psi = 0,46$, figure 60D) after four hours.

After four hours in the reaction solution the size of the particles was not as homogenous as before, but no multidots can be detected after the four hours. The order parameter did not change significantly over the reaction time. In case of the intramicellar growth (figure 60) this can be explained by a stabilizing effect through the micelles. They keep the particles in their position. If the samples are treated 45 minutes in the hydrogen plasma, as in the second case, the polymer from the micelles is completely removed. Nevertheless, the particles are not moving during the growth process. This is due to the oxide layer on top of the silicon substrate. The gold dots sink inside this layer, which is then avoiding the movement of the gold particles on the surface.

To follow the formation of the core shall particles more in detail, the diameter of the particles in the SEM images have been analyzed with MatLab [14].

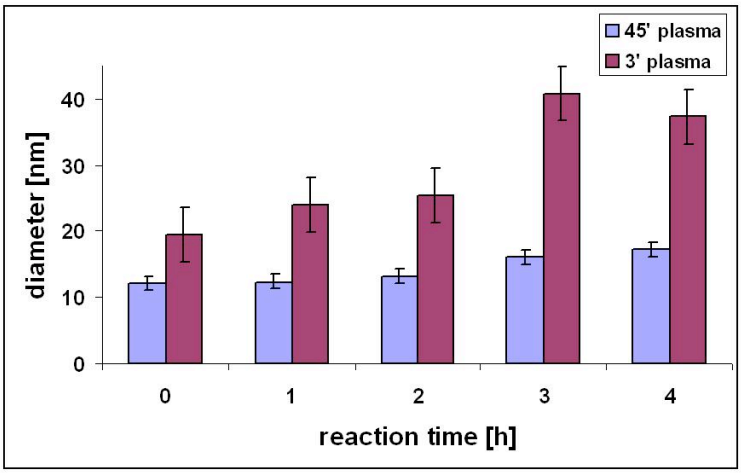

Figure 61: **Growth of the particles on the surface, due to the formation of a bismuth shell around the gold.** Compared is an intramicellar growth mechanism (3 min. plasma treatment) with one around preformed gold dots (45 min plasma treatment).

The diameter of the gold dots, which are only activated in short oxygen plasma treatment is larger then after the treatment for 45 minutes in the hydrogen plasma (figure 61). For both methods the growth of the bismuth shell becomes obvious, as the diameter of the particles is increasing. After dipping a silicon substrate in a PS 2076-*b*-P2VP 571 solution and activating it for three minutes in the oxygen plasma, the diameter of the particles is 19,4 nm (figure 61, pink columns). The diameter increases with the reaction time over 24,0 nm after one hour, over 25,4 nm after two hours, to 40,8 nm after three hours. Longer reaction times are not resulting in a further increase of the particle size.

[14] Kindly programmed by H. Boehm from the group of Prof. J. P. Spatz, MPI for metals research, Stuttgart, Germany.

After four hours in the reaction solution the size of the particles was at 37,7 nm. Obviously saturation is reached after three hours. The same effects can be observed for the hydrogen plasma treated substrates (figure 61, blue columns). The gold particles themselves have a diameter of 12,0 nm. It is growing with the reaction time over 12,3 nm after one hour, over 13,1 nm after two hours, to 16,0 nm after three hours. In contrast to the previous case saturation is nor yet reached after three hours, as the diameter is increasing to 17,2 nm after four hours in the reaction solution. It is obviously possible to obtain

The difficulty in the determination of the particle size is the formation of multidots. The program partly notes them as single particles, partly divides them into several small ones. Calculating the diameter of the particles is thus not the best method to see if there is saturation. A too low concentration of the bismuth precursor could also be the reason for a stop in the growth process.

For a more detailed analysis of the growth, the substrates have been measured by XPS (figure 62). After growth of the bismuth shell for one (figure 62, blue line), two (figure 62, red line), and four hours (figure 62, green line) the substrates have been analyzed.

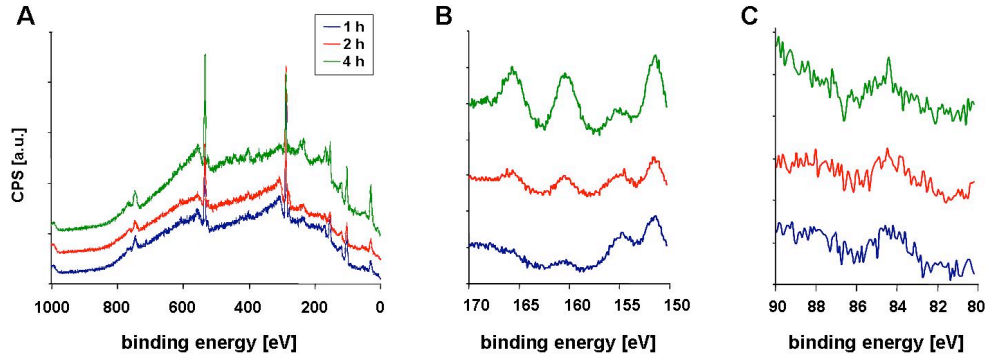

Figure 62: **XPS of Au@Bi core shell particles after growth of the shell for one (blue line), two (red line) and four hours(green line).** A: Survey. B: The bi 4f signal is increasing with the reaction time. C: Differences in the Au 4f intensity are hardly to be distinguished

Shown are the survey (figure 62A), the Bi 4f signal (figure 62B) and the Au 4f signal (figure 62C). For bismuth the $4f_{7/2}$ line can be found at a binding energy of 157,0 eV. 5,31 eV apart from it, the $4f_{5/2}$ signal appears at higher binding energy, but usually with lower intensity. The spectra of the core shell particles show a signal at 160,0 and 165,5 eV. The shift of 3 eV denotes the presence of bismuth oxide instead of elementary bismuth. The intensity of both Bi 4f signals is increasing over the reaction time. The gold $4f_{7/2}$ peak at 84,2 eV is hardly detectable. For the Au $4f_{5/2}$ electrons, the peak should be at 3,7 eV shifted. This peak can not be detected, as the signal to noise ratio is not high enough to determine the signal from the background.

As the absolute intensities of the measurements cannot be compared with

each other, we normalized them to silicon. The silicon signal from the surface is always detected, also in an intensity scan (Table 1).

Table 4: Comparison of XPS Intensities.

Reaction time	I_{Bi}/I_{Si}	I_{Si}/I_{Au}
1h	16,5	2,3
2h	6,3	3,9
4h	3,0	17,2

As expected, the relation of the intensities between bismuth and silicon (I_{Bi}/I_{Si}) is decreasing. More bismuth is deposited on the surface over the time. The relation between the silicon and the gold intensity is increasing. The increase shows that either the gold is washed away during the reaction, which is quite unlikely. A more reasonable explanation is the formation of a layer on top of the gold. This layer is increasing over the reaction time, cushioning the signal of the gold. Especially after four hours the ratio between gold and silicon is very high. The gold seems to be covered by a dens layer of metal, where the X-rays can not come through.

5.1.2 CdSe Rods and Wires

The as prepared Au@Bi core-shell nanopatterned surfaces are used for the growth of CdSe wires directly on the surface. As bismuth is supposed to catalyze the growth of the wires, surfaces with different particle sizes have been used for growing them. As there was a difference in the formation of the core-shell particles depending on the plasma conditions, both methods are tested also for the growth of CdSe rods and wires. In oxygen plasma shortly activated substrates with different amounts of bismuth are used for the growth of CdSe rods and wires under the same growth conditions (figure 63).

The used surfaces, containing the core-shell particles, have been equally prepared as the ones in figure 59. The difference in the growth of the CdSe is clearly visible in the SEM (figure 63). Having only small amounts of bismuth on the surface is lading to an inhomogeneous growth of the particles. CdSe might be fusing inside or forming a further shell, but there is no anisotropic growth observable (figure 63A). With increasing size of the bismuth particles, the CdSe starts forming rods and wires. They first are pretty short and seem to be curled around the dots (figure 63B). Also they appear not homogenously on the surface. If the bismuth particles are allowed to form over three hours, defined rods are formed. They are homogenously spread over the surface, even though not every gold dot is connected with a CdSe rod. Their length is between 200 nm and 1 μm (figure 63C). Working with substrates, which have been for four hours in the reaction solution, the growth is even enhanced (figure 63D). The formed CdSe wires are growing over several micrometers. The growth is homogenous all over the surface.

Even if the average diameter of the core-shell particles on the surfaces after

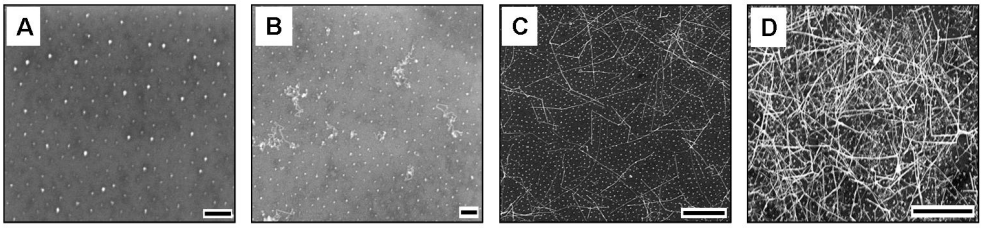

Figure 63: **SEM images after growing CdSe on substrates containing different amounts of bismuth.** The core shell particles were grown in an intramicellar approach. The CdSe growth conditions were the sam efor all. A: 1 hour growth of Bi followed by CdSe growth; B: 2 hours growth of Bi shell followed by CdSe growth; C: 3 hours growth of Bi shell followed by CdSe growth; D: 4 hours growth of Bi shell followed by CdSe growth. The scale bars in A and B correspond to 200 nm, in C and D to 1 μm.

four hours of bismuth growth was less than compared to the ones after three hours in the reaction solution, they obviously contain more bismuth. In the non dipped area, there are no CdSe wires. The bismuth in the surface is not working as catalyst for the growth in solution. The particles are selectively growing on them.

The same experiment has been carried out with substrates, where the micellar film has been completely removed after dip-coating. The growth conditions of the CdSe have been the same as before. In the SEM one can clearly see that there is a difference in the two cases (figure 64).

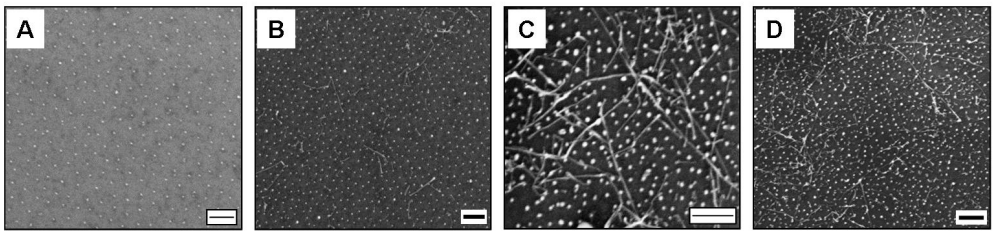

Figure 64: **SEM images after growing CdSe on substrates containing different amounts of bismuth.** The core shell particles were grown after a complete plasma removal of the diblock copolymer. The CdSe growth conditions were equal for all. A: 1 hour growth of Bi followed by CdSe growth; B: 2 hours growth of Bi shell followed by CdSe growth; C: 3 hours growth of Bi shell followed by CdSe growth; D: 4 hours growth of Bi shell followed by CdSe growth. The scale bars in A and B correspond to 200 nm, in C and D to 1 μm.

Having only a small shell of bismuth around the gold particles, there was no change in the surface observable (figure 64A). The surface looks the same as

before the growth (Figure 3B). With increasing particle size also the growth of CdSe is promoted. After growing bismuth for two hours, there are sever CdSe rods on the surface (figure 64B). Their length is between 200 and 500 nm. The length of the rods is again increasing on the next substrate (figure 64C). Here the bismuth was allowed to grow for three hours. The wires have a length in the micrometer range; also some rods can be found with a length of 100 to 200 nm. The diameter of the dots on the surface is increased. Probably also here CdSe has fused inside the particles or has formed a further shell around them. Leaving the substrates longer in the bismuth reaction solution is not enhancing further growth of CdSe wires (figure 64D). The growth here even seems to be reduced. The length of the wires is in the range of 300 to 700 nm, and they are homogenously distributed over the surface.

But not only should the amount of bismuth play an important role on the growth of the wires on the surface, also the reaction time of the CdSe. Working with the same bismuth particle size but changing the reaction time of the CdSe growth should lead to different modified substrates.

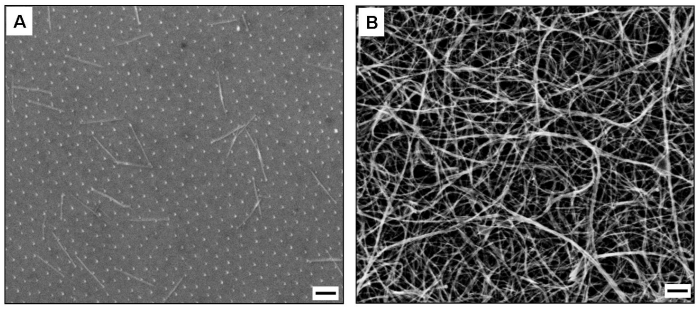

Figure 65: **SE micrographs of CdSe wires, grown on substrates with the same Bi content, but varying the the reaction time of the CdSe.** A: 3 min. B: 9 min. reaction time in solution. The scale bars correspond to 200 nm.

Growing CdSe wires over a time of three minutes on a bismuth modified surface (two hours growth of bismuth) results in a formation of CdSe rods with a length of 400 to 800 nm (figure 65A). Every rod is connected to a dot on the surface. Leaving the same kind of surface for nine minutes in the CdSe reaction solution is resulting in the formation of long wires (figure 65B). It is impossible to determine the length of the single wires . There are junctions between several wires, making it impossible to measure the length of a single wire.

Going to a position where the ends of the wires can be seen, there are light spots on the end of each wire (figure 66A). As there CdSe wires are very dense on the surface, it is hard to distinguish if every rod has this tip at the end. At the dipping edge it is possible to look on the end of single wires (figure 66B). The wires are growing from the patterned area. Few of them end in the non-dipped area, so that they can be analyzed in the SEM in more detail.

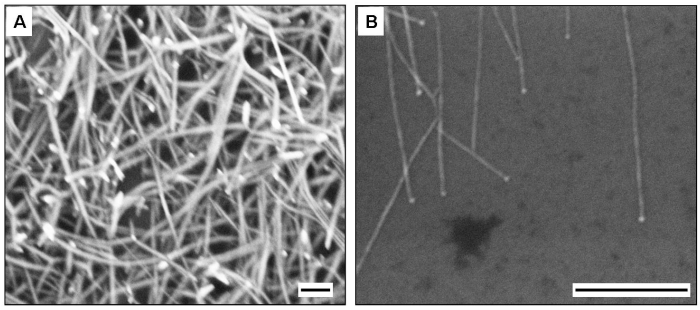

Figure 66: **SEM image of CdSe wires.** A: The white tips at the free ends of the wires indicate a tip growth. B: The free ends of the CdSe wires are probably decorated with a Bi tip. The scale bars correspond to 200 nm.

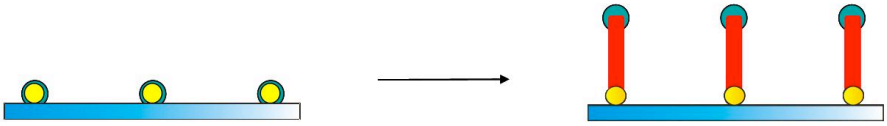

Figure 67: **Assumed growth of CdSe wires on Au@Bi core shell particles.** The cadmium as well as the selenium fuse through the bismuth but can not enter the gold nanoparticles itself. The CdSe wire finally growth between the gold and the bismuth.

The tips at the free ends of the wires are indicating that the growth takes place between the gold core and the bismuth shell of the particles. The dots on the surface can still be visualized in some spots on the surface, where the growth of the wires is not too dense. We assume a growth mechanism, where the cadmium and the selenium fuse through the bismuth but can not enter the gold. The wire is thus growing between the bismuth and the gold. While the gold particle stays on the surface, the bismuth is at the tip of the growing wire (figure 67).

The amount of bismuth obviously has an effect on the growth of CdSe wires on the surface. It is enhancing the growth. All rods and wires grown on the surface are in the range of 200 nm up to several μm.

5.2 Growth of Co on Pt Nanostructured Substrates

Also the growth of Co on a gold nanopatterned surface is not possible. A metal, where an epitaxial growth of cobalt should be possible is platinum. As it is possible to get nanostructured surfaces with platinum nanodots, we are using these substrates for the growth of cobalt rods directly on the growth.

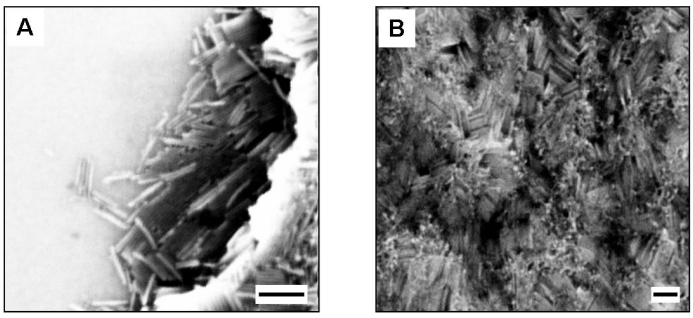

Figure 68: **SEM images of cobalt (Co) rods on platinum nanodots, obtained by dipcoating a silicon substrate in a PS 1056-*b*-P2VP [H_2PtCl_6]$_{0,5}$ 495 solution.** A: Co particles only occur on the nanopatterned substrate. B: A multilayer of Co rods homogenously covers the surface. The scale bars correspond to 100 nm.

The platinum nanopatterned substrates were obtained by working with PS 1056-*b*-P2VP 495 with a loading of platinum of 0,5. Under standard synthesis conditions the nanopatterned surface is covered with cobalt rods (figure 68B). There are several layers of the particles above each other. But on the dipping line it becomes obvious that the growth is dependent on the platinum nanoparticles. On the non-dipped part of the substrate there are hardly any cobalt rods (figure 68A). The multilayer of the rods is eve resistant to ultrasound application. Some of the dots have a light spot on top, which could be platinum. But as there are too many particles on the substrate it is impossible to draw conclusions from these images to the growth mechanism. Also here we assume an influence of the reaction conditions on the growth of the substrates.

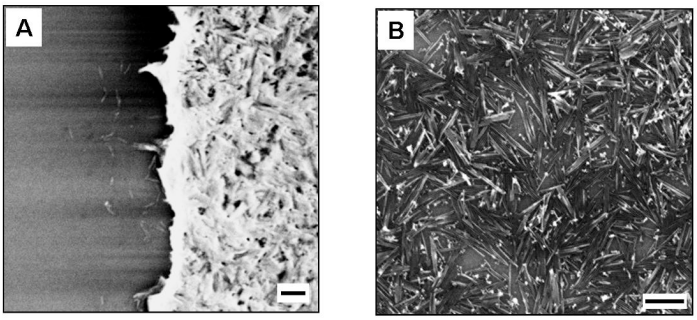

Figure 69: **SEM images of cobalt (Co) rods on platinum nanodots, obtained by dipcoating a silicon substrate in a PS 1056-*b*-P2VP $[H_2PtCl_6]_{0,5}$ 495 solution.** The concentration of the Co precursor is 5 times higher than in the previous case. A: Co particles only occur on the nanopatterned substrate. B: The surface is homogenously covered by a layer of particles. The light tips at their ends, indicating a growth on the Pt particles. The scale bars correspond to 200 nm.

Increasing the concentration of the cobalt precursor five times, results in particles with a length of 300 nm (figure 69B). The particles are growing only in the nanopatterned area. In the dipping edge, where the density of the platinum is higher compared to the rest of the surface, a multilayer of cobalt rods occurred (figure 69A). In the non dipped area there were hardly any particles found. The cobalt rods on the surface have again light spots at their end, indicating the growth out of the platinum on the surface. As the rods are lying on the surface, it is also here impossible to decide, which of the two growth mechanisms can be assumed.

An epitaxial growth mechanism of cobalt on platinum nanopatterned surfaces can be assumed. The control of the reaction conditions is very complex. The cobalt precursor needs high temperature for the decomposition. Reaction temperatures of 70 ° C did not result in any growth of cobalt particles, neither in solution nor on the surface, even after 48 hours reaction time.

The nanopatterned substrates prepared by micellar nanolithography are a good platform for the seeded growth of inorganic nanocrystals. As the particles on the surface can be made out of several material, it is applicable for different materials. By tuning the interparticle distance it is also possible to influence the lateral distance between the rods and wires. As they are growing directly on the surface, neither a modifaction of the particles nor a linker is required.

6 Viral Nanoparticles as Building Blocks

Although plant viral capsids have been extensively studied and utilized in nanotechnology, only few studies are about their immobilization on surfaces. Bi-and trilayer assemblies of cowpea mosaic virions (CPMV), labeled with two different ligands, biotin and a fluorescent dye, have been successfully demonstrated in solution.

6.1 CPMV Layers on Supported Lipid Bilayers

Functionalization of the virion allows the bottom-up assembly of arrays via layer-by-layer approach on a surface. Therefore various modifications of CPMV particles have been investigated by *N. Steinmetz* et al. [182]. In collaboration, we employed multilayers of biotin modified CPMV particles, cross linked via streptavidin by quartz crystal microbalance with dissipation monitoring (QCM-D). The here used virus particles were coated with two different densities of biotin molecules and that were attached over shorter and longer linkers (figure 70).

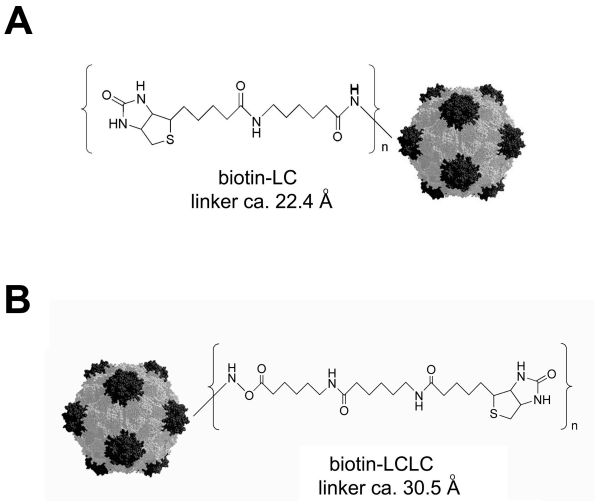

Figure 70: **Schema of cowpea mosaic virus (CPMV) particles decorated with biotin.** A: CPMV-(LCLC-bio): biotin, attached over a short (LC) linker, with a length of 2,24 nm; B: CPMV-(LCLC-bio): biotin, attached over a long (LCLC) linker, with a length of 3,05 nm. The CPMV is shown in grey and black, distinguishing the subunits on the protein coat, from [183].

CPMV viral nanoparticles (VNPs) are decorated with NHS-activated biotin molecules. Exterior lysines on the protein coat of the CPMV have been modified either with biotin-LC-N-hydrosuccinimide (LC-bio) or biotin LCLC-N-hydrosuccinimide (LCLC-bio). The LC-linker results in a spacing of 2,24 nm, while the LCLC linker separates the biotin from the virion about 3,05 nm. The

CPMV was either fully (F) decorated, with up to 240 lysines modified with biotin, or partly (P) modified with biotin (30 - 40 biotins on the virion surface). The formation of a bilayer of CPMV connected over SAv has been followed in situ by QCM-D measurements (figure 71).

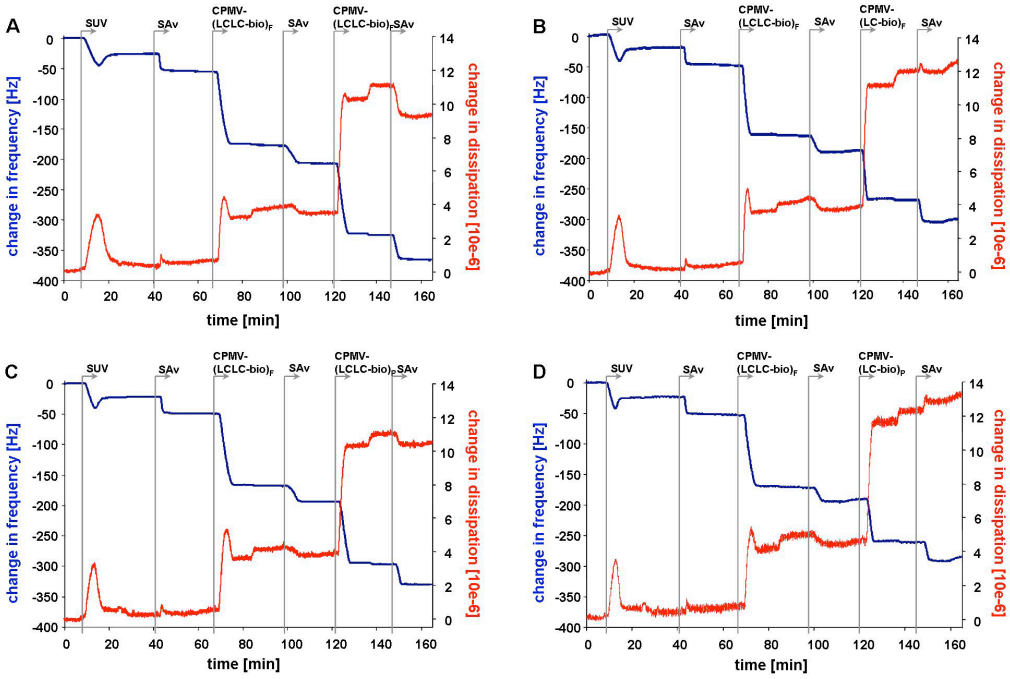

Figure 71: **Building of arrays consisting of alternating biotinylated CPMV particles and SAv on biotin doped supported bilayers (SLBs), as followed by QCM-D.** The CPMV particles have a different density in biotin labelling, as well as different spacer lengths. A: CPMV-(LCLC-bio)$_F$, B: CPMV-(LC-bio)$_F$, C: CPMV-(LCLC-bio)$_P$, D: CPMV-(LCLC-bio)$_P$, bio = biotin, LCLC = long spacer (3,05 nm), LC = short spacer (2,24 nm), F = fully decorated with biotin (about 240 biotin molecules attached), P = partly decorated (with 30 – 40 biotin molecules). Shown is the 5th overtone.

Hydrophilic silica surfaces have been functionalized with a biotin doped supported lipid bilayer (SLB). Alternating layers of differently biotin modified CPMV and SAv are build, followed by QCM-D measurements. In the first case, we used fully decorated CPMV, where the biotin is separated over the long spacer (CPMV-(LCLC-bio)$_F$, figure 71A). The formation of a supported lipid bilayer (SLB) from vesicles (t = 9 - 32 min), developed by *Richter* et al., shows the characteristic two-phase behavior [214]. In a first step, the vesicles adsorb on the surface. If a critical concentration is reached (peak at t = 13 min), they start spreading, forming a bilayer on the surface. The changes in frequency (-25 Hz) as well as in dissipation ($<0{,}5 \cdot 10^{-6}$) confirm the formation of a SLB in good quality. The surface of the resulting bilayer is doped with biotin. The biotin is randomly distributed in the bilayer. Adding SAv to the bilayer (t = 43 -

58 min) results in as additional shift in frequency of -29 Hz and small changes in dissipation, which is in good agreement with previous reports about the formation of a dense monolayer of SAv. The frequency change of -29 Hz corresponds to a mass uptake of 510 ng/cm^2. This indicates, that around 60 % of the film consists of water, as previously published results claim a dried mass of 200 ng/cm^2 for a monolayer of SAv.

The resulting SAv monolayer is now used for the attachment of a second CPMV layer (t = 69 - 83 min). The frequency decreases about -121 Hz. Together with a small shift in dissipation of $3{,}1 \cdot 10^{-6}$ the formation of a fairly rigid layer of the NPs can be assumed, where the particles are irreversibly bound, as no change in frequency can be observed during rinsing. The slight changes at 83 as well as at 136 min arise from the change in the buffer.

The decrease in frequency of -121 Hz is in agreement with a mass uptake of 2150 ng/cm^2. The expected mass, calculated by a random sequential adsorption model, is only 730 ng/cm^2. The higher value of the measurement indicates a strong hydration also of the virion layer. The deposition of another layer of SAv (t = 100 - 113 min) results in the same change of frequency (-29 Hz) as in the first layer. In contrast, the change in dissipation is slightly negative ($0{,}2 \cdot 10^{-6}$), indicating a stiffning of the second layer. The multivalent SAv molecules can cross link neighboring CPMV particles, as many biotins are exposed on the surface of the particles.

A second layer of CPMV (t = 123 - 136 min) and a third layer of SAv (t = 149 - 159) are added on top of the existing layer, to see if it is possible to build up several layers of them. The thickness of the second CPMV layer is comparable to the first one, as the change in frequency is very similar (Δf = -119 Hz). But there must be differences in the binding mode, as there is no peak observed and the change in dissipation is larger ($\Delta D = 7{,}7 \cdot 10^{-6}$). An additional last layer of SAv was added on top, resulting in a change in frequency of Δf = -40 Hz. This is a much larger value than in the two previous SAv layers, which can be explained by a much higher roughness of the surface, due to the CPMV. The decrease in dissipation ($\Delta D = -1{,}8 \cdot 10^{-6}$) is due to the cross linking of the VNPs with each other over SAv.

To explore the influence of the spacer length as well as the biotin density on the surface, the above described experiment was repeated with CPMV with lower biotin densities (CPMV-(LCLC-bio)$_P$, figure 71C), and with a shorter spacer (CPMV-(LC-bio)$_F$, figure 71B and CPMV-(LC-bio)$_P$, figure 71D).

The formation of the supported lipid bilayer as well as the attachment of the SAv layer is the same in all cases (figure 71A). The changes in frequency as well as in dissipation are nearly the same for all. The differences were less than 0,5 Hz and $0{,}1 \cdot 10^{-6}$, demonstrating the reproducibility of the experiments. The values for all measurements are summed up in Table 1. The changes in frequency for the formation of the first CPMV layer do not show significant differences, indicating the formation of a dense monolayer of VNPs on the surface. Differences can be found in the dissipation monitoring. They range between 3,1 and $4{,}1 \cdot 10^{-6}$ and are larger for lower biotin densities. A possi-

Table 5: Responses in frequency and dissipation in the formation of alternating SAv and CPMV layers, measured in QCM-D.

	(LCLC-bio)$_F$*		(LC-bio)$_F$*	
	Δf [Hz]	ΔD [10^{-6}]	Δf [Hz]	ΔD [10^{-6}]
1st SAv layer	-29	0,2	-29	0,2
1st CPMV layer	-121	3,1	-114	3,6
2nd SAv layer	-29	-0,4	-26	-0,6
2nd CPMV layer	-119	7,7	-82	8,2
3rd SAV layer	-40	-1,8	-37	-0,0

	(LCLC-bio)$_P$*		(LC-bio)$_P$*	
	Δf [Hz]	ΔD [10^{-6}]	Δf [Hz]	ΔD [10^{-6}]
1st SAv layer	-29	0,2	-29	0,2
1st CPMV layer	-118	3,6	-118	4,1
2nd SAv layer	-26	-0,4	-22	-0,5
2nd CPMV layer	-103	7,0	-70	7,5
3rd SAV layer	-34	-0,7	-30	0,5

*LCLC = long linker, LC = short linker, F = fully decorated, P = partially decorated

ble explanation is that these VNPs can bind with less biotin molecules to the SAv, resulting in a higher flexibility of the system and thus in an increase of the dissipation. Depositing a layer of SAv on the CPMV results in changes in the frequency ranging from -22 to -29 Hz. As expected, less binding occurs for lower biotin densities on the surface of the particles. But also the short linker results in a lower change in frequency. Probably not all VNPs biotinylated over the short spacer can be fully covered with SAv. Nevertheless, the negative shift in dissipation indicates that the VNPs are crosslinked with each other through the SAv. Major variations in Δf and ΔD between the differing VNPs occur in the deposition of the second CPMV layer. The frequency changes in a range between -70 Hz for the partly biotin decorated particle with the short spacer and -119 Hz for the long spacer and full biotin coverage. These alterations can be explained by the roughness in the formation of the first SAv layer, strongly affecting the ability of CPMV with short spacers and low biotin coverage to bind. The amount of SAv, deposited on top of the second CPMV layer, is in accordance with the observations for that layer. The frequency changes most for the long spacer and the high biotin concentration (Δf = -40 Hz) and least for the short spacer and the low biotin concentration (Δf = -30 Hz). Additionally the dissipation varies from $0{,}5 \cdot 10^{-6}$ to $-1{,}8 \cdot 10^{-6}$, being positive for short spacer and low biotin coverage, and negative for the long spacer and full coverage with biotin. At lower CPMV coverage, a full crosslinking might not be possible due to steric reasons. For the other cases, the measurements support the previous assumption, that crosslinking through SAv of neighboring CPMV results in a decrease of dissipation.

Varying the roughness of the surface can influence the interaction of CPMV

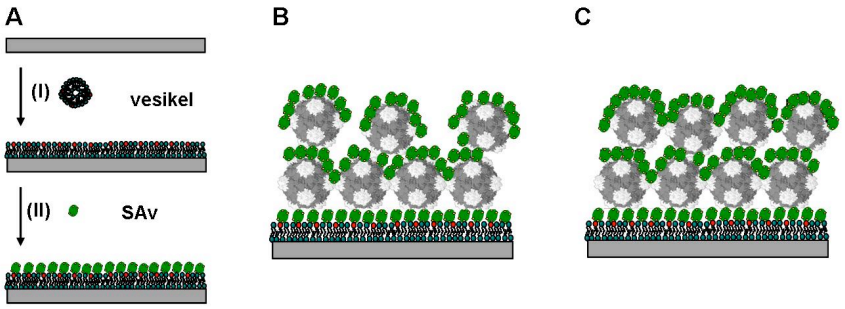

Figure 72: **Schematic presentation of arrays of biotinylated cowpea mosaic virus (CPMV) particles and streptavidin (SAv) formed on a biotin-doped supported lipid bilayer.** The CPMV is shown in grey, distinguishing the subunits on the protein coat. A: Formation of the supported lipid bilayer out of vesikles. B: Array, consisting of CPMV-(LC-bio)P and SAv; C: Array consisting of CPMV-(LCLC-bio)F and SAv. LC = short linker, LCLC = long linker, P = partially decorated, F = fully decorated with biotin. (B and C adopted from [183]).

with SAv covered surfaces. The biotin density as well as the spacer length has to be taken into account to build an array with layer-independent particle densities (figure 72B, C). Using a high density of biotin and a long spacer forms the most regular arrays (figure 72C).

6.2 CPMV Layer on Gold

To avoid the necessity of an additional layer, a method for the direct attachment of the virions to a surface was investigated. A controlled assembly of unmodified CPMV is not possible, as they aggregate on the surface, forming inhomogenous layers. As biotin modified CPMVs are stable in solution, we investigated a method for the attachment of SAv on gold. As SAv itself is not binding to the gold nanopattern, we introduced thiol groups to the protein according to standard protein modification procedure with Traut's reagent (figure 73). The cyclic iminothiolane reacts in a ring opening reaction with primary amines on the surface of the protein, leading to free accessible thiol groups.

The successful reaction can be followed by measuring the number of the introduced thiol groups. These number was determined by working with a thiol determination kit. The method relies on the activation of a protein via the free thiol groups. This protein is then determined by an encymatic recognition, resulting in a fluorescent molecule. The intensity and thus the concentration of thiol groups is determined at 410 nm. The sensitivity of this essay is about 25 times higher than the one of a standard Ellman's assay [215], due to the enzymatic amplification.

Knowing the concentration of the SAv it is possible to calculate the num-

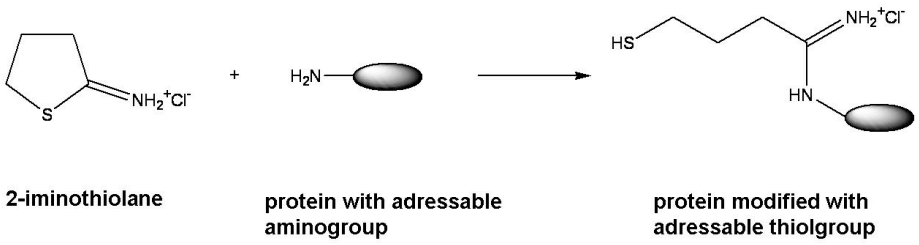

Figure 73: **Modification of proteins with 2-iminothiolane (Traut's Reagent).** The cyclic iminothiolane reacts in an ring opening mechanism with primary amines in a protein, resulting in a free thiol group on the outside of the protein.

ber of thiols on the modified protein. A non-modified SAv is used as control. Native streptavidin is a tetrameric protein with a molecular weight of 53 kDa. Each monomer consists out of 159 amino acids and is addressable by one biotin. The amino acid sequence reveals 9 lysine residues in each monomer. As the lysines consist of amino groups, these can easily be addressed by the iminothiolane. If every lysine reacts with Traut's reagent one can reach a maximum number of 32 thiol groups.

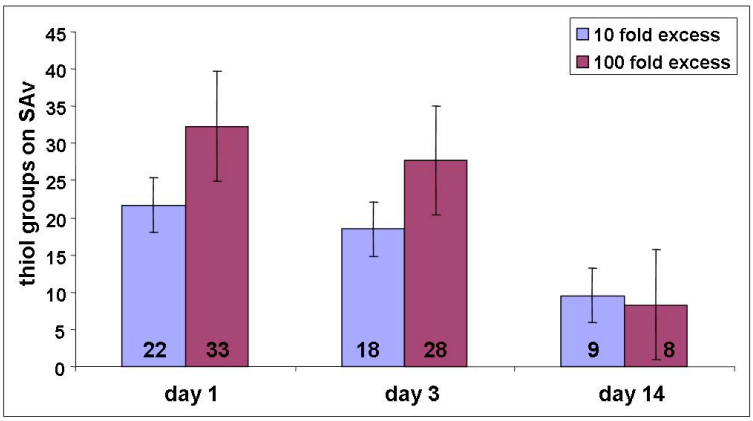

Figure 74: **Number of thiol groups on SAv, introduced with Traut's reagent.** The excess of added Traut's reagent influences the amount of inserted thiol groups. Measuring the thiol concentration over a period of two weeks shows a decrease in the number of free thiol residues. Thus leading to the conclusion that disulfide bridges are formed.

Working with a 100-fold excess of the iminothiolane introduced an average number of 33 thiol moieties, whereas with a 10-fold excess 22 thiols are detected (figure 74). This result indicates that the higher excess of iminothiolane addresses all lysines present in the amino acid sequence. Already after two days a decrease in the concentration of the thiol groups is detectable. This effect becomes more obvious after two weeks; where only 9 thiol groups are

detectable in the case of a 100-fold excess of iminothiolane and 8 for 10-fold excess. This can be explained by an oxidation reaction of thiols, where they form dithiol bridges. This oxidation might occur intramolecular or intermolecular. The former case still allows an attachment on the surface. But the molecular structure of the protein is changed, which could have an effect in the biotin binding properties of the SAv. Biotin molecules might not bind to the SAv any longer, or the binding kinetics might be influenced by structural changes in the structure during the modification. A reaction of the molecules with each other leads to formation of clusters of two or more proteins. As a consequence it is necessary to freshly modify the protein before it is immobilized on a gold surface.

The successful attachment of the thiolated SAv (HS-SAv) to PEG passivated gold nanopatterned surfaces were observed in a fluorescence microscope (figure 75).

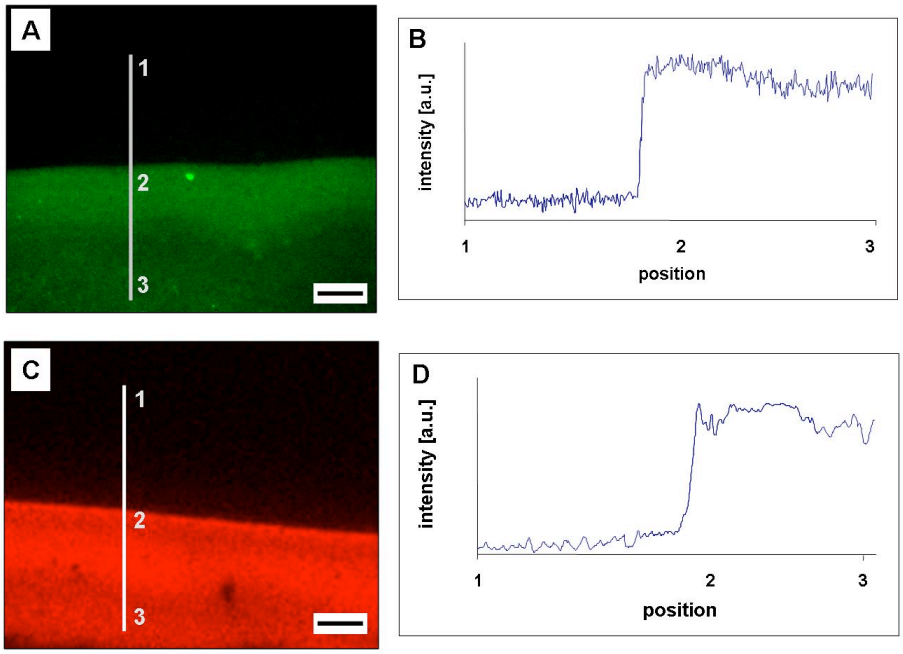

Figure 75: **Fluorescence image of thiol modified streptavidin (HS-SAv), immobilized on a PEG passivated, gold nanopatterned glass slide.** The upper part of the images are non patterned areas on the glass slide, while the lower part is nanostructured with gold particles, working as anchor points for HS-SAv. A: HS-SAv, labelled with a fluorescent dye (Alexa Fluor 488), was directly bound to the gold dots on the surface; B: intensity profile along the grey line in (A); C: HS-SAv was immobilized on the gold dots. Fluorescently labelled biotin (Alexa Fluor 532) was attached to the HS-SAv; D: intensity profile along the grey line in (C). The scale bars correspond to 1 μm.

The successful attachment of thiol modified SAv, carrying a fluorescent dye

(Alexa Fluor 488), can clearly be observed (figure 75A). In the non-dipped area (upper part) there is hardly any fluorescence visible, while in the dipped area (lower part) the fluorescence of the dye can be detected. The difference in fluorescence is also visible in the intensity profile (figure 75B). Only low fluorescence is detectable at position 1. There are no gold dots present in this part of the surface. The PEG passivation successfully prevents the protein from binding to the surface. At position 2, the dipping edge, a sharp increase in intensity occurs. The thiol-modified protein is able to bind to the gold nanodots, present on the surface. The higher intensity in fluorescence in the first micrometer of the nanopatterned area refers to a higher density of the gold dots, due to the dip coating process. The uniform fluorescence in the patterned area of the glass slide (position 3, figure 75B) indicates, that the thiol modified protein binds to the gold dots on the surface.

In order to control the biotin binding activity, thiolated SAv is immobilized on gold dots of nanopatterned glass slide. With an Alexa Fluor 532 dye fluorescently labelled biotin (biotin AF532) is added to the immobilized SAv. Figure 75C depicts the fluorescence image, depicted from this experiment. Also here, fluorescence can be only detected in the area, functionalized with the gold dots. The intensity profile over the grey line in the flurescence image validates the data (figure 75D). The profile starts in the PEG passivated area of the surface, where no fluorescence can be detected. The value in this area was again used to substract the background of the image. At the dipping edge, corresponding to position 2, a substantial increase of fluorescence occurs, indicating the beginning of the nanopatterning of the substrate. Also here a higher intensity is observed in approximately the first micrometer of the patterning, resulting from then higher density of the gold nanodots in this area. Going to the homogenously patterned surface (position 3, figure 75D), the fluorescence stays constant.

Taking the results together, it is possible to modify SAv with iminothiolane, without inhibiting the biotin binding properties. The modified protein binds specifically to gold dots on the surface, while the PEG passivation prevents from unspecific adsorption to the area between the gold nanopattern.

To see, if the kinetics of the biotin binding process is influenced by the modification of streptavidin, we performed QCM-D measurements, which enables the in situ observation of the biotin binding to the streptavidin. These experiments were carried the out on a homogenous gold surface, as well as on a silicon oxide surface with a supported lipid bilayer. The second experiment allows a direct comparison with the experiments, carried out with the unmodified SAv, as described in part 6.1.

It is possible to attach the modified protein under flow conditions on surfaces. The formation of the SAv layer is followed in QCM-D measurements on a supported bilayer as well as on gold (figure 76 and figure 77).

To compare the biotin binding activity of the thiol modified SAv with the unmodified one, we immobilized repeated the immobilization experiments on a biotin doped bilayer, but with the modified protein (figure 76A). We used fully

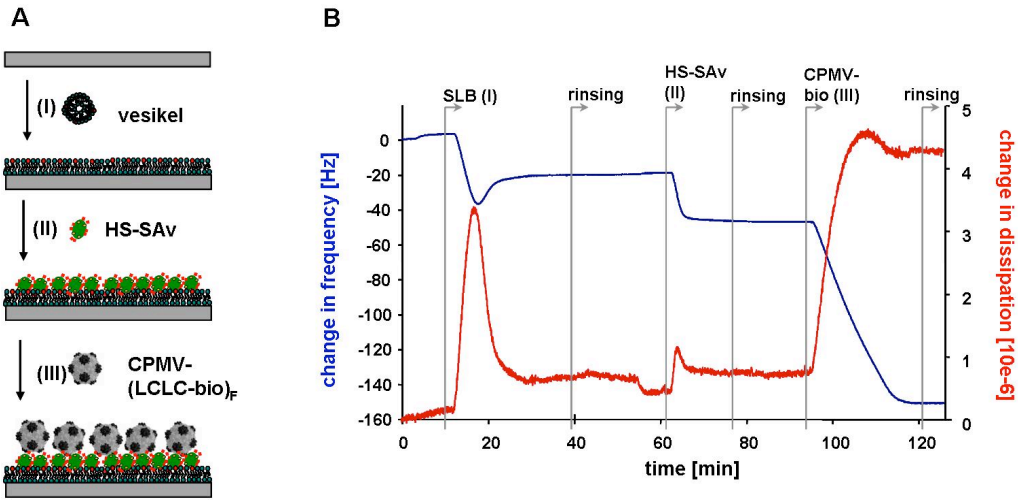

Figure 76: **Immobilization of biotin modified cowpea mosaic virus (CPMV) particles on a biotin doped supported lipid bilayer (SLB) via thiol modified streptavidin (HS-SAv).** A: schematic drawing of the formed layers; B: QCM-D measurement of the formed layers. Shown is the 5th overtone. The added virions were fully coated with biotin, over the long spacer.

decorated CPMV, where the biotin is separated about 3 nm from the particle, as we obtained with this modification the most uniform layers on streptavidin. The formation of the bilayer out of vesicles (t = 10 – 39 min) causes the same changes in frequency and dissipation as in the above described cases, indicating a good quality (figure 76B). Thiol modified SAv (t = 61 – 76 min) is forming a layer on it, resulting in change of the frequency of –28 Hz, and a change in dissipation of $0{,}3 \cdot 10^{-6}$. These values are in good agreement with the ones, obtained for non modified SAv, where the frequency changes –29 Hz and the dissipation $0{,}2 \cdot 10^{-6}$ (figure 76A). Adding the biotin modified CPMV (t = 94 – 122 min) is the origin for a frequency change of –105 Hz and dissipation change of $3{,}6 \cdot 10^{-6}$. The change in dissipation is in accordance with the layer on the non-modified SAv, but the change in the frequency indicates a less dense layer of the CPMV. The value is similar to the one, obtained in the second CPMV layer, where it was only partly decorated with biotin (figure 76C). This value can not be explained by the roughness of the surface, as there is only a layer of SAv on the SLB. In agreement with our measurements, we assume a dens layer. So obviously, the HS-SAv is not able to bind as many biotin modified CPMVs as the unmodified one.

To see, if the effect is the same on gold, we performed the experiment but this time on an activated gold surface (figure 77A). The formation of the layers is here also followed by QCM-D (figure 77B).

The thiol modified SAv binds to the gold surface, resulting in a change in frequency of –21 Hz, corresponding to a mass uptake of 370 ng/cm^2, compared to

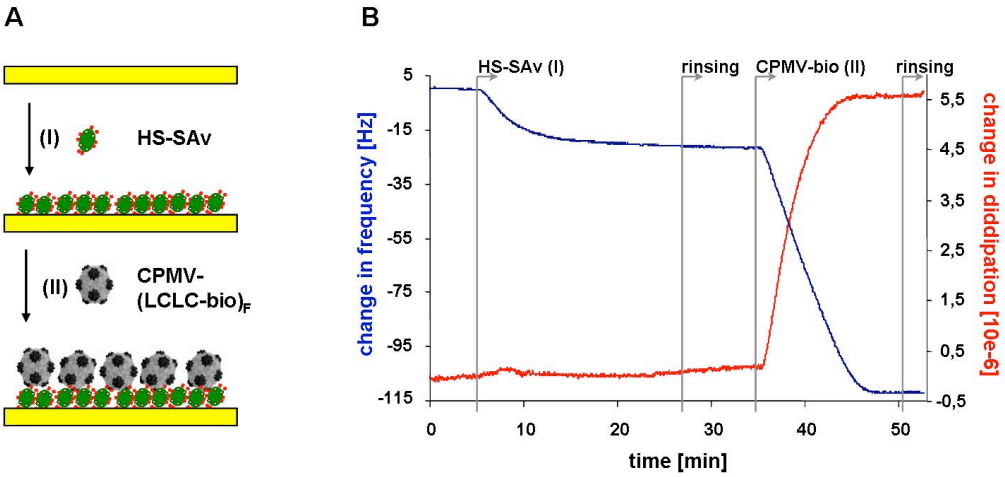

Figure 77: **CPMV attached to thiolated streptavidin (HS-SAv) on a gold surface.** A: schematic drawing of the stepwise layer formation; B: QCM-D measurement, shown is the 5th overtone. The added virions were fully coated with biotin, over the long spacer

510 ng/cm^2 in the case on the supported lipid bilayer. A more unlikely reason could be, that less water (solvent) is adsorbed in the HS-SAv layer. But thiol groups usually do not affect the solubility in aqueous solution. A more reliable explanation is that the formed HS-SAv layer on gold is not as dense as the ones on the biotin-doped bilayer. The change in dissipation ($\Delta D = 0{,}1 \cdot 10^{-6}$) is in agreement with the previous measurements. This HS-SAv layer serves as binding site for the biotinylated CPMV. The change in frequency (Δf = -90 Hz) as well was the change in dissipation ($\Delta D = 5{,}4 \cdot 10^{-6}$) differs from the experiments on a bilayer. The formed layer is not as dense, while the higher change in dissipation indicates a softer film. The VNPs are not attached rigidly to the layer. The value is comparable to the second CPMV layers (table 5), assuming a more flexible attachment. Probably, the binding activity of the HS-SAv layer on the gold is less than on the bilayer. The values, working with the thiol modified SAv, are summed up in table 6:

Table 6: Comparison of the immobilization of CPMV-(LCLC-bio)$_F$ with thiol modified modified and unmodified streptavidin on gold and a supported lipid bilayer.

	HS-SAv on Gold		HS-SAv on SLB		SAv on SLB	
	Δf [Hz]	ΔD [10^{-6}]	Δf [Hz]	ΔD [10^{-6}]	Δf [Hz]	ΔD [10^{-6}]
SAv	-21	0,1	-28	0,3	-29	0,2
CPMV	-90	5,4	-105	3,6	-121	3,1

We used SAv to build a bilayer of biotin modified CPMV on a surface. The density of biotin, present at the VNPs, influences the roughness of the formed layers, as well as the length of the spacer. In order to transfer this system on a

nanopatterned substrate, we first investigated a method to directly immobilize SAv on gold, by introducing a thiol group on the lysine residues. In QCM-D experiments we could show, that the biotin binding activity is reduced, but not completely suppressed by this modification.

Part IV
Outlook

7 Outlook

In this work, different methods for the immobilization of inorganic nanocrystals are presented. One can imagine several application for such substrates in nanotechnology, as already the bare colloidal nanocrystals exhibit a variety of properties. The project could be continued either in the direction of material science or in the direction of application. For both directions, the patterning of the substrates via block copolymer nanolithography might further be analyzed.

Regarding the material aspect, further improvements in the aligning of the nanoparticles on the substrate are possible.

The approach of stretching ssDNA between gold particles on the surface as described in section 1.5.1 could be employed as programmable surface. The ssDNA offers defined binding sites due to its predefined base sequence. The distance of 60 nm between the gold particles on the surface is bridged by a strand of 178 nucleotides, where 153 of them remain free for further functionalization. Colloidal nanocrystals, modified with ssDNA, can now be directed towards a defined position between the gold dots on the surface. The precise position is predetermined by the sequence of the DNA, as sketched in figure 78. This system could be used to investigate on the distance dependency of the interaction between the two types of particles on the surface.

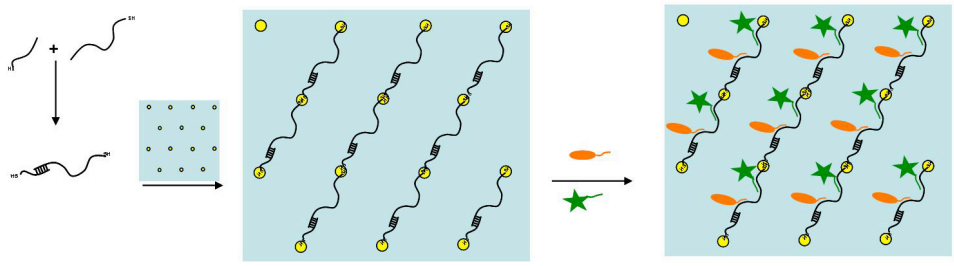

Figure 78: **Building of a programmable surface with ssDNA**. The predesigned sequence is guiding DNA modified nanoparticles to defined positions on the surface.

The attachment of inorganic nanoparticles via a dithiol linker could be extended by the introduction of further processing steps. An alignment of anisotropic Co-Au matchsticks is possible by application of a magnetic field during the deposition, as shown in section 4.2.3. In a second step, new Co-Au matchsticks are provided and aligned in a magnetic field which is now oriented under an angle of 60° as compared to the first one, resulting in a diamond lattice (figure 79).

In a similar way the alignment of CdSe-Au dumbbells and matchsticks can be envisaged, but by working with an electric instead of a magnetic field. Dense alignment of CdSe rods on an unstructured surface in an electric field is demonstrated in literature [216]. As only few material show ferromagnetic

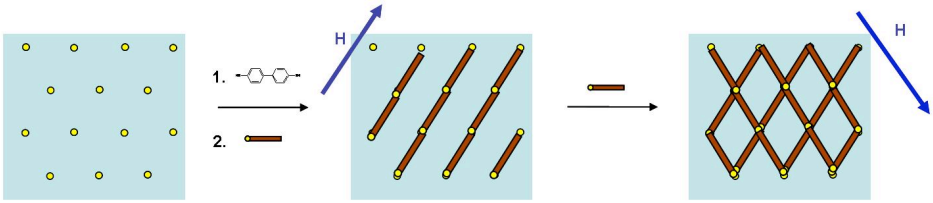

Figure 79: **Schematic drawing for the alignment of magnetic particles in a magnetic field H.** After afirst alignment, new precursor is added to the substrate and also aligned in a magnetic field, resulting in a diamond lattice.

properties and in the same time can be grown in a rod shape, the alignment in an electric field might be more versatile. For instance combinations of CdSe and CdTe or CdS nanoparticles could be aligned under different orientations on the surface, including rotations of 180°.

The growth directly on the surface can be further investigated for Co as well as for CdSe. Growing Co particles on the surface might also work starting from other than platinum nanoparticles. Looking on the crystal structure of Co, ruthenium and iron should allow an epitaxial growth. Also growth directly from Co nanoparticles on the surface would be interesting. Comparing the different materials in conjunction with high resolution electron microscopy might give a deeper insight in the growth mechanism and help to elucidate the role of the particles on the surface. It is still unclear, whether the metal nanoparticles serve as seeds or catalysts for the growth of the Co rods.

The synthesis of rods on surfaces from solution could be extended to further materials. Especially for the scheme for the growth of CdSe one can imagine extensions to other materials. For example other II-VI semiconductor nanocrystals, such as CdTe or CdS, have similar growth conditions.

For the CdSe nanowires a use as solar cell might be possible. The semiconductor nanowires are known to be efficient absorbers for light in the visible spectrum [29, 217]. The current design of nanocrystal-based solar cells uses a blend of colloidal nanocrystals with a conductive polymer. An electron-hole pair generated in a nanocrystal is separated on the crystals' surface. One type of carrier is transported through the polymer to an electrode, while the other is transported through the nanocrystal to the opposite electrode. This approach is generally limited by the absence of a percolating network of nanocrystals. The distance, over which carriers can be transported, is thus limited to the dimensions of the nanocrystals. And thus also the absorbing volume is limited. Additionally the contact between the nanocrystals and the electrode is often far from optimal. The advantage of the SLS approach described in this work as compared to other designs, is that the nanowires are directly attached to a surface and thus one can expect to find an ohmic contact. Figure 80 displays a sketch of a possible layout.

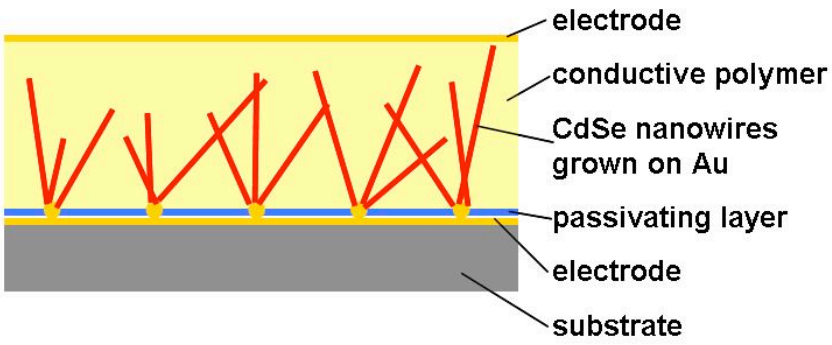

Figure 80: **Sketch of a possible layout for an application as solar cell.** Gold dots are deposited onto a substrate, which should ideally be transparent, as well as the lower electrode, e.g. ITO on glass. The upper electrode can be some metal that is evaporated onto the device.

References

[1] W. Luther. Industrial application of nanomaterials - chances and risks. *VDI-Technologiezentrum*, 2004.

[2] London Royal Society. *Nanoscience and nanotechnology: Opportunities and uncertainties. Technical Report*. The Royal Society & The Royal Academiy of Engineering, 2004.

[3] R. P. Feynman. There's plenty of room at the bottom. *Engineering and Science*, 23:22–36, 1960.

[4] B. Bhushan. *Springer Handbook of Nanotechnology*. Springer Verlag, Berlin, Germany, 2004.

[5] M. A. McCord. Electron beam lithography for 0,13 um manufacturing. *J. Vac. Sci. Technol.*, 15(6):2125–2129, 1997.

[6] J. Melngailis. Focused ion beam technology and applications. *J. Vac. Sci. Technol.*, 5(2):469–495, 1987.

[7] G. L.-T. Chiu and J. M. Shaw. Optical lithography: Introduction. *IBM J. Res. & Devel.*, 41((1/2)), 1997.

[8] Stephan Foerster. Amphiphilic block copolymers for templating applications. *Top Curr Chem*, 226:1–28, 2003.

[9] Stephan Foerster and Thomas Plantenberg. Funktionale Strukturhierarchien aus selbstorganisierenden Polymeren. *Angewandte*, 114:712–739, 2002.

[10] I. W. Hamley. Nanostructure fabrication using blockcopolymers. *Nanotechnology*, 14:R39–R54, 2003.

[11] Nadrian C. Seeman. DNA nanotechnology: Novel DNA constructions. *Annual Review of Biophysics and Biomolecular Structure*, 27:225–248, 1998.

[12] Yinli Wang, John E. Mueller, Börries Kemper, and Nadrian C. Seeman. Assembly and charecterization of five-arm and six-arm DNA branched junctions. *Biochemistry*, 30:5667–5674, 1991.

[13] David S. Ginger, Hua Zhang, and Chad A. Mirkin. Zur Entwicklung der Dip-Pen-Nanolithographie. *Angewandte Chemie*, 116:30–46, 2004.

[14] Y. Xia, J. A. Rogers, K. E. Paul, and G. M. Whitesides. Unconventional methods for fabricating and patterning nanostructures. *Chem. Rev.*, 99:1823–1848, 1999.

[15] Joachim P. Spatz, Vanessa Z.-H. Chan, Stefan Mößmer, Frank-Michael Kamm, Alfred Plettl, Paul Ziemann, and Martin Möller. A combined top-down/bottom-up approach to the microscopic localization of metallic nanodots. *Advanced Materials*, 14:1827–1832, 2002.

[16] Joy Y. Cheng, Caroline A. Ross, Henry I. Smith, and Edwin L. Thomas. Templated self-assembly of block copolymers: Top-down helps bottom-up. *Advanced Materials*, 18:2505–2521, 2006.

[17] A. Paul Alivisatos. Nanocrystals: building blocks for modern materials design. *Endeavour*, 21(2):56–60, 1997.

[18] Emil Roduner. Size matters: why nanomaterials are different. *Chem. Soc. Rev.*, 35:583–592, 2006.

[19] R. C. Somers, M. G. Bawendi, and D. G. Nocera. CdSe nanocrystal based chem-/bio- sensors. *Chem. Soc. Rev.*, 36:579–591, 2007.

[20] Z. Adam Peng and Xiaogang Peng. Mechanism of the shape evolution of CdSe nanocrystals. *J. Am. Chem. Soc.*, 123:1389–1395, 2001.

[21] Liberato Manna, Erik C. Scher, and A. Paul Alivisatos. Synthesis of soluble and processable rod-, arrow-, teardrop-, and tetrapod-shaped CdSe nanocrystals. *J. Am. Chem. Soc.*, 122:12700–12706, 2000.

[22] Xiaogang Peng, Liberato Manna, Weidong Yang, Juanita Wickham, Erik C. Scher, Andreas Kadavanich, and A. Paul Alivisatos. Shape control of CdSe nanocrystals. *Nature*, 404:59–61, 2000.

[23] Liberato Manna, Delia J. Milliron, Andreas Meisel, Erik C. Scher, and A. Paul Alivisatos. Controlled growth of tetrapod-branched inorganic nanocrystals. *Nature Materials*, 2:382–385, 2003.

[24] Z. Adam Peng and Xiaogang Peng. Nearly monodisperse and shape-controlled CdSe nanocrystals via alternative routes: Nucleation and growth. *J. Am. Chem. Soc.*, 124:3343–3353, 2002.

[25] Sandeep Kumar and Thomas Nann. Shape control of II-VI semiconductor nanomaterials. *Small*, 2:316–329, 2006.

[26] Y. Khalavka and C. Soennichsen. Growth of gold tips onto hyperbranched CdTe nanostructures. *Adv Mater*, 20:588–591, 2008.

[27] S. Kudera. *Formation of Colloidal Nanocrystals - The Aspect of Nucleation*. PhD thesis, Ludwig-Maximilians Universität, München, 2007.

[28] 6th Frameworkprogram of EU. Self assembly of shape controlled colloidal nanocrystals (http://www.sa-nano.it).

[29] L. A. Kosoyachenko, E. V. Grushko, and A. I. Savchuk. Depndence of charge collection in thin- film CdTe solar cells on the adsorber layer parameters. *Semiconductor Science and Technology*, 23:025011 (7pp), 2008.

[30] Emily A. Weiss, Venda J. Porter, Ryan C. Chiechi, Scott M. Geyer, David C. Bell, Moungi G. Bawendi, and George M. Whitesides. The use of size-selective excitation to study photocurrent through junctions containing single-size and multi-size arrays of colloidal CdSe quantum dots. *Journal of the American Chemical Society*, 130:83–92, 2008.

[31] Christof M. Niemeyer. Nanopartikel, Proteine und Nucleinsäuren: Die Biotechnologie begegnet den Materialwissenschaften. *Angewandte Chemie*, 113:4254 – 4287, 2001.

[32] David W. Grainger and David G. Castner. Nanobiomaterials and nanoanalysis: Opportunities for improving the science to benefit biomedical techologies. *Adv Mater*, 20:867–877, 2008.

[33] V. F. Puntes, P. Gorostiza, D. M. Aruguete, N. G. Bastus, and A. P. Alivisatos. Collective behaviour in two-dimensional cobalt nanoparticle assemblies observed by magnetic force microscopy. *Nat Mater*, 3:263–268, 2004.

[34] J. Bansmann, S. Kielbassa, H. Hoster, F. Weigl, H. G. Boyen, U. Wiedwald, P. Ziemann, and R. J. Behm. Controlling the interparticle spacing of Au-salt loaded micelles and Au nanoparticles on flat surfaces. *Langmuir*, 23:10150–10155, 2007.

[35] G. A. DeVries, M. Brunnbauer, Y. Hu, A. M. Jackson, B. Long, B. T. Neltner, O. Uzun, B. H. Wunsch, and F. Stellacci. Divalent nanoparticles. *Science*, 315:358–361, 2007.

[36] A. Paul Alivisatos. Perspectives on the physical chemistry of semiconductor nanocrystals. *J. Phys. Chem.*, 100:13226–13239, 1996.

[37] C.A. Mirkin, Robert L. Letsinger, Robert C. Mucic, and James J. Storhoff. A DNA based method for the rationally assmebling nanoparticles into macroscopic materials. *Nature*, 382:607–609, 1996.

[38] B. L. Sanchez-Gaytan, W. Cui, Y. J. Kim, M. A. Mendez-Polanco, T. V. Duncan, M. Fryd, B. B. Wayland, and S. J. Park. Interfacial assembly of nanoparticles in discrete block-copolymer aggregates. *Angewandte Chemie*, 119:9395–9398, 2007.

[39] Wenchao Sheng, Sungjee Kim, Jinwook Lee, Sang-Wook Kim, Klavs Lensen, and Moungi G. Bawendi. In-situ encapsulation of quantum dots into polymer microspheres. *Langmuir*, 22:3782–3790, 2006.

[40] D.E. Fogg, L.H. Radzilowski, B.O. Dabbousi, R.R. Schrock, E.L. Thomas, and M.G. Bawendi. Fabrication of quantum dot-polymer composites: Semiconductor nanoclusters in dual-function polymer matrices with electron-transporting and cluster-passivating properties. *Macromolecules*, 30(26):8433–8439, 1997.

[41] Bryan D. Korth, Pei Keng, Inbo Shim, Steven E. Bowles, Chuanbing Tang, Tomasz Kowalewski, Kenneth W. Nebesny, and Jeffrey Pyun. Polymer-coated ferromagnetic colloids from well-defined macromolecular surfactants and assembly into nanoparticle chains. *J. Am. Chem. Soc.*, 128:6562–6563, 2006.

[42] Nanosensors GmbH Neuchatel, Switzerland. www.nanosensors.com.

[43] Katerina Soulantica, Laurent Erades, Muriel Sauvan, Francois Senocq, Andre Maisonnat, and Bruno Chaudret. Synthesis of indium and indium oxide nanoparticles from indium cyclopentadienyl precursor and their application for gas sensing. *Advanced Functional Materials*, 13:553–557, 2003.

[44] Luigi Carbone, Concetta Nobile, Milena De Giorgi, Fabio Della Salla, Giovanni Morello, Pierpaolo Pompa, Martin Hytch, Etienne Snoeck, Angela Fiore, Isabella R. Franchini, Monica Nadasan, Albert F. Silvestre, Letizia Chiodo, Stefan Kudera, Roberto Cingolani, Roman Krahne, and

Liberato Manna. Syntheisis and micrometer-scale assembly of colloidal CdSe/CdS nanorods prepared by a seeded growth approach. *Nano Letters*, 7:2942–2950, 2007.

[45] A. L. Rogach, D.V. Talapin, E.V. Shevchenko, A. Kornowski, M. Haase, and H. Weller. Organization of matter on different size scales: Monodisperse nanocrystals and their superstructures. *Adv. Funct. Mater.*, 12(10):653–664, 2002.

[46] C. B. Murray, C. R. Kagan, and M. G. Bawendi. Self-organization of CdSe nanocrystallites into three-dimensional quantum dot superlattices. *Science*, 270:1335–1338, 1995.

[47] Dov Steiner, Doron Azulay, Assaf Aharoni, Assaf Salant, Uri Banin, and Oded Millo. Electronic structure and self-assembly of cross-linked semiconductor nanocrystal arrays. *Nanotechnology*, 19:065201(4pp), 2008.

[48] X. K. Zhao, S. Xu, and H. J. Fendler. Semiconductor particles formed at monolayer surfaces. *Langmuir*, 7:520–524, 1991.

[49] Y. Yuan, I. Cabasso, and J. H. Fendler. Preparation of ultrathin, size-quantized semiconductor particulate films at oriented mono- and poly[(vinylbenzyl)phosphonate] interfaces and their characterization on solids. *Chem Mater*, 2:226–229, 1990.

[50] K. C. Yi and J. H. Fendler. Template-directed semiconductor size quantization at monolayer-water interfaces and between the headgroups of langmuir -blodgett films. *Langmuir*, 6:1519–1521, 1990.

[51] X. K. Zhao, L. D. McCormick, and J. H. Fendler. Preparation-dependent rectification behvior of lead sulfide particulate films. *Adv. Mater.*, 4:93, 1992.

[52] K. C. Yi, Z. Horvoelgyi, and J. H. Fendler. Chemical formation of silver particulate films under monolayers. *J. Phys. Chem.*, 98:3872–3881, 1994.

[53] Janos H. Fendler. *Advances in Polymer Series - Membrane-Mimetic Approach to Advanced Materials*, volume 113. Springer Verlag, Berlin, 1994.

[54] Janos H. Fendler and Fiona C. Meldrum. The colloid chemical approach to nanostructured materials. *Advanced Materials*, 7:607–632, 1995.

[55] K. M. Gattas-Asfura, C. A. Constantine, M. J. Lynn, D. A. Thimann, X. Ji, and R. M. Leblanc. Characterization and 2D self-assemby of CdSe quantum dots at the air-water interface. *J. Am. Chem. Soc.*, 127:14640–14646, 2005.

[56] A. Ulman. *An Introduction to Ultrathin Films: From Langmuir-Blodgett to Self-Assembly*. Academic Press Inc., San Diego, USA, 1991.

[57] R. A. Sperling, T. Liedl, S. Duhr, Stefan Kudera, M. Zanella, C.-A. J. Lin, W. H. Chang, D. Braun, and W.J. Parak. Size determination of (bio)conjugated water-soluble colloidal nanoparticles: A comparison of different techniques. *J. Phys. Chem.*, 111:11552–11559, 2007.

[58] Byung Soo Kim, Soo Young Lee, Young Ho Cho, Ju Yong Youn, Moon Suk Kim, Gilson Khang, and Lee. Hai Bang. Preparation of a polymer surface coated with agradient of quantum dots. *Nanotechnology*, 19:045301 (6pp), 2008.

[59] Hanying Li, Sung Ha Park, John H. Reif, Thomas H. LaBean, and Hao Yan. DNA-templated self-assembly of protein and nanoparticle linear arrays. *J. Am. Chem. Soc.*, 126:418–419, 2004.

[60] Ralf M. Zimmermann and Edward C. Cox. DNA stretching on functionalized gold surfaces. *Nucleic Acids Research*, 22:492–497, 1994.

[61] Joachim P. Spatz, Thomas Herzog, Stefan Moessmer, Paul Ziemann, and Martin Moeller. Micellar inorganic-polymer hybrid systems - a tool for nanolithography. *Advanced Materials*, 11:149–153, 1999.

[62] Roman Glass, Marco Arnold, Jacques Bluemmel, Alexander Kueller, Martin Moeller, and Joachim P. Spatz. Micro-nanostructured interfaces fabricated by the use of inorganic block copolymer micellar monolayers as negative resist for electron-beam lithography. *Advanced Functional Materials*, 13:569–575, 2003.

[63] Roman Glass, Martin Moeller, and Joachim P. Spatz. Block copolymer micelle nanolithiography. *Nanotechnology*, 14:1153–1160, 2003.

[64] Theobald Lohmueller, Eva Bock, and Joachim P. Spatz. Synthesis of quasi-hexagonal ordered arrays of metallic nanoparticles with tuneable particle size. *Advanced Materials*, 20(12):2297–2302, 2008.

[65] I.I. Potemkin, E.Yu. Kramarenko, A.R. Khokhlov, R.G. Winkler, P. Reineker, P. Eibeck, J.P. Spatz, and M. Möller. Nanopattern of diblock copolymers selectively adsorbed on a plane surface. *Langmuir*, 15(21):7290–7298, 1999.

[66] Cheolmin Park, Jongseung Yoon, and E. L. Thomas. Enabling nanotechnology with self assembled block copolymer patterns. *Polymer*, 44:6725–6760, 2003.

[67] Z. Li, W. Zhao, Y. Liu, M.H. Rafailovich, J. Sokolov, K. Khougaz, A. Eisenberg, R.B. Lennox, and G. Krausch. Self-ordering of diblock copolymers from solution. *Journal of the American Chemical Society*, 118(44):10892–10893, 1996.

[68] Matthias Geissler and Younan Xia. Patterning: Principles and some new development. *Advanced Materials*, 16:1249–1269, 2004.

[69] Joachim P. Spatz, Sergei Sheiko, and Martin Möller. Ion-stabilized block copolymer micelles: Film formation and intermicellar interaction. *Macromolecules*, 29:3220–3226, 1996.

[70] L. Isaacs, D. N. Chin, N. Bowden, Y. Xia, and G. M. Whitesides. *Supermoleculear Materials and Technologies*, chapter Supermoleculear Materials and Technologies. John Wiley & Sons, New York, 1999.

[71] A. R. Shultz and P. J. Flory. Phase equilibria in polymer-solvent systems. *Journal of the American Chemical Society*, 74:4760–4767, 1952.

[72] A. R. Shultz and P. J. Flory. Equlibria in polymer-solvent systems. II. thermodynamic interaction parameters from critical miscibility data. *Journal of the American Chemical Society*, 75:3888–3892, 1953.

[73] Stefan Moessmer. *Size Control of Metallic Nanoparticles and Surface Patterning by Self-Assembly of Diblock Copolymers*. PhD thesis, Universität Ulm, 1999.

[74] M. W. Matsen. The standard gaussian model for block copolymer melts. *J. Phys.: Condens. Matter*, 14:R21–R47, 2002.

[75] I. W. Hamley. *The Physics of Block Copolymers*. Oxford University Press, Oxford, 1998.

[76] J.J. Chiu, B.J. Kim, E.J. Kramer, and D.J. Pine. Control of nanoparticle location in block copolymers. *Journal of the American Chemical Society*, 127(14):5036–5037, 2005.

[77] J.C. Meiners, A. Quintel-Ritzi, J. Mlynek, H. Elbs, and G. Krausch. Adsorption of block-copolymer micelles from a selective solvent. *Macromolecules*, 30(17):4945–4951, 1997.

[78] A. Johner and J. F. Joanny. Block copolymer adsorption in a selective solvent: a kinetic study. *Macromolecules*, 23(26):5299–5311, 1990.

[79] Ludwig Leibler, Henri Orland, and Lohn C. Wheeler. Theory of critical micelle concentration for solutions of block copolymers. *J Chem Phys*, 79:3550–3557, 1983.

[80] Stefan Moessmer, Joachim P. Spatz, Martin Moeller, Thomas Aberle, Juergen Schmidt, and Walther Burchard. Solution behavior of poly(styrene)-block-poly(2-vinylpyridine) micelles containing gold nanoparticles. *Macromolecules*, 33:4791–4798, 2000.

[81] Z. Gao and A. Eisenberg. A model of micellization for block copolymers in solutions. *Macromolecules*, 26:7353–7360, 1993.

[82] Ciro Esposito, Patrizia Colicchio, Angelo Facchiano, and Raffaele Ragone. Effect of a weak electrolyte on the critical micellar concentration of sodium dodecyl sulfate. *Journal of Colloidal and Interface Sience*, 200, 1998.

[83] Gerd Kaestle, Hans-Gerd Boyen, Frank Weigl, Gunther Lengl, Thomas Herzog, Paul Ziemann, Silke Riethmüller, Oliver Mayer, Christoph Hertmann, Joachim P. Spatz, Martin Möller, Masaki Ozawa, Florian Banhart, Michael G. Garnier, and Peter Oelhafen. Micellar nanoreactors - preparation and characterization of hexagonally ordered arrays of metallic nanodots. *Advanced Functional Materials*, 13:853–861, 2003.

[84] Y. Liu, W. Zhao, X. Zheng, A. King, A. Singh, M. H. Rafailovich, J. Sokolov, K. H. Dai, and E. J. Kramer. Surface-induced ordering in asymmetric block copolymers. *Macromolecules*, 27(14):4000–4010, 1994.

[85] Masato Aizawa and Jillian M. Buriak. Block copolymer templated chemistry for the formation of metallic nanoparticles arrays on semiconductor surfaces. *Chem. Mater.*, 19:5090–5101, 2007.

[86] Masato Aizawa and Jillian M. Buriak. Block copolymer-templated chemistry on Si, Ge, InP, and GaAs surfaces. *J. Am. Chem. Soc.*, 127:8932–8933, 2005.

[87] J. C. Meiners, A. Ritzi, M. H. Rafailovich, J. Sokolov, J. Mlynek, and G. Krausch. Two-dimensional micelle formation of polystyrene-poly(vinylpyridine) diblock copolymers on mica surfaces. *Applied Physics A: Materials Science & Processing*, 61(5):519–524, November 1995.

[88] C. Soennichsen, B. M. Reinhard, J. Liphardt, and A. P. Alivisatos. A molecular ruler based on plasmon coupling of single gold and silver nanoperticles. *Nat. Biotech.*, 23:741–745, 2005.

[89] A. P. Alivisatos. The use of nanocrystals in biological detection. *Nat. Biotech.*, 22:47–52, 2004.

[90] C. L. Haynes and R. P. Van Duyne. Nanosphere lithography: A verstaile nanofabrication tool for studies of size-dependent nanoparticle optics. *J. Phys. Chem. B*, 105:5599–5611, 2001.

[91] Y. W. Cao, R. Jin, and C.A. Mirkin. DNA-modified core-shell Ag/Au nanoparticles. *J. Am. Chem. Soc.*, 123(32):7691–7692, 2001.

[92] Juergen Groll, Krystyna Albrecht, Peter Gasteier, Silke Riethmueller, Ulrich Ziener, and Martin Moeller. Nanostructured ordering of fluorescent markers and single proteins on substrates. *ChemBioChem*, 6:1782–1787, 2005.

[93] Juergen Groll, Elza V. Amirgoulova, Thomas Ameringer, Colin D. Heyes, Carlheinz Roecker, G. Ulrich Nienhaus, and Martin Moeller. Biofunctionalized, ultrathin coatings of cross-linked star-shaped poly(ethylene oxode) allow reversible folding of immobilized proteins. *J. Am. Chem. Soc.*, 126:4234–4239, 2004.

[94] Tobias Wolfram, Ferdinand Belz, Tobias Schoen, and J. P. Spatz. Site-specific presentation of single recombinant proteins in defined nanoarrays. *Biointerphases*, 2(1):44–48, 2007.

[95] Marco Arnold, Vera C. Hirschfeld-Warneken, Theobald Lohmueller, Patrick Heil, Jacques Bluemmel, Elisabetta A. Cavalcanti-Adam, Monica Lopez-Garcia, Paul Walther, Horst Kessler, Benjamin Geiger, and Joachim P. Spatz. Induction of cell polarization and migration by a gradient of nanoscale variations in adhesive ligand spacing. *Nano Letters*, 8:2063–2069, 2008.

[96] P. Reiss. *Semiconductor Nanocrystal Quantum Dots*, chapter Synthesis of semiconductor nanocrystals in organic solvents. Springer, Wien, New York, 2008.

[97] R. Kubo. Electronic properties of metallic fine particles. I. *J. Phys. Soc. Jpn.*, 17:975–986, 1962.

[98] William E. Buhro and Vicki L. Colvin. Semiconductor nanocrystals - shape matters. *Nature Materials*, 2:138–139, 2003.

[99] S. Kudera, L. Carbone, E. Carlino, R. Cingolani, P. D. Cozzoli, and L. Manna. Synthesis routes for the growth of complex nanostructures. *Physica E*, 37:128–133, 2007.

[100] X. Michalet, F. F. Pinaud, Thilo D. Lacoste, Maxime Dahan, M. P. Bruchez, A. Paul Alivisatos, and Shimon Weiss. Properties of fluorescent semiconductor nanocrystals and their application to biological labeling. *Single Mol.*, 2:261–276, 2001.

[101] M. G. Bawendi, M. L. Steigerwald, and L. E. Brus. The quantum-mechanics of larger semiconductor clusters and dots. *Ann. Rev. Phys. Chem.*, 41:477–496, 1990.

[102] P. J. Thomas and P. O'Brien. A simple numerical calculatio correctly predicts the observed size regime for growth of tetrapodal chalcogenide nanocrystals. *J. Am. Chem. Soc.*, 128:5614–5615, 2006.

[103] J. S. Garitaonandia, Maite Insauusti, Eider Goikolea, John D. Suzuki, Motohiro ad Cashio, Naomi Kawamura, Hitoshi Ohsawa, Izakun Gil de Muro, Kiyonori Suzuki, Fernando Piazaola, and Teofilo Rojo. Chemically induced permanent magnetism in Au, Ag, and Cu nanoparticles: Localization of the magnetism by element selective techniques. *Nano Lett.*, 8(2):661–667, 2008.

[104] H. Liu, B. S. Mun, G. Thomton, S. R. Isaacs, Y. S. Shon, Ogletree. D. F., and M. Salmeron. Electronic structure of ensembles of gold nanoparticles: Size and proximity effects. *Phys. Rev. B*, 72:155430–155434, 2005.

[105] K. J. Nobusada. Electronic structure and photochemical properties of a monolayer-protected gold cluster. *J. Phys. Chem. B*, 108:11904–11908, 2004.

[106] W. J. Parak, L. Manna, F. C. Simmel, D. Gerion, and P. Alivisatos. *Nanoparticles: From Theory to Application*, chapter Quantum Dots. WILEY-VCH Verlag GmbH, Weinheim, 2004.

[107] S. V. Gaponenko. *Optical properties of semiconductor nanocrystals*. Cambridge University Press, Cambridge, UK, 1998.

[108] D. J. Norris, A. Sacra, C. B. Murray, and M. G. Bawendi. Measurement of the size-dependent hole spectrum in CdSe quantum dots. *Phys. Rev. Lett.*, 72:2612–2615, 1994.

[109] Heng Yu and William E. Buhro. Solution-liquid-solid growth of soluble GaAs nanowires. *Advanced Materials*, 15:416–419, 2003.

[110] X. Michalet, F. F. Pinaud, L. A. Bentolila, J. M. Tsay, S. Doose, J. J. Li, G. Sundaresan, A. M. Wu, S. S. Gambhir, and S. Weiss. Quantum dots for live cells, in vivo imaging, and diagnostics. *Science*, 307:538, 2005.

[111] Patricia M. A. Farias, Beate S. Santos, AndrÈ A. de Thomaz, Ricardo Ferreira, Frederico Menezes, Carlos L. Cesar, and Adriana fontes. Fluorescent II-VI semiconductor quantum dots in living cells: Nonlinear microspectroscopy on an optical tweezers system. *J. Phys. Chem. B*, 112:2734–2737, 2008.

[112] Ron Gill, Lily Bahshi, Ronit Freeman, and Itamar Willner. Optical detection of glucose and acetylcholine esterase inhibitors by H_2O_2-sensitive CdSe/ZnS quantum dots. *Angew. Chem.*, 120:1700–1703, 2008.

[113] Alfredo M. Morales and Charles M. Lieber. A laser ablation method for the synthesis of crystalline semiconductor nanowires. *Science*, 279:208–211, 1998.

[114] L. Manna and S. Kudera. *Wet-Chemical Approaches to Inorganic Nanostructures*, chapter Mechanisms underlying the growth of inorganic nanoparticles in the liquid phase. Transworld Research Network, Kerala, India, 2008.

[115] A. I. Ekimov and A. A. Onuschenko. *Sov. Phys. Semicond.*, 16:775–778, 1982.

[116] A. L. Efros. *Sov. Phys. Semicond.*, 16:772–775, 1982.

[117] Katerina Soulantica, Andre Maisonnat, Marie-Claire Fromen, Marie-Jose Casanove, Pierre Lecnte, and Bruno Chaudret. Synthesis and self-assembly of monodisperse indium nanoparticles prepared from the organometallic precursor [In(h5-c_5h_5)]. *Angew. Chem. Int. Ed.*, 40:448–451, 2001.

[118] Shengchun Qu, Haibin Yang, Dawei Ren, Shihai Kan, Guangtian Zou, Dongmei Li, and Minghui Li. Magnetite nanoparticles prepared by precipitation from partially reduced ferric chloride aqueous solutions. *Journal of Colloidal and Interface Science*, 215:190–192, 1999.

[119] P. D. Cozzoli, L. Manna, M. L. Curri, S. Kudera, C. Giannini, M. Striccoli, and A. Agostiano. Shape and phase control of colloidal ZnSe nanocrystals. *Chem. Mater.*, 17:1296–1306, 2005.

[120] A. A. Guzelian, J. E. B. Katari, Andreas V. Kadavanich, U. Banin, K. Hamad, E. Juban, A. P. Alivisatos, R. H. Wolters, C. C. Arnold, and J. R. Heath. Synthesis of size-selected, surface-passivated InP nanocrystals. *J. Phys. Chem.*, 100:7212–7219, 1996.

[121] M. A. Olshavsky, A. N. Goldstein, and Paul A. Alivisatos. Organometallic synthesis of GaAs crystallites exhibiting quantum confinement. *Journal of the American Chemical Society*, 112:9438–9439, 1990.

[122] I. Moreels, J. C. Martins, and Z. Hens. Ligand adsorption/desorption on sterically stabilized InP ciolloidal nanocrystals: Observation and thermodynamic analysis. *ChemPhysChem*, 7:1028–1031, 2006.

[123] Z. Hens, I. Moreels, and J. C. Martins. In situ 1H NMR study on the trioctylphosphine oxide capping of colloidal ino nanocrystals. *ChemPhysChem*, 6:2578–2584, 2005.

[124] A. Puzder, A. J. Williamson, F. Gygi, and G. Galli. Self-healing of CdSe nanocrystals: First-principles calculations. *Phys. Rev. Lett.*, 92:217401, 2004.

[125] A. Puzder, A. J. Williamson, N. Zaitseva, G. Galli, L. Manna, and A. P. Alivisatos. The effect of organic ligand binding on the growth of CdSe

nanoparticles probed by ab initio calculations. *Nano Lett.*, 4:2361–2365, 2004.

[126] Y. Chen, J. Vela, H. Htoon, J. L. Casson, D. J. Werder, D. A. Bussian, V. I. Klimov, and J. A. Hollingsworth. "giant" multishell CdSe nanocrystal quantum dots with suppressed blinking. *J. Am. Chem. Soc.*, 130:5026–5027, 2008.

[127] A. L. Efros. Almost alwys bright. *Nature Mater.*, 7:612–613, 2008.

[128] C. B. Murray, D. J. Norris, and M. G. Bawendi. Synthesis and characterization of nearly monodisperse CdE (E = sulfur, selenium, tellurium) semiconductor nanocrystallites. *J. Am. Chem. Soc.*, 115:8706–8715, 1993.

[129] X. G. Peng, J. Wickham, and A. P. Alivisatos. Kinetics of II-VI and III-V colloidal semiconductor nanocrystal growth: "focusing" of size distributions. *J. Am. Chem. Soc.*, 120:5343–5344, 1998.

[130] P. D. Cozzoli, Theresa Pellegrino, and L. Manna. Synthesis, properties and perspectives of hybrid nanocrystal structures. *Chem. Soc. Rev.*, 35:1195–1208, 2006.

[131] M. A. Hines and P. Guyotsionnest. Synthesis and characterization of strongly luminescing ZnS-capped CdSe nanocrystals. *J. Phys. Chem.*, 100:468–471, 1996.

[132] B. Rodriguez-Gonzalez, A. Burrows, M. Watanabe, C. J. Kiely, and L. M. L. Marzan. Multishell bimetallic Auag nanoparticles: synthesis, structure and optical properties. *J. Mater. Chem.*, 15:1755–1759, 2005.

[133] A. Sashchiuk, L. Langof, R. Chaim, and E. Lifshitz. Synthesis and characterization of PbSe and PbSe/PbS core-shell colloidal nanocrystal. *J. Cryst. Growth*, 240:431–438, 2002.

[134] Jiande Gu, Yaoming Xie, and Henry F. Schaefer III. Structural and energetic characterization of a DNA nucleoside pair and its anion: Deoxyriboadenosine (da) - deoxyribothymidine (dt). *J. Phys. Chem. B*, 109:13067–13075, 2005.

[135] H. W. Gu, R. K. Zheng, X. X. Zhang, and B. Xu. Facile one-pot synthesis of bifunctional heterodimers of nanoparticles: A conjugate of quantum dot and magnetic nanoparticles. *J. Am. Chem. Soc.*, 126:5664–5665, 2004.

[136] Taleb Mokari, Eli Rothenberg, Inna Popov, Ronny Costi, and Uri Banin. Selective growth of metal tips onto semiconductor quantum rods and tetrapods. *Science*, 304:1787–1790, 2004.

[137] Taleb Mokari, Claudia G. Szturum, Asaf Salant, Eran Rabani, and Uri Banin. Formation of asymmetric one-sided metal-tipped semiconductor nanocrystal dots and rods. *Nat Mater*, 4:855–863, 2005.

[138] S. Kudera, L. Carbone, M. F. Casula, R. Cingolani, A. Falqui, E. Snoeck, W. J. Parak, and L. Manna. Selective growth of PbSe on one or both tips of colloidal semiconductir nanorods. *Nano Lett.*, 5:445–449, 2005.

[139] D. J. Milliron, S. M. Hughes, Y. Cui, L. Manna, J. B. Li, L. W. Wang, and A.P. Alivisatos. Colloidal nanocrystal heterostructures with linear and branched topology. *Nature*, 430:190–195, 2004.

[140] K. W. Kwon and M. Shim. gamma-Fe_2O_3/II-VI sulfide nanocrystal heterojunctions. *J. Am. Chem. Soc.*, 127:10269–10275, 2005.

[141] X. Y. Gao, L. T. Yu, R. I. MacCuspie, and H. Matsui. Controlled growth of se nanoparticles on Ag nanoparticles in different ratios. *Adv Mater*, 17(4):426–429, 2005.

[142] R. S. Wagner and W. C. Ellis. Vapor-liquid-solid mechanism of single crystal growth. *Applied Physics Letters*, 4:89–90, 1964.

[143] L. Castaldi, K. Gainnakopoulos, A. Travlos, D. Niarchos, S. Boukari, and E. Beaurepaire. FePt and CoPt nanoparticles co-deposited on silicon dioxide - a comparative study. *Nanotechnology*, 19:085701 (5pp), 2008.

[144] MArco Lattuada and T. Alan Hatton. Functionalization of monodisperse magnetic nanoparticles. *Langmuir*, 23:2158–2168, 2007.

[145] Daniela Caruntu, Brian L. Cushing, Gabriel Caruntun, and Charles J. O'Connor. Attachment of gold nanograins onto colloidal magnetite nanocrystals. *Chem Mater*, 17:3398–3402, 2005.

[146] Yong Zhang, Nathan Kohler, and Miqin Zhang. Surface modification of superparamagnetic magnetite nanoparticles and their intracellular uptake. *Biomaterials*, 23:1553–1561, 2002.

[147] Claudia Altavilla, Enrico Ciliberto, Dante Gatteschi, and Claudio Sangregorio. A new route to fabricate monolayers of magnetic nanoparticles on silicon. *Adv Mater*, 17:1084–1087, 2005.

[148] G. Kataby, T. Prozorov, Yu. Koltypin, H. Cohen, Chaim N. Sukenik, A. Ulman, and Aharon Gedanken. Self-assembled monolayer coatings on amorphous iron and iron oxide nanoparticles: Thermal stability and chemical reactivity studies. *Langmuir*, 13:6151–6158, 1997.

[149] E. R. Childers, W. Imaino, J. H. Eaton, G. A. Jaquette, P. V. Koeppe, and D. J. Hellman. Six orders of magnitude in linear tape technology: The one terabyte project. *IBM J. Res. & Dev.*, 47(4):471–482, 2003.

[150] Fabienne Wetz, Katerina Soulantica, Marc Respaud, Andrea Falqui, and Bruno Chaudret. Synthesis and magnetic properties of Conanorod superlattices. *Materials Science and Engineering C*, 27:1162–1166, 2007.

[151] Theresa Pellegrino, Angela Fiore, Elvio Carlino, Cinzia Giannini, P. Davide Cozzoli, Giuseppe Ciccarella, Marc Respaud, Luca Palmirotta, Roberto Cingolani, and Liberato Manna. Heterodimers based on $CoPt_3$-Au nanocrystals with tunable domain size. *J. Am. Chem. Soc.*, 128:6690–6698, 2006.

[152] F. Dumestre, B. Chaudret, C. Amiens, Marie-Claire Fromen, Marie-Jose Casanove, P. Renaud, and P. Zurcher. Shape control of thermodynamically stable cobalt nanorods through organometallic chemistry. *Angew. Chem. Int. Ed.*, 41(22):4286–4289, 2002.

[153] F. Dumestre, B. Chaudret, C. Amiens, M. F. P. Respuad, P. Renaud, and P. Zurcher. Unprecedented crystalline super-lattices of monodisperse cobalt rods. *Angew. Chem. Int. Ed.*, 42:5213–5216, 2003.

[154] R. A. Andersen, K. Faegri, J. C. Green, A. Haaland, M. F. Lappert, W. P. Leung, and K. Rypdal. Synthesis of bis[bis(trimethylsilyl)amido]iron(II). structure and bonding in M[N(SiMe,)$_2$]$_2$ (M = Mn, Fe, Co): Two-coordinate transition-metal amides. *Inorg. Chem.*, 27(10):1782–1786, 1988.

[155] Fabienne Wetz, Katerina Soulantica, Andrea Falqui, Marc Respaud, Etienne Snoeck, and Bruno Chaudret. Hybrid co-Au nanorods: Controlling Au nucleation and location. *Angew. Chem. Int. Ed.*, 46:7079–7081, 2007.

[156] A. M. Schwartzberg, T. Y. Olson, C. E. Talley, and J. Z. Zhang. Synthesis, characterization, and tunable optical properties of hollow gold nanospheres. *J. Phys. Chem. B*, 40:19935–19944, 2006.

[157] E.V. Shevchenko, D.V. Talapin, A.L. Rogach, A. Kornowski, M. Haase, and H. Weller. Colloidal synthesis and self-assembly of $CoPt_3$ nanocrystals. *Journal of the American Chemical Society*, 124(38):11480–11485, 2002.

[158] E.V. Shevchenko, D.V. Talapin, H. Schnablegger, A. Kornowski, O. Festin, P. Svedlindh, M. Haase, and H. Weller. Study of nucleation and growth in the organometallic synthesis of magnetic alloy nanocrystals: The role of nucleation rate in size control of $CoPt_3$ nanocrystals. *Journal of the American Chemical Society*, 125(30):9090–9101, 2003.

[159] Y. Lu, H. Xiong, X. C. Jiang, Y. N. Xia, M. Prentiss, and G. M. Whitesides. Asymmetric dimers can be formed by dewetting half-shells of gold deposited on the surfaces of spherical oxide colloid. *J. Am. Chem. Soc.*, 125:12724–12725, 2003.

[160] I. L. Medintz, K. E. Sapsford, J. H. Konnert, A. Chatterji, T. Lin, J. E. Johnsson, and H. Mattoussi. Decoration of discretely immobilized cowpea mosaic virus with luminescent quantum dots. *Langmuir*, 21:5501–5510, 2005.

[161] Yoo Seong Choi, Seung Pil Pack, and Young Je Yoo. Development of a protein microarray using sequence-specific DNA binding domain on DNA chip surface. *Biochem Biophys Res Comm*, 329:1315–1319, 2005.

[162] Nadrian C. Seeman. DNA nickes and nodes and nanotechnology. *Nano Lett.*, 1:22–26, 2001.

[163] Erez Braun, Yoav Eichen, and Uri Sivan. DNA-templated assembly and electrode attachment of a conducting silver wire. *Nature*, 391:775–778, 1998.

[164] Yoav Eichen, Erez Braun, Uri Sivan, and G. Ben-Yoseph. Self-assembly of nanoelectronic components and circuits using biological tmplates. *Acta Polym.*, 49:663–670, 1998.

[165] James Watson and Francis Crick. A structure for deoxyribose nucleic acid. *Nature*, 171:737, 1956.

[166] M. Mandelkern, J. Elias, D. Eden, and Crothers D. The dimensions of DNA in solution. *J. Mol. Biol.*, 152:153–161, 1981.

[167] S. P. Goff and P. Berg. Construction of hybrid viruses containing sv40 and lambda phage DNA segments and their propagation in cultured monkey cells. *Cell*, 9:695–705, 1976.

[168] L. Houdebine. Transgenetic animal models in biomedical research. *Methods Mol. Biol.*, 360:163–202.

[169] A. B. Steel, R. L. Levicky, T. M. Herne, and M. J. Tarlov. Immobilization of nucleic acids at solid surfaces: Effect of oligonucleotide length on layer assembly. *Biophysical Journal*, 79:975–981, 2000.

[170] Alexander W. Peterson, Lauren K. Wolf, and Rosina M. Georgiadis. Hybridization of mismatched or partially matched DNA at surfaces. *Journal of the American Chemical Society*, 124:14601–14607, 2002.

[171] Selina Moses, Scott H. Brewer, Lisa B. Lowe, Simon E. Lappi, Lauren B.G. Gilvey, Marc Sauthier, Robert C. Tenent, Daniel L. Feldheim, and Stefan Franzen. Characterization of single- and double-stranded DNA on gold surfaces. *Langmuir*, 20:11134–11140, 2004.

[172] Helen G. Hansma, Robert L. Sisnheimer, Min-Qian Li, and Paul K. Hansma. Atomic force microscopy of single- and double-stranded DNA-blockcopolymer-nanopartikeln. *Nucleic Acids Research*, 20:3585–3590, 1992.

[173] Justin D. Cohen, John P. Sadowski, and Peter B. Dervan. Addressing single molecules on DNA nanostructures. *Angewandte Chemie*, 119:8102–8105, 2007.

[174] Theresa Pellegrino, R. A. Sperling, A. P. Alivisatos, and W. J. Parak. Gel electrophoresis of gold-DNA nanoconjugates. *Journal of Biomedicine and Biotechnology*, 2007:26796 (9 pp), 2007.

[175] J. Sun, C. DuFort, M. C. Daniel, A. Murali, C. Chen, K. Gopinath, B. Stein, M. De, and V. M. Rotello. Core-controlled polymorphism in virus-like particles. *Proc. Natl. Acad. Sci. USA*, 104:1354–1359, 2007.

[176] Q. Wang, T. Lin, L. Tang, J. E. Johnson, and M. G. Finn. Icosahedral virus particles as addressable nanoscale building blocks. *Angew. Chem. Int. Ed.*, 41:459–462, 2002.

[177] F. Garcia-Arenal. Sequence and structure at the genome 3′ end of the u2-strain of tobacco mosaic virus, a histidine-accepting tobamovirus. *Virology*, 167:201–206, 1988.

[178] R. N. Perham and T. M. A. Wilson. The polarity of stripping of coat protein subunits from the RNA in tobacco mosaic virus under alkaline conditions. *FEBS Lett.*, 62:111–28, 1976.

[179] T. M. A. Wilson, G. P. Lomonossoff, and J. F. Glover. Dimthyl sulphoxide (DMSO) disassembles tobacco mosaic virus predominantly from the 5′ end of the viral RNA. *J. Gen. Virol.*, 53:225–234, 1981.

[180] T. Lin, Z. Chen, R. Usha, C. V. Stauffacher, J.-B. Dai, T. Schmidt, and J. E. Johnson. The refined crystal structure of cowpea mosaic virus at 2.8a resolution. *Virology*, 265:20–34, 1999.

[181] G. P. Lomonossoff and J. E. Johnson. The synthesis and structure of comovirus capsids. *Prog. Biophys. molec. Biol.*, 55:107–137, 1991.

[182] Nicole F. Steinmetz, George P. Lomonossoff, and David J. Evans. Decoration of cowpea mosaic virus with multiple, redox-active, organometallic complexes. *Small*, 2:530–533, 2006.

[183] Nicole F. Steinmetz, Eva Bock, Ralf P. Richter, J. P. Spatz, George P. Lomonossoff, and David J. Evans. Assembly of multilayer arrays of viral nanoparticles via biospecifc recognition: A quartz crystal microbalance with dissipation monitoring study. *Biomacromolecules*, 9:456–462, 2008.

[184] C. L. Cheung, S.-W. Chung, A. Chatterji, T. Lin, J. E. Johnson, S. Hok, J. Perkins, and J. J. De Yoreo. Physical controls on directed virus assembly at nanoscale chemical templates. *J. Am. Chem. Soc.*, 128:10601–10607, 2006.

[185] John Henry J. Scott. Accuracy issues in chemical and dimensional metrology in the SEM and TEM. *Meas. Sci. Technol.*, 18:2755–2761, 2007.

[186] G. Binnig, C. F. Quate, and Ch. Gerber. Atomic force microscope. *Phys. Rev. Lett.*, 56(9):930–934, March 1986.

[187] J. F. Moulder, Stickle, Sobol W. E., and K. D. A. P. E., Bomben. *Handbook of X-ray Photoelectron Spectroscopy*. Perkin-Elmer Corporation, Eden Prairie, Minnesota, USA.

[188] Günter Sauerbrey. Verwendung von Schwingquarzen zur Wägung dünner Schichten und zur Mikrowägung. *Zeitschrift für Physik Journal*, 155:206–222, 1959.

[189] Frederik Hoeoek, Charlotte Larsson, and Camilla Fant. *Encyclopedia of Surface- and Colloid Science*, chapter Biofunctional Surfaces Studied by Quartz Crystal Microbalance with Dissipation Monitoring. Marcel Dekker, New York, 2002.

[190] T. H. Courtney. *Mechanical Behavior of Materials*. Waveland Press Inc., Illinois, USA, 2005.

[191] Claire J. Carmalt, Neville A. Compton, R. John Errington, George A. Fisher, Ismunaryo Moendar, Nicholas C. Norman, and Kenton H. Whitmire. Homoleptic bismuth amides. *Inorganic Synthesis*, 31:98–101, 1997.

[192] Joachim P. Spatz, Stefan Moessmer, Christoph Hartmann, Martin Moeller, Thomas Herzog, Michael Krieger, Hans-Gerd Boyen, Paul Ziemann, and Bernd Kabius. Ordered deposition of inorganic clusters from micellar block copolymer films. *Langmuir*, 16, 2000.

[193] C. Soennichsen. *Plasmons in metal nanostructures*. PhD thesis, Ludwig-Maximilians Universität, München, 2001.

[194] Anton A. Darhuber, Sandra M. Troian, Jeffrey M. Davis, Scott M. Miller, and Sigurd Wagner. Selective dip-coating of chemically micropatterned surfaces. *Journal of Applied Physics*, 88(9):5119–5126, 2000.

[195] *Lange's Handbook of Chemistry*. MacGraw Hill Handbooks, 2004.

[196] M. J. Levene, Jonas Korlach, Stephen W. Turner, Mathieu Foquet, H. G. Craighead, and W. W. Webb. Zero-mode waveguides for single-molecule analysis at high concentrations. *Science*, 299:682–686, 2003.

[197] Alena M. Lieto and Nancy L. Thompson. Total internal reflection with fluorescence correlation spectroscopy: Nonfluorescent competitors. *Biophys J*, 87:1268–1278, 2004.

[198] Kai Hassler, Tiemo Anhut, Rudolf Riegler, Michael Goesch, and Theo Lasser. High count rates with total internal reflection fluorescence correlation spectroscopy. *Biophys J: Biophys Let*, pages L01–L03, 2005.

[199] Mathieu Foquet, Kevan T. Samiee, X. Kong, B. P. Chauduri, Paul M. Lundquist, Stephen W. Turner, Jake Freudenthal, and Daniel B. Roitman. Improved fabrication of zero-mode waveguides for single-molecule fabrication. *J Appl. Phys.*, 103:034301 (9pp), 2008.

[200] Nan Ma, Jun Yang, Kelly M. Stewart, and Shana O. Kelley. DNA-passivated CdS nanocrystals: Luminescence, bioimaging, and toxicity profiles. *Langmuir*, 23:12783–12787, 2007.

[201] A. Salant, E. Amitay-Sadovsky, and U. Banin. Directed self-assembly of gold-tipped CdSe nanorods. *J. Am. Chem. Soc.*, 128:10006–10007, 2006.

[202] J. Christopher Love, Lara A. Estroff, Jennah K. Kriebel, Ralph G. Nuzzo, and George M. Whitesides. Self-assembled monolayers of thiolates on metals as a form of nanotechnology. *Chem Rev*, 105:1103–1169, 2005.

[203] Swapnil Kohale, Sara M. Molina, Brandon L. Weeks, Rajesh Khare, and Louisa J. Hope-Weeks. Monitoring the formation of self-assembled monolayers of alkanedithiols using a micromechanical cantilever sensor. *Langmuir*, 23:1258–1263, 2007.

[204] Jacques Bluemmel, Nadine Perschmann, Daniel Aydin, Jovana Drinjakovic, Thomas Surrey, Monica Lopez-Garcia, Horst Kessler, and Joachim P. Spatz. Protein repellent properties of covalently attached PEG coatings on nanostructured sio2-based interfaces. *Biomaterials*, 28(32):4739–4747, November 2007.

[205] N. Herron, J. C. Calabrese, W. E. Farneth, and Y. Wang. Crystal structure and optical properties of Cd(32)S(14)(SC(6)H(5))(36)-DMF(4), a cluster with a 15 angstrom CdS core. *Science*, 259:1426–1428, 1993.

[206] Theresa Pellegrino, L. Manna, S. Kudera, T. Liedl, D. Koktysh, A.L. Rogach, S. Keller, J. Raedler, G. Natile, and W. J. Parak. Hydrophilic nanocrystals coated withe an amphiphilic polymer shell: A general route to water soluble nanocrystals. *Nano Lett.*, 4:703–707, 2004.

[207] T. Zhang, J. Ge, Y. Hu, and Y. Yin. A general approach for transfering hydrophobic nanocrystals into water-soluble. *Nano Lett.*, 2007.

[208] F. Hoeoek, A. Ray, B. Norden, and B. Kasemo. Characterization of PNA and DNA immobilization and subsequent hybridization with DNA using acoustic-shear-wave attenuation measurements. *Langmuir*, 17(26):8305–8312, 2001.

[209] Marian E. Gindy, Anthanassios Z. Panagiotopoulos, and Robert K. Prud'homme. Composite block copolymer stabilzed nanoparticles: Simultaneous encapsulation of organic actives and inorganic nanostructures. *Langmuir*, 24:83–90, 2008.

[210] Y. Lin, A. Boeker, J. He, K. Sill, G. Hiang, C. Abetz, X. Li, J. Wang, T. Emrick, S. Long, Q. Wang, A. Balazs, and T. P. Russell. Self-directed self-assembly of nanoparticle/copolymer mixtures. *Nature*, 434:55–59, 2005.

[211] Shan Zou, Rui Hong, Todd Emrick, and Gilbert C. Walker. Ordered CdSe nanoparticles within self-assembled block copolymer domains on surfaces. *Langmuir*, 23:1612–1614, 2007.

[212] S. Joon Kwon and Jae-Gwan Park. Theoretical analysis of the radius of semiconductor nanowires grown by the catalytic vapour-liquid-solid mechnism. *Journal of Physics: Condensed Matter*, 18:3875–3885, 2006.

[213] Lian Ouyang, Kristin n. Maher, Chun Liang Yu, Jusitn McCarthy, and Hongkun Park. Catalyst-assisted solution-liquid-solid synthesis of CdS/CdSe nanorod heterostructures. *Journal of tha American Chemical Society*, 129:133–138, 2007.

[214] Ralf P. Richter, K. K. Hock, J. Burkhartsmeyer, H. Boehm, P. Bingen, G. Wang, Nicole F. Steinmetz, David J. Evans, and J. P. Spatz. Membrane-grafted hyaluronan films: A well-defined model system of glycoconjugate coats. *J. Am. Chem. Soc.*, 129:5306–5307, 2007.

[215] George L. Ellman. Tissue sulfhydryl groups. *Archieves of Biochemistry and Biophysics*, 82:70–77, 1959.

[216] Concetta Nobile, V. A. Fonoberov, S. Kudera, A. Della Torre, A. Ruffino, G. Chilla, Tobias Kipp, D. Heitmann, L. Manna, R. Cingolani, A. A. Balandin, and Roman Krahne. Confined optical phonon modes in aligned nanorod arrays detected by resonsnt inelastic light scattering. *Nano Lett.*, 2007.

[217] M. Law, L. E. Greene, J. C. Johnson, R. Saykally, and P. Yang. Nanowire dye-sensitized solar cells. *Nat Mater*, 4:455–459, 2005.

List of Figures

List of Tables

Publications

N. F. Steinmetz, E. Bock, R. P. Richter, J. P. Spatz, G. P. Lomonossoff, D. J. Evans: *Assembly of Multilayer Arrays of Viral Nanoparticles via Biospecific Recognition: A Quartz Crystal Microbalance with Dissipation Monitoring Study*, Biomacromolecules **2008**, *9*, 456-462.

T. Lohmüller, E. Bock, J. P. Spatz: *Synthesis of Quasi Hexagonal Ordered Arrays of Metallic Nanoparticle Arrays with Tuneable Particle Size*, Advanced Materials **2008**, *20*, 2297-2302.

Acknowledgements

Several people were involved in the development of this work. I am especially grateful to my supervisor Prof. Joachim Spatz, for offering me the possibility to work on this highly interesting and challenging topic. He gave me the opportunity for a stay in Lecce. I would like to express my gratitude for his academic support, trust and all the academic opportunities he gave me.

I also want to express my gratitude to Liberato Manna and Teresa Pellegrino for being supervisors and advisors during my stay in Lecce. The discussions were always motivating and fruitful. In Lecce, I found many dear colleagues, helping me at work and in every days life. In particular it was Angela Fiore, Alessandra Quarta, Stefan Kudera and Luigi Carbone, which introduced me to the world of inorganic nanocrystals. A big thanks also to Valentina Arima for spending many hours at the AFM with me.

I want to thank Katerina Soulantica and Bruno Chaudret for giving me the chance to work with together with them, also in their lab in Toulouse.

To Asaf Salant and Uri Banin I want to express my gratitude for providing me with inorganic nanocrystals. During the SA-NANO meetings Uri seemed to be an inexhaustible source of ideas.

Many thanks also to Nicole Steinmetz. She introduced me to the world of the virus nanoparticles and was always helpful in answering all my questions concerning biology. Especially in working with ssDNA she was a great help, also by supporting me with material.

I want to express my gratitude to Gunter Richter, for all the XPS measurements he performed for me. He always found the time to explain and to discuss with me the data.

I want to thank Ralf Richter for introducing me to the QCM-D technique. He always found the time to help me in interpreting the data.

It would have been impossible to me to handle all the bureaucracy, especially during my stay in Italy, without the help of Elke Schönig-Erdinger and Elisabeth Pfeilmeier.

During my stay in Italy, I found several friends, helping me to survive in Italy even without speaking Italian. Thanks to Roman and Stefan, for the everyday lunch meetings at the Scacca; to the container-crew (Concetta Nobile, Luigi Carbone, Angela Fiore, Isabella Francini, Allesandra Quarta, Gianvito Caputo, Stefan Kudera, Marianna Casavola, Benedetta Antonazzo) for always good atmosphere at work but also around; to Davide and Libero for joining me by running around the sports ground in the evening; to Kirsten, Philo and Manuel for countless espressi, polpette, and all the time at the various beaches.

Many thanks to Heike Böhm, Lisa Maus, Theo Lohmüller, and Stefan Kudera for endless discussions about my work. They were always an input for new ideas and getting a new point of view on the experiments. Thanks to Lisa and Stefan additionally for having lots of fun in the lab.

A big thanks goes to Margit Kapp, Maria Sycha, Christine Mollenhauer, Henriette Ries and Ioanis Gregoridis for providing breakfast, taking care for the coffee machine and help in the lab.

Many thanks to my office mades, Nadine and Leticia, and the neighbor-office mades, Julia Schölermann and Stefanie Korte, as well as Heike Böhm and Lisa Maus for spending several hours with drinking tea and eating cake and walking around the lake.

Thanks to the people in Heidelberg (Marcus Abel, Julia Ranzinger, Kai Uhrig, Theobald Lohmüller and all the others) for finding always time for a coffee or a beer.

Thanks to Tobias Wolfram, for always having some chocolate in his cupboard. I want to thank all the people from the Spatz group, in Heidelberg as well as in Stuttgart, for having a good time during my PhD.

Many thanks to Tobias Wolfram, Lisa Maus, Stefan Kudera, and Theo Lohmüller for proofreading of this work.

I finally want to thank my family, for destracting me from work from time to time.

Ich erkläre hiermit, dass ich die vorgelegte Dissertation selbst verfasst und mich keiner anderen als der von mir bezeichneten Quellen und Hilfen bedient habe.

Heidelberg, den 21. August 2008 .....

Eva Bock